



Spatio–Angular Microscopy

PhD Thesis

Martin Kielhorn

April 2013

Abstract

Photobleaching and phototoxicity pose a problem in live cell imaging. Fluorescence imaging induces reactive oxygen species in observed organisms which can alter the behaviour of the sample. Hence, minimising the light exposure is an important goal.

We augment a wide field epifluorescence microscope with two spatial light modulators. By controlling the spatial excitation pattern and the angle of illumination, we can adapt the illumination to the specimen. In many cases, this technique will create exposures with reduced excitation of the out-of-focus fluorophores, resulting in better image quality and less phototoxicity.

Our custom software is used to obtain an initial image stack of the specimen. Subsequent image sections are exposed with excitation patterns that account for the previous image stack. Depending upon the distribution of fluorophores, this adaptive exposure can considerably reduce photobleaching and phototoxicity.

Preface

The work described in this thesis was carried out between June 2008 and April 2013.

In chapter 1, we introduce photophysics of fluorescence and emphasize the importance of oxygen for phototoxicity. Furthermore, we also explain conventional microscopes and CCD cameras.

In chapter 3, we compare some state-of-the-art techniques for illumination control in microscopes. Particularly in section 3.3.2, we discuss the micro-lens based light field microscope by Levoy's computational photography group, which imaged the toy soldier in 2003.

In chapter ??, we describe our microscope and in chapter ??, we show some images, taken with illumination control in our prototype.

- ccd measurement
- mapping lcos camera

In the appendix, we also describe a completely different approach for spatio-angular illumination based on holography (Appendix ??) and we document an interferometric attempt to convert our precise programmable phase mask into a spatial intensity modulator (Appendix ??).

Note that the Appendix ?? describes a modification of our prototype with a spatial light modulator that receives data from a graphics card. A higher bandwidth makes this approach more useful than the prototype described in the main text and we tried to implement this first. However eventually, it proved too difficult to trigger the components in this configuration and we switched to the more predictable USB-controlled display as described in the main body of the text.

The appendix also contains some theoretical explanations of raytracing (Appendix 6), computational optical sectioning (Appendix ??) and the wave-optics based simulation of our microscope (Appendix ??).

Source Code Availability

Source code that has been developed during this project is available on <https://github.com/plops/mma>. It contains implementations for:

- illumination planning based on raytraces (see Appendix 6)
- moving the z–stage of a Zeiss Axiovert 200M microscope body
- controlling an Andor Clara camera using the Andor SDK version 2. For the other cameras following below, control software was written:
 - Photometrics Cascade II (interface to unsupported closed-source driver, only works on very old 32-bit Linux kernels)
 - mvBlueFox 102G using the SDK
 - Logitech Pro 9000 using a generic Video4Linux interface
 - Andor sCMOS using Andor SDK version 3
- displaying patterns using a graphics card that supports OpenGL on a ForthDD SXGA ferroelectric LCoS display
- controlling a stand-alone ForthDD WXGA 3DM display controller using USB
- estimating the parameters of a rigid transformation between camera and LCoS display (see Appendix ??),
- controlling the micro-mirror array by Fraunhofer IPMS using their SDK
- some specific image processing tools:
 - three-dimensional convolution and Fourier transforms
 - drawing of lines and ellipsoids in volumes
 - rasterization of triangles (for creating shadow maps in the BFP, see section ??)
 - calculation of optical transfer function for high NA objectives
 - localization of spherical nuclei in volumetric data (parts of the algorithm as described in Santella et al. (2010))

The main development was done using GNU Linux. However, portability was kept in mind and most of the code was made to work with Microsoft Windows as well.

FIXME TRANSLATE:

Die Zeichnung auf der Titelseite zeigt den Strahlenverlauf durch ein 100× objective mit numerical aperture 1.45. Leider sind Designparameter der von mir verwendeten Objektive kaum beizukommen deshalb habe ich hier Daten aus einem Patent verwendet (Matthae et al. 2003).

Acknowledgements

It is my pleasure to thank all those who have made this thesis possible. First and foremost, I owe my deepest gratitude to my supervisor Rainer Heintzmann for giving me the opportunity to become part of his research group at King's College London and later in the Institute of Photonic Technology in Jena.

I owe my sincere thanks to Kai Wicker, Jakub Nedbal, Susan Cox, Daniel Appelt, Ondřej Mandula, Ronny Förster, Ivana Šumanovac, Eckhard Birkner, Kathrin Klehs and all the other members of our group for valuable discussions, support and review of the manuscript.

My sincere thanks to the European Union Framework Programme 7 (project number 2115597) for the studentship on this project. I also thank Erhard Ipp, Günter Zöchling, Vincent Galy, QueeLim Ch'ng, Jörg Heber, Mark Eckert, Dirk Berndt, Joel Seligson, Jean-Yves Tinevez and Florian Rückert for helpful collaboration.

Furthermore I highly appreciate the input of Herbert Gross, Miroslav Grajcar, Edward Rosten, Christophe Rhodes, Paul Khuong, Nikodemus Siivola, Gabor Melis and Luís Oliveira. Occasionally, the expertise and insight of them steered me into right direction or greatly simplified problems I faced.

Finally, I wish to thank the authors and contributors to the following software projects: Linux, GCC, Emacs, SBCL (Rhodes 2008), Maxima, Micromanager (Edelstein et al. 2010), DIPimage, Wireshark, Latex, Inkscape, Gimp, ImageJ/Fiji (Abràmoff et al. 2004; Schindelin et al. 2012) and Blender. These free software projects and their communities are invaluable to my work and greatly enhance my efficiency.

The work presented in this thesis is my own, unless I cite a reference.

M. K.

Jena, Germany

April 2013

Contents

1. Introduction	11
1.1. Phototoxicity in life sciences and the model organism <i>C. elegans</i> .	12
1.2. Photophysical principles of phototoxicity	16
1.3. Conventional microscopes	19
1.3.1. Ray-optical description of a large-aperture lens	19
1.3.2. Wave-optical theory for image formation in a fluorescence microscope	20
1.3.3. Illumination in a wide-field epifluorescence microscope	26
1.3.4. Phototoxicity in conventional microscopes	28
1.3.5. Conclusion	28
1.4. Image detectors in wide-field microscopy	28
1.4.1. Introduction	28
1.4.2. Photon shot noise and read noise	30
1.4.3. Comparison chart for detector selection	32
1.4.4. Calibration of the EM-CCD gain	36
1.4.5. Conclusion	37
2. Methods of controlling illumination patterns	38
2.0.6. 2-photon laser scanning fluorescence microscopy	38
2.1. programmable array	38
3. Other approaches of light control	39
3.1. Light sheet fluorescence microscopy	39
3.1.1. Light sheet generation with cylindrical lens	39
3.1.2. Light sheet generation using the detection objective	41
3.2. Scanning techniques for improving light utilization	42
3.2.1. Controlled light exposure microscopy (CLEM)	42
3.2.2. Acousto-optic deflectors for fast beam steering	43
3.3. Non-scanning techniques	43
3.3.1. Direct illumination	43

Contents

3.3.2. Intensity modulation	45
3.3.3. Temporal focusing	48
3.3.4. Phase modulation	49
4. The concept of spatio-angular microscopy	52
4.1. Motivation	52
4.2. An imaging protocol with spatio-angular illumination control	56
4.2.1. Description of an exemplary biological specimen	56
4.2.2. Preparation of living embryo samples	56
4.2.3. Sectioning through structured illumination	57
4.2.4. Computer model for the integration of a priori knowledge about the biological events	57
4.2.5. Illumination optimization by means of raytracing	59
5. Description of our prototype for spatio-angular illumination	61
5.1. Description of the optical components	61
5.1.1. Ensuring homogeneous illumination	63
5.1.2. Fourier optical filter for contrast generation on pupil plane SLM	65
5.1.3. Relay optics between pupil plane and focal plane SLM	68
5.1.4. Contrast generation on focal plane SLM using polarization	69
5.1.5. Variable telescope as tube lens	69
5.2. Electronic control of the component	70
5.3. Mapping between pixels of the focal plane SLM and camera pixels	71
5.3.1. The rigid coordinate transform	72
5.3.2. Experimental example and image processing	73
5.3.3. Conclusion	74
6. Raytracing for spatio-angular microscopy	76
6.1. Refraction at planar surface	76
6.2. Intersection of a ray and a plane	78
6.3. Intersection of a ray and a sphere	79
6.3.1. Solving the quadratic equation	80
6.4. Refraction on paraxial thin lens	80
6.5. Refraction through high NA objective (illumination)	81
6.6. Reverse path through oil objective (detection)	82
6.6.1. Easy case: back focal plane positions only	82
6.6.2. Full raytrace through oil objective in detection direction . .	83

Contents

6.6.3. Treatment of aberration (detection)	84
6.7. Sphere projection	85
6.8. Conclusion	87
7. Experimental results with spatio-angular microscope	89
7.1. Measuring acceptance angle for three different embedding media .	89
7.2. Measuring light distribution by bleaching a fluorescent gel . . .	91
7.3. Spatio-angular illumination of three-dimensionally distributed beads	93
7.4. Angular illumination and a higher concentration of beads	96
7.5. Conclusion	97
8. Discussion	98
8.1. Outlook	102
A. EM-CCD camera calibration	103
A.1. Andor Basic code listing for automatic image acquisition	103
A.2. Python code listing for the read noise evaluation	106
B. Optical sectioning by structured illumination	109
C. Mapping between focal plane SLM and camera	110
C.1. Rigid coordinate transformation	110
C.2. Image processing: Localizing bright spots on the camera	111

Nomenclature

- β Transversal magnification of an objective $\beta = f_{\text{TL}}/f$, for Zeiss lenses the magnification β is written on the objective and the focal length of the tube lens is defined as $f_{\text{TL}} = 164.5 \text{ mm}$, page 15
- \mathcal{E} Etendue, information capacity, light gathering capacity or space-bandwidth product; its value is related to the number of point spread functions that can be resolved in the field., page 23
- Ω Excitation dose in $\text{J}/(\text{cm}^2 \text{stack})$, page 11
- Φ_e Radiant flux of excitation light in watts, page 11
- $\mathbf{r} = (r_x, r_y, r_z)^T$ Three-dimensional spatial coordinate, page 18
- $\mathbf{r}_t = (r_x, r_y)^T$ Transversal two-dimensional spatial coordinate, page 18
- $\mathbf{v} = (v_x, v_y, v_z)^T$ Three-dimensional spatial frequency, page 18
- $\mathbf{v}_t = (v_x, v_y)^T$ Transversal two-dimensional spatial frequency, page 18
- $\tilde{u}(\mathbf{v})$ Fourier transform of scalar field as a function of spatial frequencies, page 18
- $u(\mathbf{r})$ Scalar field as a function of spatial coordinates, page 18
- AOD Acousto-optic deflector, page 39
- AOM Acousto-optic modulator, page 39
- chief ray Ray from the periphery of the field through the center of the entrance aperture, page 15
- CLEM Controlled light exposure microscopy, page 35
- DMD Digital micro mirror device, page 41
- DPSS Diode-pumped solid-state (laser), page 40

Contents

- EGFP Enhanced green fluorescent protein, page 40
- EM-CCD Electron multiplying charge-coupled devices, page 7
- entrance aperture Projection of the limiting aperture of the optical system into object space, page 15
- Ewald sphere Transfer function of free space, page 18
- GFP Green fluorescent protein, page 40
- HILo Highly inclined and laminated optical sheet microscopy, page 38
- I²M Image interference microscopy (Gustafsson et al. 1999), page 22
- IFTA Iterative Fourier transform algorithm, page 45
- LCoS Liquid crystal on silicon (display), page 40
- LED Light-emitting diode, page 40
- LED light emitting diode, page 58
- marginal ray Axial ray through the periphery of the entrance aperture, page 15
- MLE-PAM Minimized light exposure programmable array microscope, page 41
- MMA micro-mirror array, page 40
- OPM Oblique plane microscopy, page 37
- PAM Programmable array microscopy, page 41
- PCF Phase contrast filter, page 46
- SPIM Selective plane illumination microscopy, page 36
- TL tube lens, page 42
- USB Universal Serial Bus., page 91
- VCSEL Vertical-cavity surface-emitting laser, page 40
- YFP Yellow fluorescent protein, page 40

1. Introduction

my device

In this work I discuss a modification of a fluorescence microscope that minimizes the toxic effects of the excitation light.

phototoxicity

In the following introductory chapter I describe what phototoxicity is and how it comes about. Then I give an example of how it influences biological observations in a developing *C. elegans* embryo and describe how this particular biological system can be used to evaluate and compare the phototoxicity of different microscopes.

cameras

Later in this chapter I give an overview of image formation in the wide-field microscope and I describe its principle limitations regarding resolution and depth discrimination. Furthermore I discuss the two most important current image detector technologies — electron multiplying charge-coupled devices (EMCCD) and scientific complementary metal–oxide–semiconductor (sCMOS).

Regardless of whether it is the picture of earth captured by an orbiting satellite, the x-ray motion picture of a running dog or the time-lapse recording of a blooming flower. Images capture our imagination and they are a good starting point to develop new models and theories.

This is particularly true for microscopy. Only after people became aware of microorganisms by direct observation, medieval quack could finally be overcome and modern medicine based on the scientific method flourished instead.

Even today — with electron microscopes, magnetic resonance tomography and sequencing machines — optical microscopy still is an indispensable tool for research of living organisms.

Fluorescence microscopy is of particular importance: It enables the scientist to selectively label a particular type of molecule in living cells and observe how they perform their biological function.

Besides localizing molecules it is possible to measure physical quantities inside of the sample. There are, for example, fluorescent labels that report membrane potentials or viscosity inside of cells.

Finally, it is even possible to exert a controlling function with the excitation light: There are compounds that locally release chemicals when illuminated and

1. Introduction

there are genetically encoded ion channels that can be switched by light (Boyden et al. 2005).

However, the excitation light introduces unnatural and potentially deleterious energy into the specimen. If the exogenous light harms the observed organism in any way, this effect is called phototoxicity.

There are a number of techniques that can reduce phototoxicity: Two photon excitation, controlled light exposure, selective plane illumination, highly inclined and laminated optical sheet, and oblique plane microscopy. I introduce them in chapter 2. These techniques have different pros and cons and not all are equally suited for a specific problem, e.g. selective plane illumination is very effective, but it needs two perpendicular lenses and can not be used for multiwell plates or to observe the liver of a living, adult mouse.

In this work I present an approach that makes use of modern display and camera technology. We only modify the microscope's illumination path, the space around objective lens and specimen remains as accessible as in any conventional wide-field microscope.

1.1. Phototoxicity in life sciences and the model organism

C. elegans

The partner in our project who is responsible for decisions related to life sciences and biology is Institut Pasteur (Paris, FR). They work on infectious diseases.

In order to motivate the importance of phototoxicity, I would like to portray an elegant drug screening experiment which I have seen on one of my visits in Paris: An automatic microscope continuously images a cell culture in multiwell plates. These cells carry a pathogen. The pathogen, the nuclei of the cultured cells and the membranes of the cells are each stained with a different fluorophore. The cells in each well of the plates are exposed to a different chemical.

A chemical is considered a hit and will be investigated during further trials, when the time lapse images show that the culture cells stay healthy and the number of pathogens decrease. As neither people nor animals come to harm, this screening experiment is an impeccable method to systematically understand and hopefully heal certain diseases. However, this experiment does not work very well, if the excitation light — and not the drug — kills the pathogens. The effect of phototoxicity should therefore be minimized.

Now one would hardly develop a microscope and directly test it with dangerous

1. Introduction

pathogens. As part of our collaboration, the Institut Pasteur therefore developed a safe biological test system that is relatively easy to maintain (Stiernagle 2006) and allows to test the phototoxicity of various microscopes (Tinevez et al. 2012).

The basis of the system is the embryo of the organism *C. elegans*. These are small invertebrates. The adult form is approximately 1 mm long. Their anatomy and development are comparatively simple and have been well characterized (Sulston and Horvitz 1977; Durbin 1987).

We use embryos of a genetically modified strain¹ that expresses eGFP tagged histones (enhanced green fluorescent protein, excitation maximum 488 nm, emission maximum 509 nm). Histones are incorporated into the chromatin during cell divisions, i.e. the nuclei of our worms fluoresce green. The mother worm passes a sufficient amount of these proteins into the cytoplasm of the embryo. In the beginning of its development the embryo entirely relies on this reserve of histones. Only in a much later stage — certainly not during the first few hours, that we observe — it will form its own histones.

Figure 1.1 compares time-lapse experiments on three different *C. elegans* embryos with varying excitation intensities.

The lineage tree of two developing *C. elegans* embryos is the same. With all other factors being equal, particularly if the temperature is constant at $21 \pm 1^\circ\text{C}$, two different embryos will develop at the same speed from egg to fertile adult in three and a half days.

At the beginning of the experiment, embryos are removed from their mothers at an identical stage, before any cellular divisions have occurred. Then a z-stack of the egg with 41 slices and one micron z-sampling is obtained every two minutes.

The columns in Figure 1.1 depict three different embryos whose development was imaged according to this protocol for two hours and 38 minutes with different excitation powers.

The figure displays the maximum intensity projections of the z-stacks. In order to make the cell nuclei visible in all images, I normalized the data to the same range. As can be guessed from the photon shot noise, the upper left image contains the least number of fluorescence photons, and the upper right the most.

An analysis of the time-lapse data show that one hour into the experiment the embryo with the highest excitation dose (right) has stopped developing and its fluorophores are strongly bleached. Some cells even turned apoptotic and went into programmed cell death.

After two hours and 38 minutes the experiment was stopped and the embryo

¹Our strain has WormBase ID AZ212 (Praitis et al. 2001).

1. Introduction

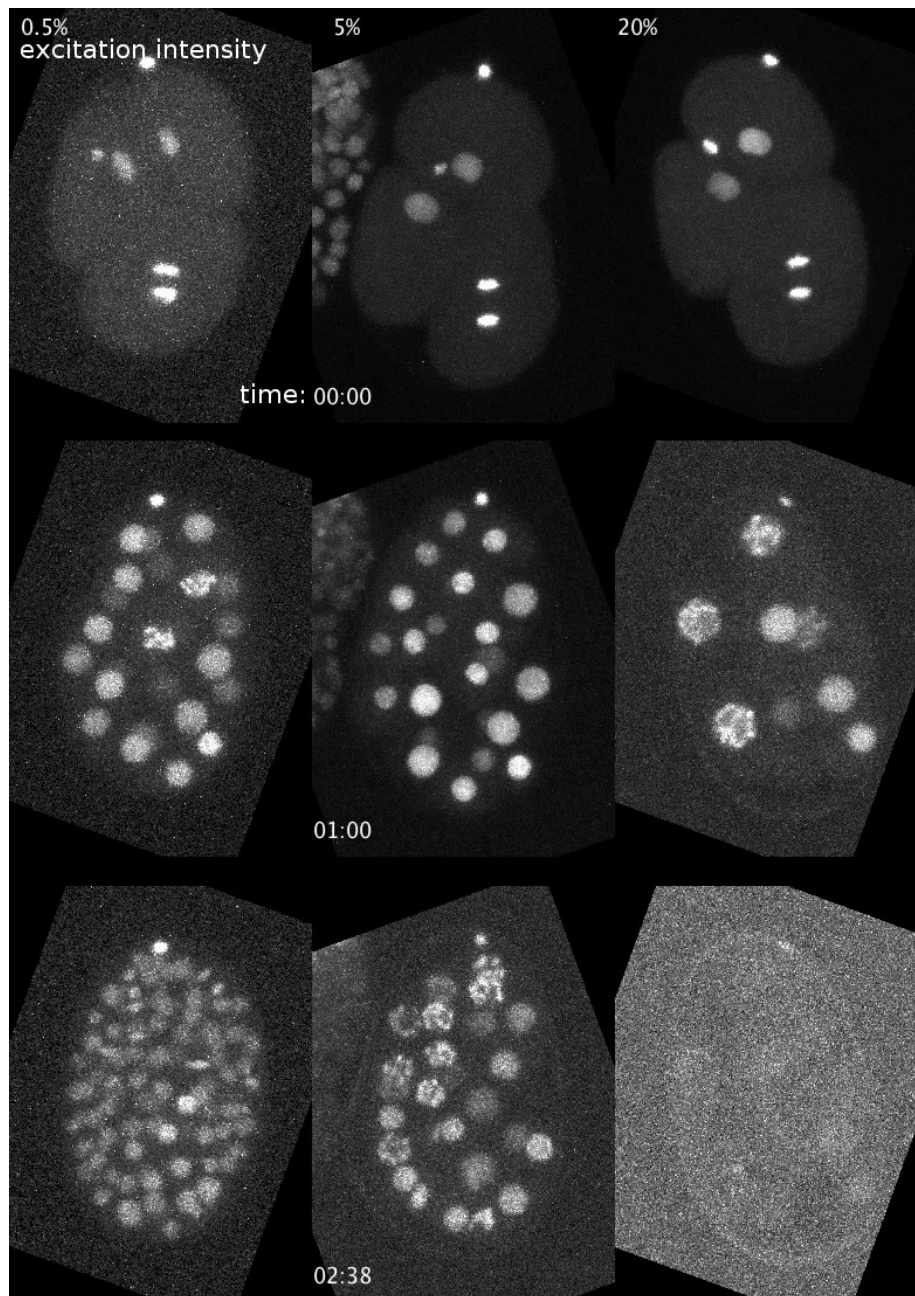


Figure 1.1.: Phototoxic effects while imaging the embryonal development of three *C. elegans* embryos (strain AZ212, histone-2B tagged with eGFP) with different excitation intensities. The embryo with lowest excitation dosage (left) develops fastest. The embryo with the highest dosage (right) ceases development and nearly all fluorophores are bleached after the experiment. Images by J.-Y. Tinevez (Institut Pasteur, Paris, FR).

which was exposed to the lowest dose (left) has developed the largest number of cells. The middle embryo ceased developing while the right embryo died even

1. Introduction

earlier and nearly all its fluorophores are bleached at the end of the experiment.

In Figure 1.2 I reproduce quantitative data from Tinevez et al. (2012). Each data point in this graph corresponds to a two hour time-lapse imaging experiment of a *C. elegans* embryo in a wide-field microscope. From a very low excitation up to a certain threshold dose the development is not affected by the light and approximately 50 cells develop during the two hours.

For a dose above the threshold the development is slowed due to phototoxicity and the number of cells at the end of the experiment decreases.

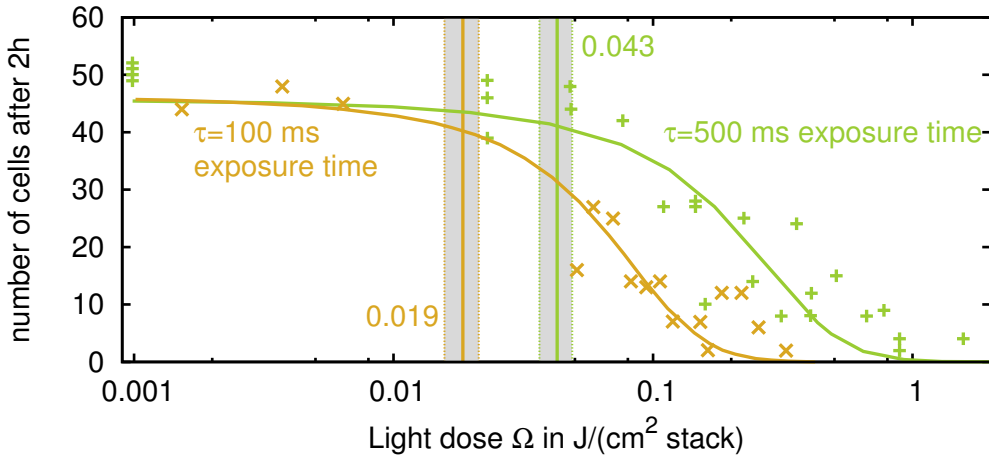


Figure 1.2.: Longer exposure times are less phototoxic. Each data point corresponds to one embryo that developed under a particular excitation dose for two hours. The solid lines are sigmoidal fits to the data. Also indicated are the two phototoxicity thresholds given by the inflection point of the sigmoid and their 95% confidence intervals. This data was provided by J.-Y. Tinevez (Institut Pasteur, Paris, FR) and is also published in Tinevez et al. (2012).

The orange data points in the diagram correspond to a per slice integration time τ of 100 ms and for the green data the integration time is five times higher.

The dose Ω on the x -axis is calculated as

$$\Omega = \frac{\Phi_e n \tau}{A}, \quad (1.1)$$

with integration time τ , area A of the illuminated field, the number of slices $n = 41$ and radiant flux Φ_e of the excitation light, as measured in the pupil.

Naively one would assume that it should not make any difference if the excitation light dose is administered with 100 ms or 500 ms exposures but these data show that a longer exposure time and low intensity are less phototoxic.

1. Introduction

These results agree with an earlier study in tobacco plants (Dixit and Cyr 2003). They investigate cell death a few days after illumination and find that there is a threshold dose below which no phototoxicity can be detected, and that this threshold decreases with light intensity. Dixit and Cyr show that the damage is caused by reactive oxygen species and they explain the shift of the phototoxicity threshold by the limited capacity of the cells' scavenging system for those radicals. They also predict the existence of redox-sensitive checkpoints in the mitotic division cycle.

In summary this section describes how to measure phototoxicity with biological specimen. The next section gives an overview of the underlying photophysics and the rest of this work describes our attempt to build a microscope with reduced phototoxic footprint.

1.2. Photophysical principles of phototoxicity

Here I give a short overview of fluorescence of molecules in order to introduce the terms photobleaching and phototoxicity.

A fluorophore is a molecule that can absorb and subsequently emit light. During the absorption of a photon the molecular orbital transitions from the electronic ground state S_0 to an excited state S_1 . The lifetime of the excited state S_1 is in the order of a few nanoseconds. A Jablonski diagram, as depicted in Figure 1.3, summarizes information about the energy levels of a molecule and possible transition processes.

The majority of known stable and bright fluorophores absorb and emit in the wavelength range between 300 nm and 700 nm. Photons at the high energy end of this range can excite molecules into higher energy levels S_n , ($n > 1$) than the first excited state; these states are unstable and hardly return to the ground state S_0 . On the other side of the spectrum: a molecule that absorbs in the near-infrared (> 700 nm) has a low-lying excited singlet state S_1 and therefore potentially increased reactivity and a high probability for a non-radiative transfer back into the ground state S_0 (Sauer et al. 2011).

The term *Stokes' shift* describes the frequency shift between the absorbed and emitted photon; the energy difference is lost as heat to the fluorophore molecule and surrounding solvent. For the practical implementation of fluorescence microscopes this is significant, as it enables to separate excitation and emission light with a dichroic beam splitter.

1. Introduction

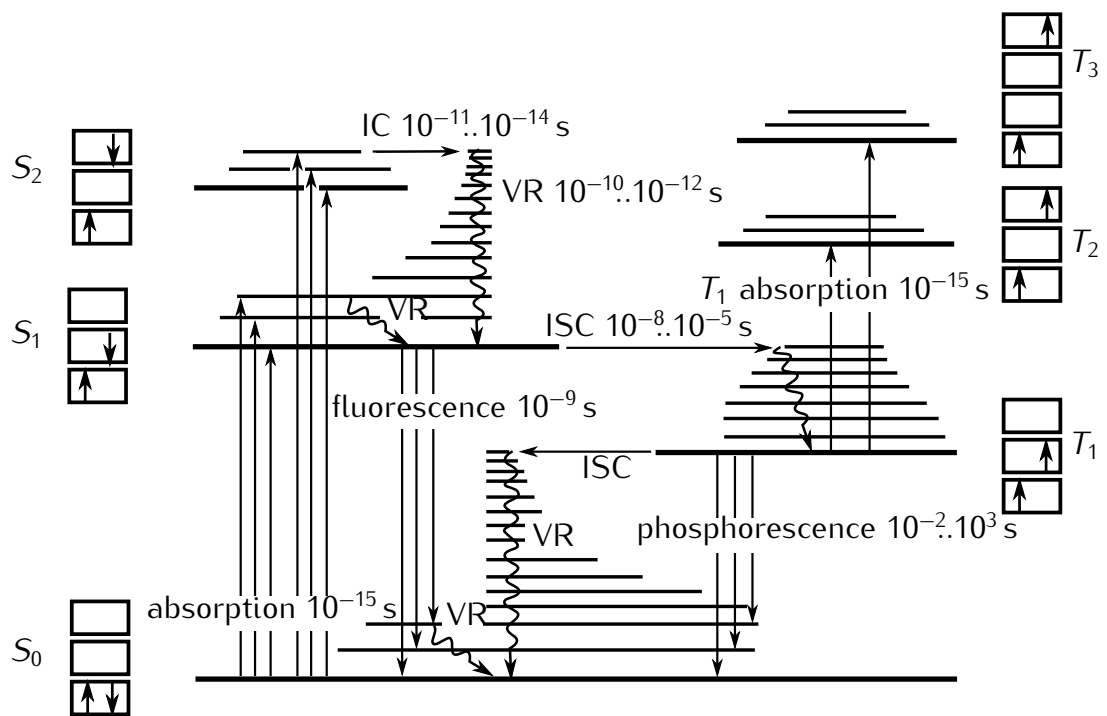


Figure 1.3.: The Jablonski energy level diagram of an illustrative fluorescent molecule. The boxes depict orbitals, up and down arrows symbolize the spin of the outer electrons. Fat horizontal lines represent electronic states. Thinner lines indicate vibro-rotational states. Various processes are shown with their typical time scales. VR = vibro-rotational relaxation, ISC = intersystem crossing, IC = internal conversion (inspired from Haken and Wolf 2006).

The excitation probability of a fluorescence molecule depends on the orientation of its dipole axis relative to the plane of vibration of the excitation field. Especially if the molecule is not rigidly bound to a bigger structure or embedded in a viscous solvent it will reorient its dipole during the fluorescence lifetime and emit the fluorescence photon in a random direction. We use this in the next section to describe image formation in the fluorescence microscope.

The triplet states T_n play an important role in photobleaching. Pure electronic absorption of one photon has no effect on the spin of an electron and therefore the transition from singlet states S_n into the triplet state T_n should not occur. However, interaction with the nuclei can mediate this spin transition. Therefore, in fluorophores this transition has a small probability, resulting in long lifetimes of the triplet state T_1 .

Deschenes and Bout (2002) show that excitation of higher triplet states T_n is the predominant reactive process for photobleaching in vacuum. In particular they

1. Introduction

measured that one rhodamine 6G molecule *in vacuum* can emit more than 1×10^9 photons before it bleaches, if the excitation intensity is low enough ($\sim 1 \text{ W/cm}^2$) to prevent decay over triplet states.

In normal atmosphere the prolonged lifetime of the triplet state T_1 makes it highly likely for the fluorophore to react with molecular oxygen O_2 . Oxygen is abundant and has a triplet ground state $^3\Sigma$ with two unpaired electrons of parallel spin in its π^* -orbitals (see Figure 1.4).

(Bernas et al. 2004)

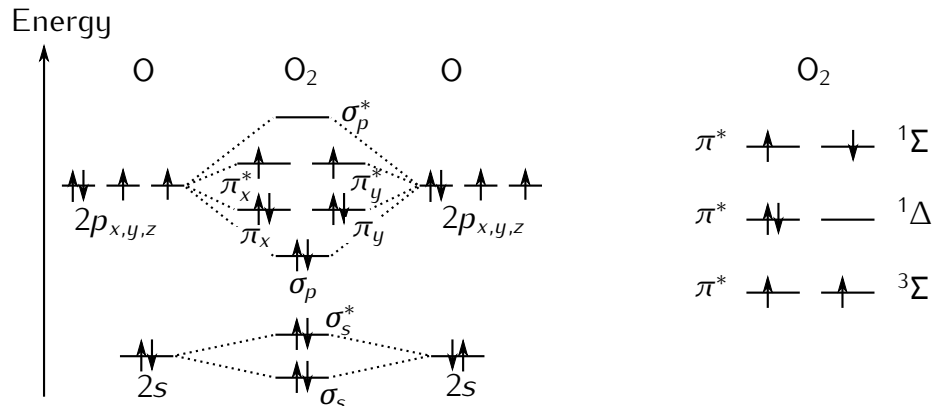


Figure 1.4.: **left:** Schematic that depicts how the orbitals of the oxygen molecule are formed from the atomic orbitals. **right:** Molecular oxygen has the lowest energy in its triplet state $^3\Sigma$ where the spins of the two outer π^* -electrons are parallel. Inspired from van de Linde (2011).

If a ground-state oxygen molecule comes into physical contact with a T_1 fluorophore, the energy of the latter can be transferred by an electron exchange energy transfer mechanism in which the orbitals directly interact with each other (Haken and Wolf 2006, p. 438 and van de Linde 2011).

During this reaction, which is also known as triplet-triplet annihilation, two forms of singlet oxygen form in competition: The lower energy state $^1\Delta$ and the short-lived, higher energy state $^1\Sigma$ that immediately ($T_{1/2} \sim 10^{-9} \text{ s}$) sends out a 1268 nm photon and decays into $^1\Delta$.

The resulting singlet oxygen $^1\Delta$ is very reactive. In a typical specimen it diffuses only a few tens of nanometres until it reacts with another molecule.

(FIXME 2000 greenbaum measures oxygen production, bernas 2004 anoxia gfp)

Nowadays many methods are known to reduce photobleaching: Substitute oxygen with noble gases or remove it enzymatically (Sauer et al. 2011, p. 89), depopulate the triplet state by adding reducing as well as oxidizing agents to the solvent (Vogelsang et al. 2008) or couple a triplet quencher directly to the

1. Introduction

fluorophore (Sauer et al. 2011, p. 19). For fixed samples it helps to change the solvent or polymer.

In living specimen these techniques may reduce photobleaching, but they can also have a detrimental effect on the biological system itself. Removing oxygen will quite certainly have a negative effect. In order to reduce phototoxicity it makes sense to think about the light management in the microscope.

1.3. Conventional microscopes

The wide-field fluorescence microscope does not excite fluorophores of the specimen in an optimal way. In this section I outline how these microscopes work and explain how out-of-focus blur severely limits their performance. I introduce the terms point spread function, optical transfer function and etendue.

1.3.1. Ray-optical description of a large-aperture lens

A microscope, is a device that collects light coming from one plane and forms a magnified image on a camera. Figure 1.5 b) shows a schematic representation of the detection path of a wide-field microscope.

The main components are an objective lens with focal length f and a tube lens TL1 with focal length $f_{TL} > f$. Sample, lenses and camera are arranged in double-telecentric configuration, i.e. the sample is located in the front focal plane of the objective, the tube lens is at distance f_{TL} behind the pupil (i.e. the back focal plane of the objective) and the camera is in the focal plane behind the tube lens.

Light from the sample is collimated by the objective lens and re-imaged by the tube lens. The lateral magnification β is given by the ratio of the focal lengths of the two lenses:

$$\beta = \frac{\overline{O'P'}}{\overline{OP}} = \frac{f_{TL}}{f}. \quad (1.2)$$

Note that in Figure 1.5 b) I represent the objective lens as a single element. This is a simplification.

In the paraxial limit ray-tracing calculations for a thick lens or even several consecutive lens elements can be simplified by bending the ray only at one place — at the principal plane.

1. Introduction

perfect imaging and
high-aperture

Microscope objectives must collect light from a large aperture in order to produce a high resolution image. This is a fact I will support shortly using the wave-optical model. Unfortunately the large ray angles in the objective prevent its simplified description using principal planes, but an analysis using the eikonal theory (Haferkorn and Richter 1984) shows

that an optical system that fulfills the Abbe sine condition allows perfect imaging even for widespread ray bundles.

$$\beta = \frac{n \sin \alpha}{n' \sin \alpha'} \quad (\text{Abbe sine condition}) \quad (1.3) \text{ ?eq:sine-cc}$$

This condition ensures that the focal length, a quantity which is usually defined only for paraxial rays, is equal for all angles. This in turn means that such a lens carries out a Fourier transform from the front to the back focal plane with linear scaling. Note that a lens with a non-linear distortion in the back focal plane will fail to produce an image that is similar to the object.

aplanatic sphere

It turns out that ray bending in a high-aperture lens system that fulfills the Abbe sine condition can be simplified to a one bend at a single surface, quite similar to the utilization of principal planes in paraxial optics. For a high-aperture system this surface is no longer a plane. Instead it is a sphere with radius nf and called *aplanatic sphere*. I depict this surface as two circle segments with bold red strokes on the lenses in Figure 1.5 b).

In addition to the Abbe sine condition microscope lenses are also corrected for spherical aberration and linear coma (Gross et al. 2005). Then the coma rays are symmetric around the chief ray, the wavefront and point spread function are approximately invariant for small field sizes (in first order). This ensures that the imaging conditions are invariant for small regions of the field plane and allows to express image formation with linear systems theory.

1.3.2. Wave-optical theory for image formation in a fluorescence microscope

wave optics

In the following I want to describe how the image on the camera is formed. For this we have to use wave theory because close to the image rays intersect, invalidating ray-optical predictions. As both, wave-optical and ray-optical theory, are very much related, we can give a useful interpretation of the aplanatic surface for wave optics.

plane waves

The underlying Maxwell equations and the wave equation are linear and we can

1. Introduction

represent propagating solutions (evanescent solutions are neglected) of the wave equation as a superposition of the elementary solution — the monochromatic, plane waves described by wave vector \mathbf{k} :

$$u(\mathbf{r}, t) = u \exp(i(\mathbf{k}\mathbf{r} - \omega t)), \quad \mathbf{r} = (r_x, r_y, r_z), \quad \mathbf{k} = (k_x, k_y, k_z), \quad |\mathbf{k}| = 2\pi \underbrace{n/\lambda_0}_{1/\lambda}, \quad (1.4)$$

with vacuum wavelength λ_0 , refractive index n and wavelength λ in the immersion medium.

The accurate treatment of high-aperture optics would in fact require a vectorial calculation of the image for a fluorophore with a particular dipole orientation. Subsequently these images should be averaged to account for random fluorophore orientations, but as I do not need quantitative expressions I limit myself to the simpler scalar problem which provides qualitatively similar results.

Ewald sphere

Assuming that the excited fluorophores in the sample give rise to a monochromatic electromagnetic field — I simplify the problem by omitting the complication that fluorophores emit photons in a wavelength range — then using the spatial frequency vector $\mathbf{v} = \mathbf{k}/(2\pi)$ we can expand the three-dimensional, stationary field amplitude distribution $u(\mathbf{r})$ into its spatial frequency spectrum $\tilde{u}(\mathbf{v})$:

$u(\mathbf{r}) :$	$\mathbb{R}^3 \rightarrow \mathbb{C}$	field distribution in sample space
$u'(\mathbf{r}') :$	$\mathbb{R}^3 \rightarrow \mathbb{C}$	field distribution in image space
$S(\mathbf{r}) :$	$\mathbb{R}^3 \rightarrow \mathbb{R}$	distribution of fluorophores in sample space
$I'(\mathbf{r}') :$	$\mathbb{R}^3 \rightarrow \mathbb{R}$	intensity distribution in image space
$\tilde{u}(\mathbf{v}) :$	$\mathbb{R}^3 \rightarrow \mathbb{C}$	spatial frequency spectrum of field in sample space
$a(\mathbf{r}) :$	$\mathbb{R}^3 \rightarrow \mathbb{C}$	amplitude point spread function
$\tilde{a}(\mathbf{v}) :$	$\mathbb{R}^3 \rightarrow \mathbb{C}$	amplitude transfer function, generalized aperture
$h(\mathbf{r}) = a(\mathbf{r}) ^2 :$	$\mathbb{R}^3 \rightarrow \mathbb{R}$	intensity point spread function
$\tilde{h}(\mathbf{v}) :$	$\mathbb{R}^3 \rightarrow \mathbb{C}$	optical transfer function

Table 1.1.: Overview of the functions that are used in this section.

$$u(\mathbf{r}) = \mathcal{F}(u(\mathbf{v})) := \int_{-\infty}^{\infty} \int_{-\infty}^{\infty} \int_{-\infty}^{\infty} \tilde{u}(\mathbf{v}) \exp(2\pi i \mathbf{r} \cdot \mathbf{v}) d^3 \mathbf{v} \quad (1.5)$$

Where \mathcal{F} denotes the Fourier transform operation. I will use several functions in this section. See Table 1.1 for a listing of their names.

Since we have assumed a monochromatic field and the length $|\mathbf{v}|$ of the spatial frequency vector is the inverse of the wavelength (n/λ_0 , in the material of refractive index n), the support (denoted 'supp') of this spectrum $\tilde{u}(\mathbf{v})$ is limited to the surface

1. Introduction

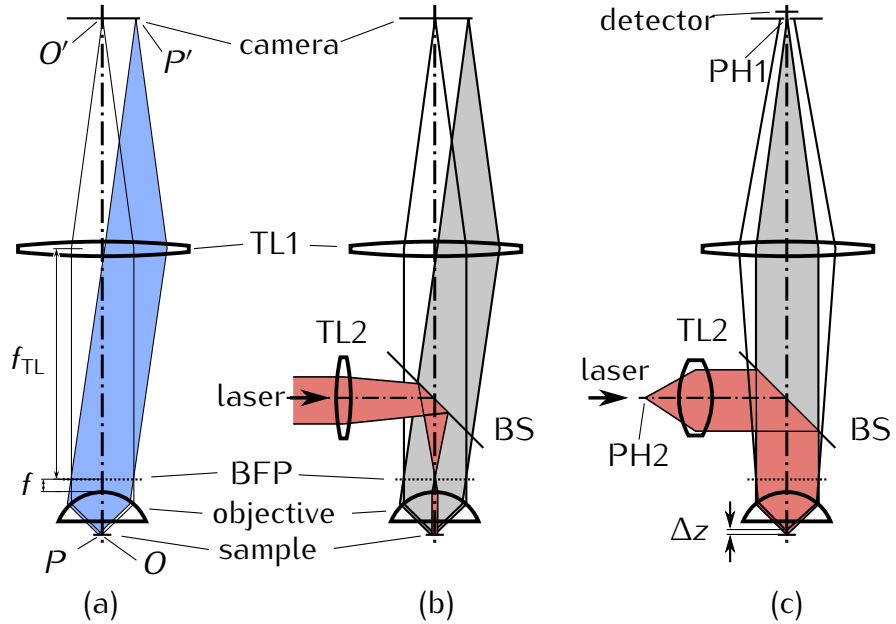


Figure 1.5.: **a)** Segment of the three-dimensional frequency spectrum of the light from the sample that is collected by the objective lens is highlighted in red on the Ewald sphere. **b)** Schematic of the detection path of a modern microscope. The sample is in the front focal plane of the objective. The detection tube lens TL1 forms a magnified image on the camera. The aplanatic spheres for objective and tube lens are indicated in red. **c)** Parallel laser epifluorescence excitation. The excitation tube lens TL2 focuses a laser into the pupil of the objective. The beam is reflected by a dichroic beam splitter (BS) towards the objective. An extended area in the specimen is illuminated. Fluorescence light returns through the objective, is transmitted through BS and forms an image on the camera.

of a sphere of radius n/λ_0 :

$$\text{supp } \tilde{u}(\mathbf{v}) = \{\mathbf{v} \in \mathbb{R}^3 : |\mathbf{v}| = n/\lambda_0\}. \quad (1.6)$$

This sphere is the transfer function of free space, and is also called Ewald sphere. Scaling the Ewald sphere with $f\lambda_0$ gives the aplanatic surface of the lens. Note that the x -component of the marginal ray (in the xz -plane) corresponds to the spatial frequency component $v_x = n \sin \alpha$ in object space and $v'_x = n' \sin \alpha'$ with $n' = 1$ in image space. The transversal spatial frequency components are related due to the Abbe sine condition (1.3):

$$\beta = v_x/v'_x, \quad \beta = v_y/v'_y. \quad (1.7)$$

1. Introduction

The transfer function $\tilde{a}(\mathbf{v})$ of the lens is defined by complex values on the Ewald sphere (McCutchen 1964):

$$\tilde{a}(\mathbf{v}) = P(\mathbf{v}_t) \exp\left(\frac{2\pi i}{\lambda} W(\mathbf{v}_t)\right) \delta\left(|\mathbf{v}| - \frac{n}{\lambda_0}\right) \text{step}(v_z), \quad (1.8)$$

$$\text{step}(x) = \begin{cases} 1 & x \geq 0 \\ 0 & x < 0 \end{cases}, \quad (\text{Heaviside step function}) \quad (1.9) \text{?eq:unit-step}$$

with the Dirac delta function δ , transversal spatial frequency vector $\mathbf{v}_t = (v_x, v_y)^T$, and the real valued pupil function $P(\mathbf{v}_t)$ and wavefront error $W(\mathbf{v}_t)$. McCutchen calls the three-dimensional function $\tilde{a}(\mathbf{v})$ the generalized aperture.

For this discussion I set $W(\mathbf{v}_t) = 1$, i.e. there is no wavefront aberration and the lens is diffraction limited. Furthermore, I use a uniform, solid cylinder as pupil function $P(\mathbf{v}_t)$ in order to limit the size of the calotte (or cap) of the Ewald sphere that is defined by the acceptance angle α of the objective²:

$$P(\mathbf{v}_t) = \text{step}\left(|\mathbf{v}_t| - \frac{n \sin(\alpha)}{\lambda_0}\right), \quad (1.10)$$

with the Heaviside step function as defined in equation (1.9). In general $P(\mathbf{v}_t)$ can assume values between 0 and 1 in order to account for apodization due to natural vignetting or angle-dependent Fresnel reflection losses on the lenses. I ignore such effects in this discussion. Also, just as the objective lens, the tube lens can be described by its generalized aperture but I assume that the tube lens maintains a diffraction limited wavefront of the full angular range. For this discussion, the full microscope is readily described by the generalized aperture of just its objective lens.

Multiplication of the angular frequency spectrum $\tilde{u}(\mathbf{v})$ with the generalized aperture $\tilde{a}(\mathbf{v})$ gives the angular frequency spectrum of the amplitude in the image:

$$\tilde{u}'(\mathbf{v}') = \tilde{u}'(\mathbf{v}/\beta) = \tilde{u}(\mathbf{v}/\beta) \cdot \tilde{a}(\mathbf{v}/\beta). \quad (1.11)$$

Note that I use the transversal magnification β to scale the arguments of the functions, so that the result is given in image space spatial frequencies³.

²Note that this expression is only valid for $\alpha \in [0, \pi/2]$. An expression for $\tilde{a}(\mathbf{v})$ encompassing the full range $[0, \pi]$ for α must contain two functions of each P and W , in dependence on whether the spatial frequency vector \mathbf{v} is directed in or against the direction of the optical axis. This is necessary to express the transfer function of a 4Pi or I^nM microscope.

³Unfortunately my notation is slightly problematic here. I assume that z-sampling occurs by

1. Introduction

According to the convolution theorem this multiplication in frequency space corresponds to a convolution in the domain of spatial coordinates \mathbf{r} of the field distribution $u(\mathbf{r})$ and an amplitude point spread function $a(\mathbf{r}) = \mathcal{F}(\tilde{a}(\mathbf{v}))$ that describes the imaging of the objective lens:

$$u'(\mathbf{r}') = u'(\beta\mathbf{r}) = (u \otimes a)(\mathbf{r}) = \int_{-\infty}^{\infty} \int_{-\infty}^{\infty} \int_{-\infty}^{\infty} u(\boldsymbol{\varrho}) a(\mathbf{r} - \boldsymbol{\varrho}) d^3\boldsymbol{\varrho} \quad (1.12)$$

where $\boldsymbol{\varrho}$ is a spatial coordinate and the lateral magnification $\beta = \mathbf{r}'/\mathbf{r}$ transforms between image space \mathbf{r}' and object space \mathbf{r} . This result shows that the three-dimensional amplitude distribution of the image is linearly related to the amplitude distribution in the sample.

A focal plane detector can only measure the intensity I' which depends non-linearly on the amplitude of the field u' . However, the fluorophores act as independent sources and their phases vary randomly with respect to each other. Each fluorophore gives rise to its coherent image $h(\mathbf{r}')$ (Goodman 1968):

$$h(\mathbf{r}') = |a(\mathbf{r}')|^2. \quad (1.13)$$

The three-dimensional intensity distribution $I'(\mathbf{r}')$ in image space can then be obtained by incoherently adding the individual images of the fluorophores:

$$I'(\mathbf{r}') = \int_{-\infty}^{\infty} \int_{-\infty}^{\infty} \int_{-\infty}^{\infty} S(\boldsymbol{\varrho}) h(\mathbf{r}' - \boldsymbol{\varrho}) d^3\boldsymbol{\varrho} \quad (1.14)$$

$$= (S \otimes h)(\mathbf{r}') \quad (1.15)$$

where $S(\boldsymbol{\varrho})$ represents the three-dimensional fluorophore distribution and $\boldsymbol{\varrho}$ is the spatial coordinate in image space.

It is useful to discuss the Fourier transform of the intensity point spread function h . This is the three-dimensional optical transfer function of the microscope and describes how well different spatial frequencies are transmitted:

$$\tilde{h}(\mathbf{v}') = \mathcal{F}(a(\mathbf{r}') a^*(\mathbf{r}')) = \tilde{a}(\mathbf{v}') \otimes \tilde{a}^*(-\mathbf{v}'). \quad (1.16) \text{ ?eq:otf?}$$

The product of the amplitude point spread function $a(\mathbf{r}')$ and its complex conjugate corresponds to an auto-correlation of the amplitude transfer function in spatial frequency space. Note that the complex conjugation of the second factor $a^*(\mathbf{r}')$

stepping the sample through the object space while the camera is fixed in the focal plane of the tube lens. Therefore the axial coordinates r_z and r'_z in object and image are identical.

1. Introduction

results in an inversion of the argument of $\tilde{a}^*(-\mathbf{v}')$.

This expression allows a geometric interpretation of the support of the optical transfer function $\tilde{h}(\mathbf{v}')$ (Gustafsson et al. 1995). Equation (1.16) describes a convolution of two spherical caps whose open sides are facing each other. The entire covered volume somewhat resembles a torus with vanishing internal diameter. Figure 1.6 depicts a $v_x v_z$ -cross-section for two different aperture angles α . The

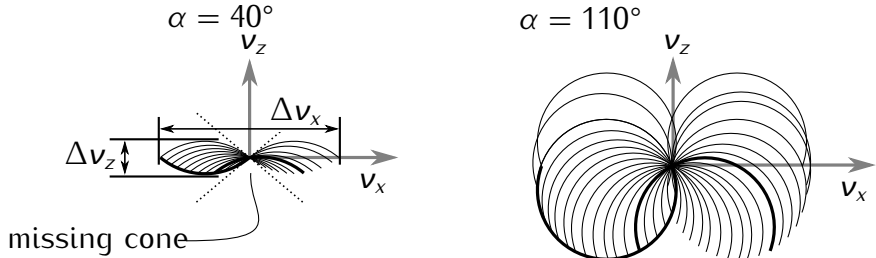


Figure 1.6.: Schematic depicting $v_x v_z$ -cross sections of the support of optical transfer function \tilde{h} for microscope objectives with different collection angles. **left:** Objectives, that only collect light that is directed into one half space, have the missing cone problem. **right:** Optical transfer function for fictional objective with larger collection angle and no missing cone.

lateral Δv_x and axial Δv_z extent of the optical transfer function can be expressed in terms of wavelength λ_0 , immersion index n and aperture angle α :

$$\Delta v_x = \begin{cases} 4n \sin(\alpha)/\lambda_0 & 0 \leq \alpha \leq \pi/2 \\ 4n/\lambda_0 & \pi/2 < \alpha < \pi \end{cases}, \quad \Delta v_z = 2 \frac{n}{\lambda_0} (1 - \cos \alpha), \quad (1.17)$$

resolution

(FIXME verify with rainers book chapter) allow to give lower bounds for the resolution that can be obtained using a well corrected objective:

$$\Delta d_x = \frac{2}{\Delta v_x} = \frac{\lambda_0}{2n \sin \alpha}, \quad \Delta d_z = \frac{2}{\Delta v_z} = \frac{\lambda_0}{n(1 - \cos \alpha)}. \quad (1.18) \text{?eq:resolut}$$

In order to sample the bandwidth limited signal in the image plane correctly, the pixel pitch p_x of the camera must be smaller than half of the resolution: $p_x < \beta \Delta d_x / 2$ (Nyquist criterium). A similar relation holds true for the z -sampling: $p_z < \Delta d_z / 2$. Too large a sampling period will result in aliasing artifacts.

Note that the axial resolution Δd_z is substantially worse than the lateral resolution Δd_x in normal microscope with a collection aperture $\alpha < \pi/2$ that is restricted to only one half-space.

Additionally the optical transfer function of such a microscope is empty in a

1. Introduction

cone shaped region around the axis above and below the origin. This means that in a conventional wide-field microscope it is impossible to bring into focus a (defect-free) fluorescent plane because low spatial frequencies do not attenuate with defocus (Neil et al. 1997). This effect is also called “missing cone problem” (Streibl 1984).

It is instructive to look at a microscope, that is not hampered by the missing cone problem: In image interference microscopy (I^2M) two opposing microscope objectives collect light from the sample and the two detection beam paths are brought to interference using a beam splitter on a focal plane detector. This configuration substantially increases the collection angle, improves the z -resolution and fills the missing cone but puts stringent requirements on the optical path difference between the two interferometer arms, i.e. this device is very sensitive to sample-induced aberrations and in practice, with fluorophores that emit in a broad wavelength range, this method only works for samples which are only a few microns thick (Gustafsson et al. 1999).

Light from the focal plane interferes constructively on the detector, light emitted at $\lambda/4$ distance away from the focal plane interferes destructively, light that is emitted at several wavelengths distance from the focal plane contributes as an incoherent sum to the detected signal. Therefore a z -stack of a fluorescent plane captured with two opposing lenses compared to just one lens will give a signal that is four times as bright in focus, shows damped oscillations (because of the finite spectral band emitted by the fluorophores) when going away from focus and has twice the brightness out-of-focus. This means the axial location of the fluorescent plane can be measured in I^2M but there is still background signal (Gustafsson et al. 1995).

The reason for this background signal is conservation of energy from plane to plane. A light ray that started in a certain object point does not stop in the corresponding image point. Therefore most out-of-focus light is added incoherently as a background to the detected signal. Structured illumination can be used to remove this out-of-focus light (Neil et al. 1997) (FIXME reference to confocal and structured illumination sections).

1.3.3. Illumination in a wide-field epifluorescence microscope

As mentioned in section 1.2, fluorescence photons are essentially emitted in all directions by a typical, (nearly) independent of the original illumination direction. Therefore it is possible and convenient to use the objective for excitation as well

1. Introduction

as detection. This mode of microscopy is called epifluorescence (Greek: $\varepsilon\pi\iota$; on, above). In this configuration usually only a small percentage of the excitation light returns due to scattering or reflection. This simplifies the separation of fluorescence light from excitation light and parts of opaque specimen can be imaged.

The blue beam in Figure 1.5 c) depicts a parallel laser that is focused into the pupil of the objective by tube lens TL2. The beam is reflected at a dichroic beam splitter (BS). This is a glass plate that has been coated with dielectric layers. The refractive index, thickness and sequence of the layers are designed so that the excitation light is reflected towards the objective. Excitation light, that is scattered or reflected in the sample and returns through the objective is reflected towards the light source. However, lower energy fluorescence light returning from the objective is transmitted towards the camera. Behind the objective the beam is parallel and illuminates the specimen. The field of view is the demagnified diameter of the laser beam before TL2.

Non-uniformity due to coherent interference

Note that tiny dirt particles in the excitation beam path can cause coherent interference and produce unwanted non-uniformities in the illumination. As a remedy the spatial coherence of the laser is sometimes reduced. Incoherent light emitting diodes, mercury or xenon arc lamps are often used instead of lasers. In the latter case a band pass filter selects the useful part of the spectrum of the excitation lamp upstream of the dichroic beam splitter.

The space-bandwidth product of a microscopic lens

etendue

A useful quantity in optics is the etendue \mathcal{E} . For a microscope objective its value is related to the number of point spread functions that can be resolved in the field. Therefore this quantity is also called information capacity, light gathering capacity or space-bandwidth product. For a high-aperture lens, the etendue is given by

$$\mathcal{E} = \frac{\pi}{4} (D_{\text{field}} \text{NA})^2, \quad (1.19) \text{ ?eq:high-ap}$$

with the numerical aperture NA and the field diameter D_{field} . The typical image diameter for Zeiss microscopes is 25 mm. For a 63 \times oil-immersion objective with NA = 1.4 this corresponds to a field diameter of $D_{\text{field}} = 0.4$ mm and an etendue

1. Introduction

of $\mathcal{E} = 0.27 \text{ mm}^2/\text{sr}$, where 'sr' denotes steradian, the SI unit of solid angle.

1.3.4. Phototoxicity in conventional microscopes

When imaging living specimen we should distinguish between useful and unnecessary excitation. Taking into account the detection capabilities of objective lenses we should maximize the ratio of in-focus to out-of-focus fluorescence. The epifluorescent wide-field and confocal microscope surely do not represent an optimum in this regard.

In chapter 3 I will introduce other microscopy techniques that are more considerate of where to deposit excitation power within the specimen.

1.3.5. Conclusion

In this section I introduced a theoretical model that describes image formation in a wide-field microscope. For well-corrected, diffraction-limited lenses this process is linear in intensity and three-dimensionally shift-invariant. In order to predict the image of a three-dimensional sample it is sufficient to know the image of a single point source.

By investigating this point spread function and its Fourier transform it is possible to give the simple relationships in equations (1.18) for the best possible resolution. Furthermore I describe the missing cone problem, a limitation inherent in all lenses that only collect light from one half-space.

1.4. Image detectors in wide-field microscopy

I describe the operation of CCD, EM-CCD and sCMOS focal plane detectors. Then I utilize a simple noise model to compare different camera models and describe a simple method to calibrate cameras so that their data is represented in the standardized unit of detected photoelectrons.

1.4.1. Introduction

Nowadays, all wide-field microscopes use silicon-based cameras to measure and digitize the intensity distribution in the intermediate image plane. The semiconductor surface is patterned with a two-dimensional array of PIN photodiodes that generate and collect an intensity-dependent amount of free charge carriers when their depletion region is exposed to light photons.

detection

1. Introduction

quantum efficiency
and back-thinning

Modern detectors can have a very high probability of a photon being absorbed and contributing to final signal (quantum efficiency Q_E). For the most light sensitive devices even the backside of the silicon substrate is removed until the diodes can be exposed from the backside. In this way, the diodes can cover the entire surface and the fill factor is not reduced due to opaque wires running over the surface. Such detectors are called 'back-thinned' and can achieve a quantum efficiency of up to 95% for green light.

There are basically two different technologies to measure and digitize the charge that was collected in the photodiodes:

Charge-coupled
devices (CCD)

In the passive-pixel sensor columns of diodes form a linear row of capacitors. By applying a sequence of different voltages, in the range up to 6 V to each of three adjacent capacitors, the charge can be transported line by line out of the sensor — therefore, this technology is known as charge-coupled device (CCD). An additional row of similar capacitors (denoted horizontal shift register) on one side of the array pushes the carriers into a charge amplifier. This consists of a much smaller capacitor (the read node) and a field-effect transistor that amplifies the voltage across the read node. This voltage linearly depends on the charge (Pawley 2006).

charge amplifier

active-pixel sensor

In the active-pixel sensor each individual photodiode is surrounded by its own transistors for readout and reset. The two-dimensional array is addressed with an access enable wire which is shared by pixels of a line and an output wire, which is shared by pixels of a column. In the simplest case (with three in-pixel transistors) start of integration and readout occurs one line at a time (rolling shutter).

When I started this work in 2008, passive CCD sensors were state of the art detectors for fluorescence microscope with regards to sensitivity and speed. Now, however, faster and cheaper active-pixel sensors that provide comparable or better noise performance, become commercially available.

In the next section I will deal with various noise sources that affect the signal of focal plane detectors. This is not only relevant to compare the performance of cameras from different manufacturers or to determine the optimal parameter settings for one particular experiment; often it is advantageous to specify an intensity measurement as the number of detected photoelectrons, e.g. when comparing images of different microscope systems (confocal, spinning disk or wide-field) or when utilizing sophisticated noise reduction algorithms.

1. Introduction

1.4.2. Photon shot noise and read noise

Photon shot noise

Fluorescence photons arrive at the detector independently of each other. This random process leads to fluctuations in the number of the detected photons and can be described by the Poissonian probability mass function (denoted as 'pois'):

$$\text{pois}(k; \lambda) = \frac{\lambda^k \exp(-\lambda)}{k!}, \quad \lambda \in \mathbb{R}, \quad k = 0, 1, 2, \dots \quad (1.20)$$

Note that in this particular formula the quantities have a different meaning than in other parts of this work. The variable k describes the number of measured photons and the real number λ is the average number of photons that reach the detector during the integration time. Figure 1.7 displays the discrete detection probabilities for three different values of λ . For large $\lambda > 1000$ photons, the shape of the Poisson distribution is excellently approximated by the normal distribution with mean and variance λ . *FIXME quote wikipedia?*

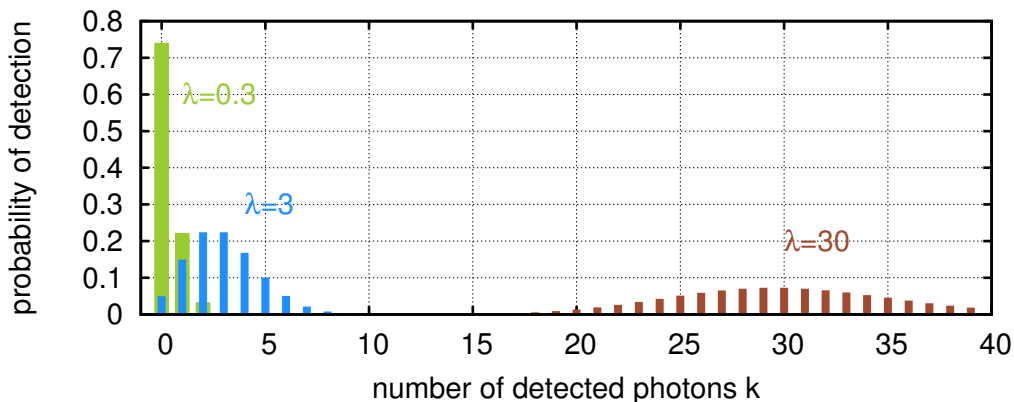


Figure 1.7.: Poissonian probability mass function $\text{pois}(k; \lambda)$ for three photon fluxes with different average photon numbers λ .

We can calibrate every detector in order to specify the measurement in the unit of detected photoelectrons. For this, we utilize the property of the Poisson distribution that the variance $(\Delta I)^2$ of an intensity measurement (in the unit of photoelectrons) is equal to the average intensity $\langle I \rangle$:

$$(\Delta I)^2 = \langle (I - \langle I \rangle)^2 \rangle = \langle I \rangle. \quad (1.21) \text{?eq:variance}$$

detector gain calibration

For the calibration of a detector, twenty images of a defocused fluorescent object (see left image in Figure 1.8) are acquired. From the twenty images the variance of the intensities is determined for each pixel. Then all occurring intensities are

1. Introduction

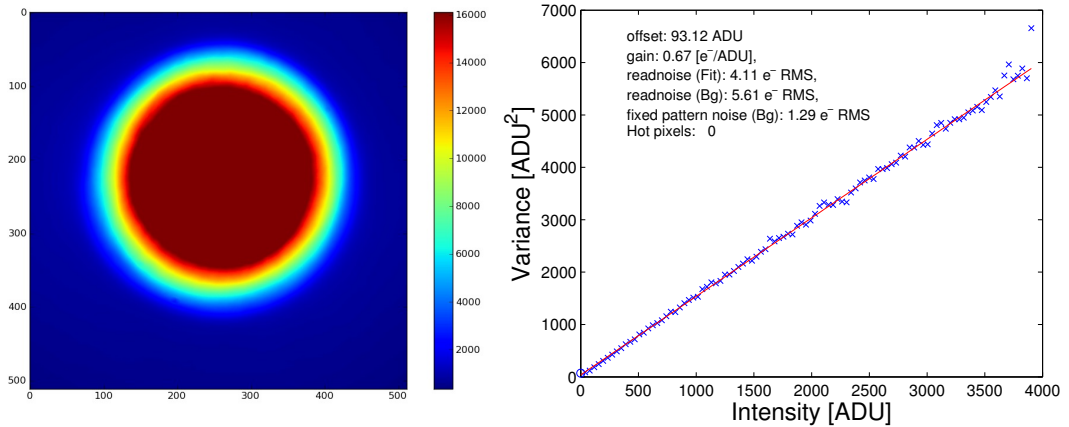


Figure 1.8.: **left:** Image of a defocused area on a fluorescent plane sample. This is used for calibrating the detector. **right:** Result of a detector calibration. The slope of the curve allows to convert the arbitrary analog-to-digital units into detected photoelectrons, the point of interception at the y -axis gives the detector read noise.

collected into 100 bins. The average intensity variance of each bin is then plotted against the intensity (see right image in Figure 1.8). The data lie on a straight line. From its slope we calculate the gain to convert the arbitrary analog-to-digital units into the number of detected photoelectrons. If the data is plotted in this unit, the slope of the line is one, according to equation (1.21). The smooth light distribution in the input images ensures a good coverage for each data point in the variance-intensity plot.

measuring read noise

To determine the quality of a detector we ensure that no light falls on the detector and create twenty dark images. For an ideal, noise-free detector these images would contain zero everywhere. In a real CCD sensor the variance of the values in the dark images reflect the readout noise N_r . Using the calibration gain, the readout noise can be specified as photoelectrons/pixel (e/px).

The analysis for the right diagram in Figure 1.8 gave a readout noise of 5.6 e/px. For the evaluation I used the function `cal_readnoise` of the DIPimage toolbox for Matlab (Lidke et al. 2005). In appendix A.2 I list an alternative Python implementation of this algorithm.

The major source for readout noise is the charge amplifier. Its noise is added uniformly to every image pixel. For readout frequencies above 1 MHz the readout noise increases with the square root of the read speed (Pawley 2006). Until a decade ago this limited the readout speed of scientific CCD cameras. Then a new type of sensor was developed — the electron-multiplying CCD (EM-CCD)

1. Introduction

(Mackay et al. 2001).

electron-multiplying
CCD

This device contains an additional sequence of capacitors (denoted multiplication registers), which are operated with a high voltage (up to 46 V). The field accelerates electrons and they can generate more charge carriers by a process called impact ionization. This is a statistical process and for every electron going through a multiplication register, there is an average probability p that it creates another electron. This probability is quite low ($p < 1.3\%$) but after a sequence of 536 registers the gain $M = (1 + p)^{536} \approx 1015$ is so high, that even readout noise at 17 MHz readout speed can be neglected.

This amplification process consumes a lot of energy and requires an elaborate cooling scheme of the detector chip as the gain is temperature dependent.

Unfortunately, the statistical nature of impact ionization leads to an uncertainty in gain and therefore introduces a new noise source. As a gain this noise acts multiplicatively on the signal. Robbins et al. (2003) analyzed the amplification process and shows that the multiplicative noise, which is also called excess noise, has the effect of halving the apparent quantum efficiency of the detector.

Note that for very low light conditions with a minute probability to detect more than one photon per pixel, the EM-CCD can be run with maximum gain as a binary detector in photon counting mode. In this mode the excess noise has no effect whatsoever; but other noise sources become important.

1.4.3. Comparison chart for detector selection

Now I will introduce a comparison chart that I first saw in Hamamatsu (2012a). It is based on a single formula for the signal-to-noise ratio SNR and if the detector parameters, such as readout noise and quantum efficiency, are known, a quantitative estimate of the expected quality of the data can be made.

Shot noise defines the fundamental limit for the signal-to-noise ratio in photo detectors (Sheppard et al. 2006). As already mentioned above, the expected noise for a signal of S photons is \sqrt{S} . Assuming the contributions to a detector pixel are S photons signal perturbed by an additional number of I_b photons background light. The signal-to-noise SNR_{id} ratio for an ideal, noise-free detector is:

$$\text{SNR}_{id} = \frac{S}{\sqrt{S + I_b}}. \quad (1.22)$$

FIXME wie interpretiert man das bei kleinen S, wenn gauss und poisson verteilung nicht gleich aus sehen?

1. Introduction

A conventional detector with reduced quantum efficiency $Q_E \in [0, 1]$ and additive, Gaussian readout noise with standard deviation N_r (in e/px) can only produce a worse signal-to-noise ratio:

$$\text{SNR}_{add} = \frac{Q_E \cdot S}{\sqrt{Q_E(S + I_b) + N_r^2}}. \quad (1.23)$$

This formula can be adapted for the electron-multiplying CCD. There, the readout noise is reduced because of the gain M but the influence of the shot noise is doubled due to the excess noise factor $F_n = \sqrt{2}$.

$$\text{SNR} = \frac{Q_E \cdot S}{\sqrt{F_n^2 \cdot Q_E \cdot (S + I_b) + (N_r/M)^2}} \quad (1.24)$$

This equation makes it possible to compare all the cameras that I can use for my experiments. Table 1.2 lists parameters from their datasheets and the three diagrams in Figure 1.9 shows curves of the relative signal-to-noise ratio $\text{SNR}/\text{SNR}_{id}$ for three different amounts of background light I_b .

When choosing the parameters I attached particular importance to the noise performance, even if that comes with a loss in readout speed.

camera type	f_{read} [MHz]	QE	N_r [e/px]	F_n	M	model
back-thinned CCD	1	0.95	5.3	1	1	E2V CCD97
EM-CCD	1	0.95	15.0	$\sqrt{2}$	80	E2V CCD97
EM-CCD single photon	17	0.95	89.0	1	1000	E2V CCD97
sCMOS global shutter	200	0.52	2.3	1	1	Fairchild CIS2521F
sCMOS rolling shutter	140	0.72	1.3	1	1	Hamamatsu FL-400
back-thinned sCMOS	—	0.95	0.7	1	1	— ⁴
interline CCD	20	0.62	6.5	1	1	Sony ICX285
interline CCD	1	0.62	2.4	1	1	Sony ICX285

Table 1.2.: Camera parameters for the curves in Figure 1.9.

For a very large number of photons the detector with the highest quantum efficiency Q_E wins (back-thinned CCD, green line):

$$\lim_{S \rightarrow \infty} \frac{\text{SNR}}{\text{SNR}_{id}} = \frac{\sqrt{Q_E}}{F_n}. \quad (\text{high light limit}) \quad (1.25)$$

For detectors with readout noise, there is a signal photon number S_n below which

⁴Back-thinned sCMOS are not available at the time of writing.

1. Introduction

the readout noise predominates:

$$S_n = \frac{N_r^2}{M^2 F_n^2 Q_E} - I_b. \quad (\text{photon shot noise limit}) \quad (1.26)$$

I indicate both limits in Figure 1.9 using different line types. The line is dotted in the region where the readout noise dominates, followed by a thick solid line where both photon shot noise and readout noise contribute. A thin line indicates the region where the relative SNR is within 95% of the high light limit and the sensor's quantum efficiency becomes the parameter that defines the performance.

interpretation of
EM-CCD in Figure 1.9

The first thing I want to look at is the EM-CCD. For a high gain of $M = 20$ the curve is horizontal and the sensor differs from the ideal detector only in terms of a reduced apparent quantum efficiency. In a low background environment $I_b = 0.3$ the electron multiplying mode is only advantageous for signals with less than 30 photons per pixel. For a higher background $I_b = 30$ electron multiplication does not improve noise performance — but note that in this mode the sensor could be read out at a 10 times higher speed.

In a low background environment and low signal level the EM-CCD comes very close to the ideal detector, when it is run in photon counting mode as indicated by the red line in the top left.

sCMOS in Figure 1.9

Next I want to discuss the curves of the active-pixel sensors.

The device designated as global shutter sCMOS is a sensor with five transistors per pixel (Vu et al. 2011). Similar to a passive-pixel CCD sensor this permits to start exposure in all pixels simultaneously, but it has two major drawbacks. The additional two transistors cover space that would otherwise be available as light sensitive area and for quantitative data, a reference frame must be taken for each image, which increases the readout noise (Gamal and Eltoukhy 2005; Hamamatsu 2012a).

The rolling shutter sCMOS sensor has only the minimum three transistors per pixel and therefore a correspondingly higher quantum efficiency. For a signal between 6 and 80 electrons per pixel this sensor provides the best quality at 8 times higher readout speed than the EM-CCD. Rolling shutter means that the pixel lines are read in succession but for our prototype it is crucial that all pixels integrate while the displays show patterns. Fortunately there is a mode called global exposure synchronization which initiates integration in the pixels line by line and generates a trigger output once all pixels have started capturing light. This allows to use the camera as a master without further effort but the camera can also be run as a slave. In that case the only requirement is that the trigger

1. Introduction

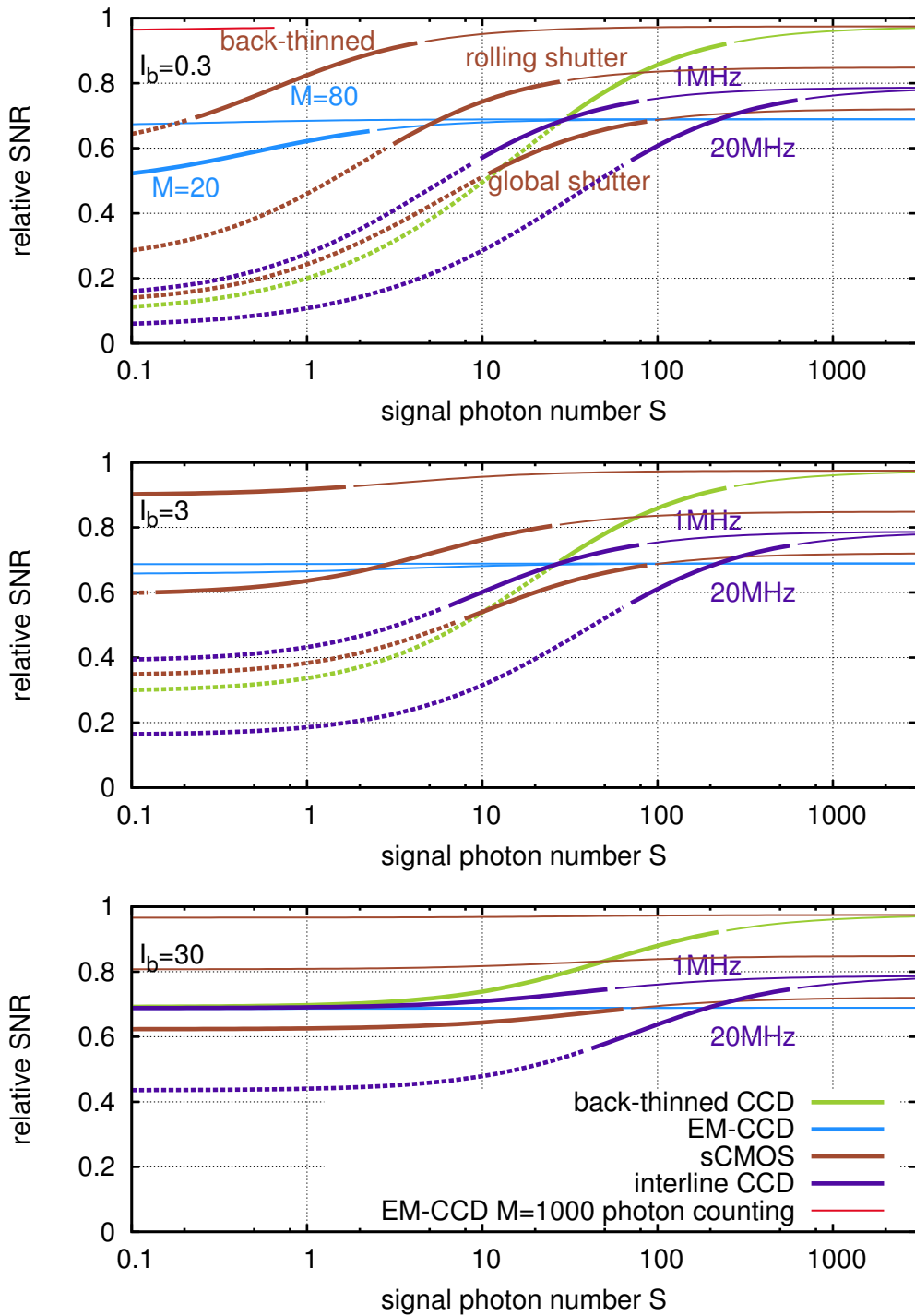


Figure 1.9.: Camera snr. dotted line for lowest light level, where N_r is the dominant noise; thin line indicates high light region where quantum efficiency and excess noise factor F_n matter

comes early enough (10 ms, Hamamatsu (2012b)) to initiate exposure in all lines before the illumination is activated.

1. Introduction

The entry back-thinned sCMOS is only a hypothetical sensor which I added to compare the performance of a low noise active-pixel sensor with near perfect quantum efficiency.

1.4.4. Calibration of the EM-CCD gain

The method I presented for CCD calibration can be applied to measure the gain M and the excess noise factor F_n of an EM-CCD. This requires dark images and image sequences of the smooth intensity distribution (from the exactly the same sample) with and without electron multiplication gain, so that data for both cases can be converted into detected photoelectrons.

The apparent quantum efficiency with gain is Q_E/F_n . Therefore the excess noise factor can be calculated with

$$F_n = N_{(1)}/N_{(M)} \quad (1.27)$$

where $N_{(1)}$ and $N_{(M)}$ are the sum of photoelectrons in the image without and with electron multiplication gain, respectively.

The variance for data without gain is $(\Delta I)_{(1)}^2 = Q_E \langle I \rangle$ and smaller than for data with gain, where the variance is $(\Delta I)_{(M)}^2 = Q_E F_n^2 \langle I \rangle$.

The x -axis in the intensity-variance plot is equal to the intensity for gain-free data and scaled with M for the amplified data. The gain M can be calculated from both slopes $m_{(1)} = Q_E$ and $m_{(M)} = Q_E F_n^2/M$ of the intensity-variance curves:

$$M = F_n^2 \frac{m_{(1)}}{m_{(M)}}. \quad (1.28)$$

In appendix A.1 I show code to automatically measure data for this calibration. In order to cover a large span of gains, I capture a short exposure image before each measurement and adjust the exposure time such that the sensor is never overexposed.

Table A.1 summarizes the calibration results. The average of the dark images (in ADU) is given in the column offset. The read noise in conventional mode is approximately 8 electrons per pixel rms. The column mean' contains the average number of photoelectrons per pixel in the illuminated image normalized by the integration time. The rows conv1 and conv2 with conventional readout (without EM-gain) contain approximately the same number. This proves that no significant bleaching occurred during the experiment.

1. Introduction

1.4.5. Conclusion

In this section I discussed how various camera sensors work. I have explained photon shot noise, which follows from the quantum mechanical nature of light and so far constitutes a fundamental limit of light detection. Based on this, I explained a calibration method that helps to evaluate camera performance and, maybe more relevant for this work, allows to compare images that were created with different microscopes.

Since low-noise active-pixel cameras became available only late during my project, and the first models still had some issues — unstable software or in the case of the Hamamatsu Orca Flash 2.8 too few outputs for trigger signals, I designed my system for EM-CCD. For most experiments, however, I used an interline CCD.

2. Methods of controlling illumination patterns

2.0.6. 2-photon laser scanning fluorescence microscopy

If the laser intensity in the focal spot of a confocal microscope is sufficiently high, then two infrared photons can be absorbed within $\sim 5\text{ fs}$ and excite the same electronic state.

In this regime, the fluorescence emission increases quadratically with laser intensity. This non-linearity confines the excitation volume to the vicinity of the focal plane (Denk et al. 1990). Fluorophores outside of this region are not excited. Therefore this method produces sectioned images by default and there is no need for a detection pinhole.

As an additional benefit infrared light is scattered less than visible light of half the wavelength. This increases penetration depth and image quality. Photodamage outside of the focal volume is unlikely and phototoxicity is much lower, compared to the single-photon confocal microscope, when z-stacks are acquired.

However, the phototoxicity within the focal volume is higher and techniques like ultramicroscopy (section 3.1) with single-photon excitation are preferable, when low overall phototoxicity is a requirement.

2.1. programmable array

Caarls et al. (2011)

3. Other approaches of light control

This chapter gives an overview of current microscopy techniques that reduce unnecessary fluorescence excitation and reduce phototoxicity. In *light sheet microscopy*, an oblique sheet of light illuminates the sample without exposing too many out-of-focus fluorophores. *Controlled light exposure microscopy* (CLEM) takes into account the in-focus fluorophore distribution and iteratively improves the signal-to-noise ratio of the measurement. Finally, *light field microscopy* allows instantaneous and complete control of all parameters of the incoherent light exposure.

3.1. Light sheet fluorescence microscopy

Light sheets can be directly created with separate optics to illuminate the sample from an orthogonal direction. Another promising method to create a sheet is to use a high numerical aperture objective near the total internal reflection angle. Diffraction couples the minimum width of the sheet and the extent of the area, where the sheet's width is constant. There is a trade-off between sheet width and field of view.

The idea of illuminating a sample from the side dates back quite far into the history of microscopy. Already one hundred years ago, an objective perpendicular to the detection objective was used for illumination of the focal plane in the specimen. This dark field technique was used to characterize gold nano particles in gold ruby glass (Siedentopf and Zsigmondy 1903).

Eventually this technique was applied to fluorescence microscopy. First to analyze cochlea specimen (Voie et al. 1993) and more recently for the development of embryos (Huisken et al. 2004). Results in the latter paper have sparked interest in the technique at many labs (Santi 2011).

3.1.1. Light sheet generation with cylindrical lens

Figure 3.1 shows how the light sheet can be focused into the specimen using a cylindrical lens. Huisken et al. (2004) employ a water dipping objective with

3. Other approaches of light control

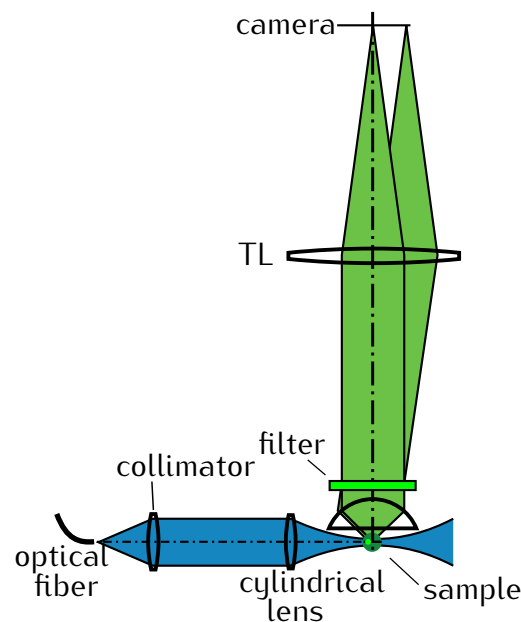


Figure 3.1.: Schematic of SPIM (selective plane illumination microscopy). A cylindrical lens illuminates the specimen with a thin sheet of light along the focal plane of the objective. Rotating the sample and/or moving it along the axis allows to reconstruct a sectioned three-dimensional volume of the fluorophore concentration with improved light utilization compared to conventional microscopes (inspired from Huisken et al. 2004).

long working distance (1...2 mm) and comparatively low NA for detection. A 10 \times objective with 660 μm field of view diameter is used with a sheet thickness that varies less than 42% (6...8 μm). The light sheet not only improves sectioning and contrast but also improves the axial resolution from originally 14 μm by nearly a factor of two.

The axial resolution of detection objectives of higher numerical aperture isn't improved so easily over an extended field of view. Shading effects, diffraction and refraction can deteriorate the light sheet. As an improvement of the technique it was suggested to rotate the specimen or illuminate with multiple sheets of light from different directions.

Other improvements involve a Bessel beam that is scanned to illuminate a plane. This intensity distribution is "self-reconstructing" and can compensate better for obstacles in its path. It comes with the cost that the light sheet isn't as confined. Simultaneous structured illumination and 2-photon effects were suggested to improve this.

A major difference between this technique and conventional microscopy tech-

3. Other approaches of light control

niques is the way the sample is mounted. Usually a specimen is placed with a drop of embedding medium on a $170\text{ }\mu\text{m}$ thick coverslip. Then it is flipped onto a microscope slide and sealed with nail varnish. This approach of mounting the sample does not work for an ultramicroscope. There the sample has to be accessed from two perpendicular sides. Often the specimen are embedded in an agarose cylinder or sometimes, they are fixed in a liquid-filled chamber.

3.1.2. Light sheet generation using the detection objective

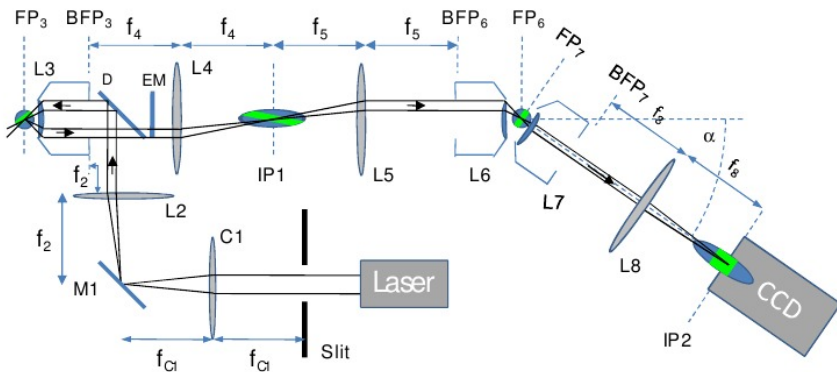


Figure 3.2.: Schematic of oblique plane microscopy (OPM). An index matched sample is excited using an oblique plane of light. The illuminated plane is tilted relative to the focal plane. Therefore out-of-focus fluorophores on the periphery of the field of view are excited. Two additional objectives in the detection path are used to reconstruct an aberration free image of all the excited fluorophores (drawing from Dunsby (2008)).

Modern high numerical aperture objectives allow to illuminate an *index matched* sample with a half angle of up to 70° . This enables illumination of an oblique and thin sheet of light in the sample just as in selective plane illumination microscopy. However this technique (oblique plane microscopy, OPM) has the advantage, that only one objective is needed in order to be close to the sample and it will work with specimen in conventional microscope slides. However, one difficulty is that the excited fluorophores are severely defocused in the intermediate image plane (see Figure 3.2). Dunsby describes how to rotate the observational plane optically in order to recover an aplanatic image from the oblique illumination plane (Dunsby 2008). They re-image the sample through two additional objectives.

Biological specimen are often not index matched and have a lower index $n_e \approx 1.33 \dots 1.45$ than the immersion oil $n = 1.52$. As indicated in Figure 3.3, the

3. Other approaches of light control

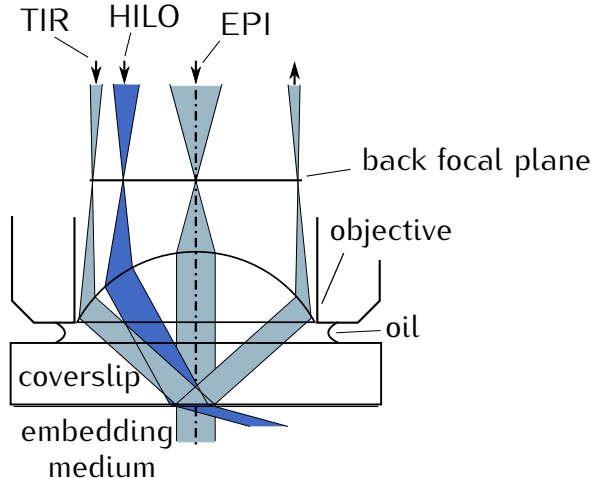


Figure 3.3.: Schematic of rays in HILO (highly inclined and laminated optical sheet) technique. The specimen is embedded in a medium of lower optical density than the cover slip. For a very high illumination angle (point on the periphery of the back focal plane), the light would be reflected at the cover slip-medium interface due to total internal reflection. For HILO, a point on the back focal plane that is closer to the optic axis is illuminated. The light enters the embedding medium at a highly inclined angle and only a thin sheet in the focal plane is illuminated (inspired from Tokunaga et al. 2008).

refraction at the interface between cover slip glass and embedding medium can be exploited to illuminate the specimen with a light sheet that is nearly parallel to the focal plane. This technique is called highly inclined and laminated optical sheet microscopy (HILO) (Tokunaga et al. 2008; Konopka and Bednarek 2008).

Note that the index mismatch between embedding and immersion medium will introduce aberrations (mostly spherical) which will limit the imaging depth.

3.2. Scanning techniques for improving light utilization

In section 2.0.6 we already introduced the 2-photon microscope. Its phototoxicity and speed can be improved with the methods that are described in the following two subsections.

3.2.1. Controlled light exposure microscopy (CLEM)

The confocal microscope (see Figure 1.5 c) allows another adaptive illumination technique. Each point in the focal plane of the specimen is treated as one of the following three cases: point with no fluorophores (A), high concentration of fluorophores (C) or an intermediate (B).

3. Other approaches of light control

Ideally, points of type (A) that do not contain fluorophores should only be exposed until fluorophore content is ruled out. The other two classes (B) and (C) should be exposed until a fixed number of fluorescence photons have been detected (C) or a maximum integration time has been reached (B). Unfortunately, due to the photon nature of light, sometimes a region of type (B) is incorrectly treated as (A) which introduces dark pixel artifacts in the image (Hoebe et al. 2010).

In conventional microscopes, areas of class (C) with high fluorophore concentration are generally exposed too much. Their signal-to-noise ratio would be high, but this doesn't increase the perceived image quality. Furthermore, the regions above and below the focal plane are unnecessarily subjected to high exposure.

The CLEM approach was first presented by Hoebe et al. in 2007, followed by an independent similar version with adaptive control of the laser power for 2-photon microscopy by Chu et al. (Hoebe et al. 2007; Chu et al. 2007).

3.2.2. Acousto-optic deflectors for fast beam steering

In a conventional confocal microscope, the beam is steered by two galvanometer mirrors. This technique offers very good light throughput and is sufficient to obtain rectangular images. However, the inertia of the mirrors severely limit the access rate of spots in the focal plane.

Replacing the mechanical mirrors with an acoustic wave in a transparent material (TeO_2) enables $4\ \mu\text{s}$ switching time (Otsu et al. 2008) and even allows refocusing (Reddy et al. 2008). These acousto-optic deflectors have lower efficiency than mirrors (70% for two AODs) and show chromatic aberrations.

However, as descanning isn't necessary in 2-photon microscopy, the lower efficiency (in the excitation path) is hardly an issue. Therefore, this technique for the first time enables "random access" of three-dimensional coordinates in the sample.

3.3. Non-scanning techniques

3.3.1. Direct illumination

An obvious method for doing spatial control is to image a two-dimensional array of high-power micro-LEDs into the specimen. However, the problem is to achieve sufficient *irradiance* and *fill factor*. The angular emission profile of LEDs is often

3. Other approaches of light control

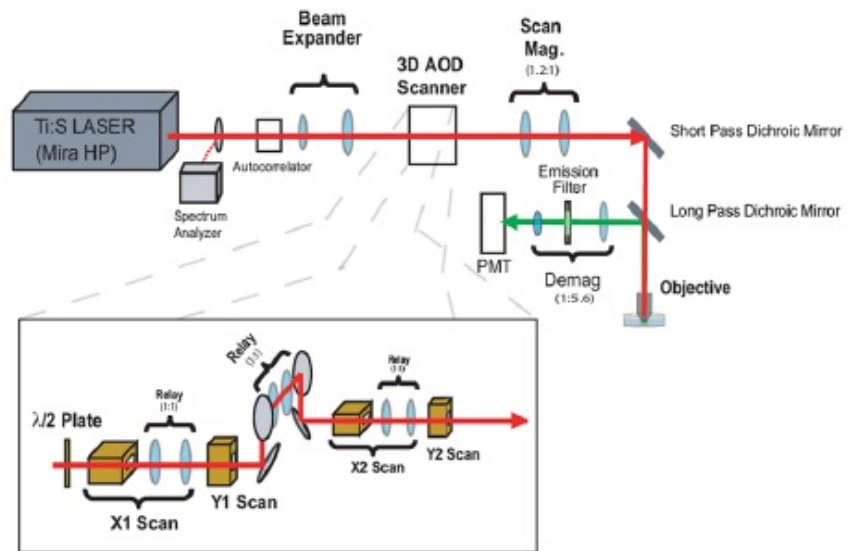


Figure 3.4.: Schematic of an acousto-optic deflector (AOD) illumination system with z -focusing. Figure taken from Reddy et al. (2008)

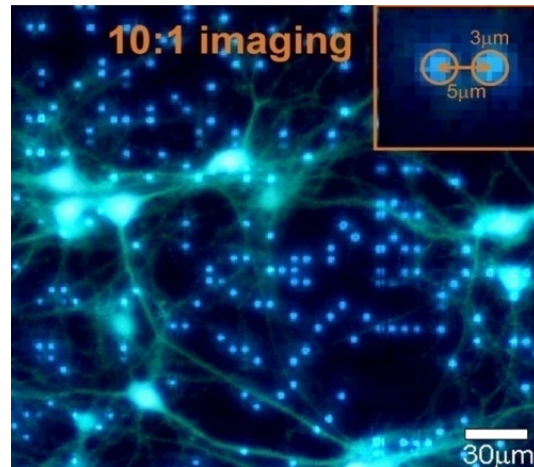


Figure 3.5.: An overlay combining wide field micro-LED illumination and fluorescence imaging YFP tag expressed in neurons, taken from Grossman et al. (2010).

Lambertian, i.e. the back focal plane of the objective would be over-illuminated and a lot of light would be lost. The fill factor is limited because it is difficult to put a lot of LEDs close to each other. The technique has been demonstrated using a 64×64 array of $20 \mu\text{m}$ micro-emitters with $50 \mu\text{m}$ pitch (Grossman et al. 2010). The LEDs can be switched at millisecond speed and emit at $(470 \pm 22) \text{ nm}$.

LED arrays enable interesting experiments where processes are influenced by light, i.e. optogenetics, but the targets ideally have to be located in the focal plane. Also, it must be verified that the illumination cone of each LED image

3. Other approaches of light control

doesn't affect the measurement, i.e. activate the specimen in the out-of-focus regions.

Nevertheless, once the LED or VCSEL arrays become available in interesting spectral ranges, we might see the direct illumination techniques more often.

3.3.2. Intensity modulation

Programmable array microscopy

A technique similar to controlled light exposure microscopy (CLEM, section 3.2.1) has been implemented in a programmable array microscope (PAM) (Caarls et al. 2011). Like our microscope, the PAM images a pattern into the sample using a spatial light modulator. Contrary to our system, the same SLM is used in the detection path to recover an image of the in-focus fluorophores.

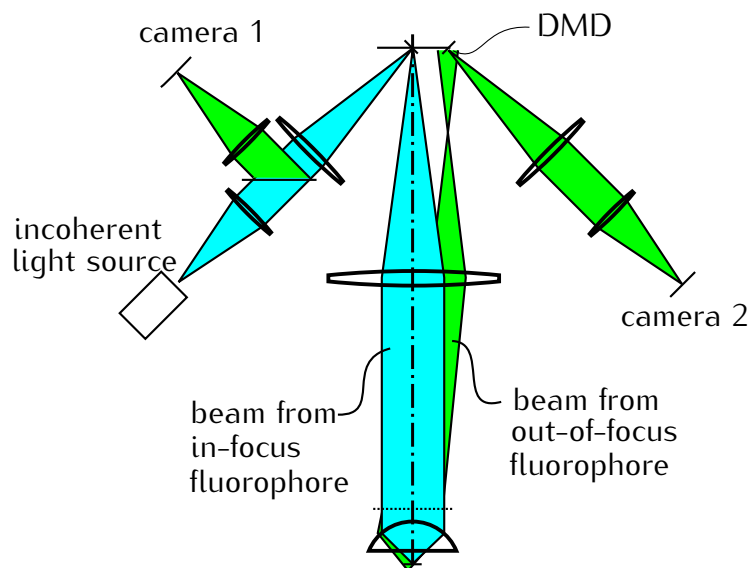


Figure 3.6.: Schematic of a programmable array microscope (PAM) (inspired from Verveer et al. 1998). A digital micro mirror device (DMD) containing an array of tiltable mirrors is imaged into the focal plane of the objective. Returning fluorescent light from out-of-focus fluorophores is distributed onto both the cameras. In-focus fluorescence is only imaged onto camera 1.

Light field microscopy

Interesting work on light fields originally started in the macroscopic domain of cameras (Lippmann 1908) and was eventually applied as a technique for microscopy

3. Other approaches of light control

(Levoy et al. 2006, 2009; Zhang and Levoy 2009). This approach is built on imaging through an array of microlenses.

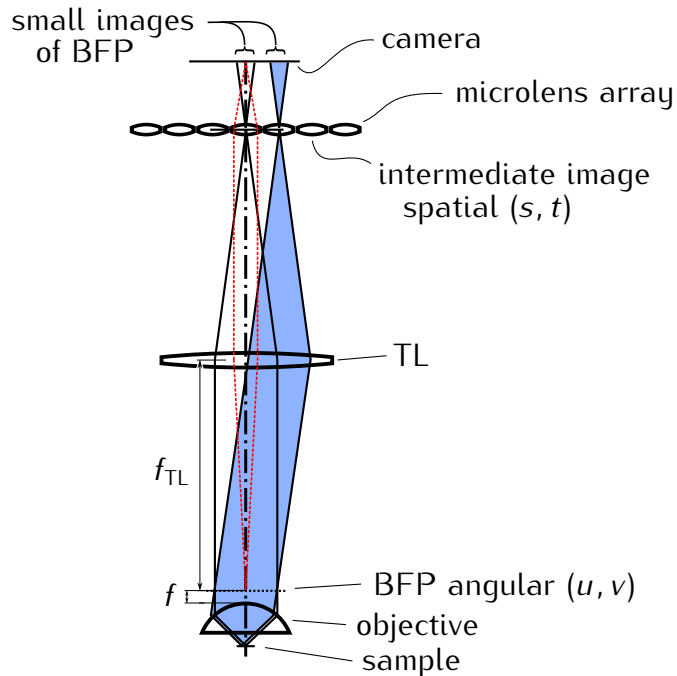


Figure 3.7.: Schematic of microlenses in intermediate image plane (inspired from Levoy et al. 2006)

A microlens array is placed behind the intermediate image plane (see Figure 3.7). The light that illuminates one microlens corresponds to one spot in the focal plane of the sample. The camera is positioned in the focal plane of the microlenses and captures an image of the back focal plane behind each microlens (see red ray bundle in Figure 3.7).

The camera captures the four dimensional light field, leaving the specimen with spatial coordinates (s, t) and angular coordinates (u, v) . This data enables computational viewpoint shifting, refocusing, extended depth of field and aberration correction of the detected fluorescence emission.

Figure 3.8 shows a bundle of rays originating from an out-of-focus point. Each of the microlenses that are hit by the circle of confusion, re-image a fraction of the angular range into a small image. This process is crucial because a lot of the original image information is lost here. The intensities from the sub-images on the camera can't later be recombined in order to, say, recover a high resolution image of the defocused point (priv. comm. R. Heintzmann).

Additionally the light field microscope doesn't utilize the full resolution of high-NA objectives. This will prevent the use of this technique in its current form

3. Other approaches of light control

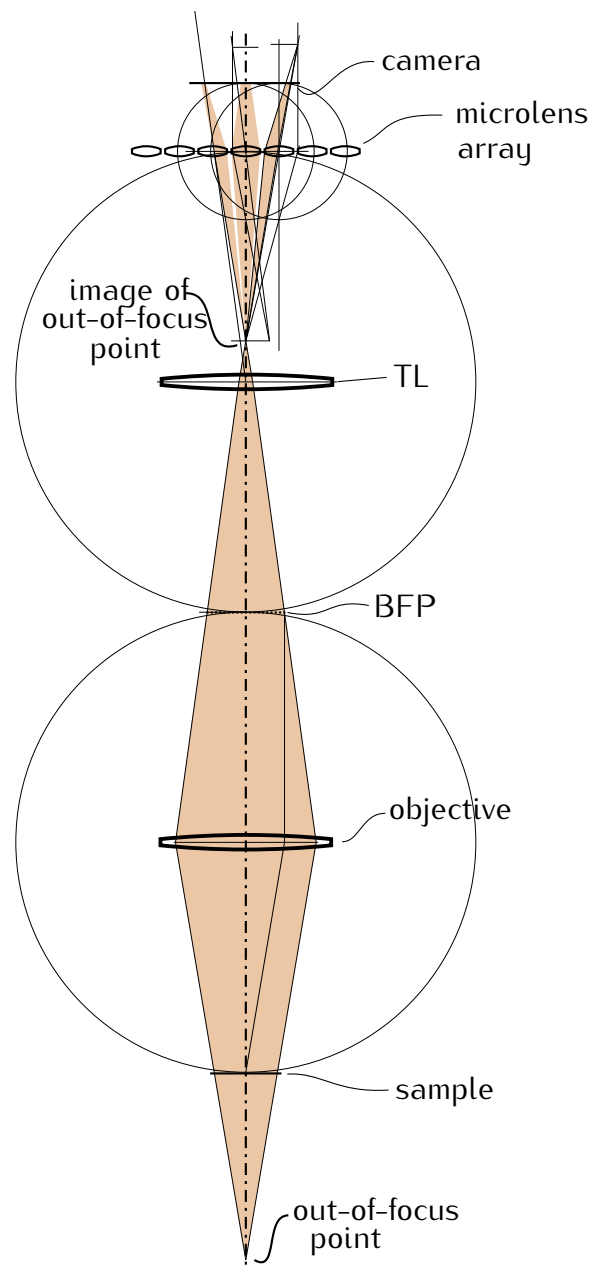


Figure 3.8.: Construction of an out-of-focus ray bundle through the light field microscope. In order to improve the readability of the drawing, the magnification in the microscope was set to 1 : 1 (focal lengths of tube lens and objective are equal). An on-axis sample point originating from below the focal plane of the objective is imaged onto an on-axis point between the tube lens and the microlens array. Three of the microlenses re-image this on-axis image point into three points behind the plane of the camera, i.e. the images behind the three microlenses will contain bright blurry spots at different positions relative to their centre.

3. Other approaches of light control

in the detection path of microscopes. When the microlenses are small enough, to obtain a high resolution image of the sample, then the angular resolution diminishes.

However, the same idea can be applied in the excitation path (Levoy et al. 2009). For illumination purposes, lower resolution will often suffice. The light-field technique allows unique control of excitation light intensity and angles at each point of the sample plane.

3.3.3. Temporal focusing

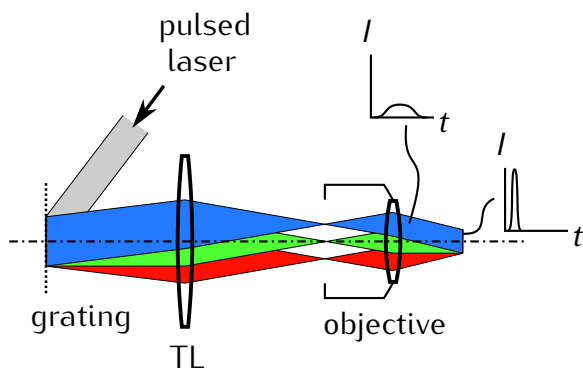


Figure 3.9.: Schematic of temporal focusing (inspired from Oron et al. 2005). A grating in the intermediate image plane separates the pulse into its spectral components. The out-of-focus areas of the specimen are illuminated with a longer pulse. Only in the focal plane, all spectral components interfere coherently and form a short intensive pulse.

The axial extent of ultra-short laser pulses can be as thin as a few microns. A parallel beam can be split into different spectral components by a grating in the intermediate image plane (Oron et al. 2005). The tube lens focuses the diffraction pattern into a line in the back focal plane of the objective.

The objective, which has to be corrected for chromatic aberration and dispersion, then focuses all the beams onto the focal plane. Different spectral components arrive in the focal plane at the same time. The out-of-focus points see an extended illumination. For a high NA objective, a pulse duration of $\tau = 20\text{ fs}$ results in a slice of $z \approx \tau c/2 \approx 3\mu\text{m}$ thickness around the focus, where the beam has significant intensity.

Using this technique it is possible to build a wide field 2-photon microscope. That only excites fluorophores within the focal plane. The technique can be further improved by spatially modulating the beam in the intermediate image

3. Other approaches of light control

plane for CLEM like performance. This technique has been implemented in the TF-GPC approach and will be discussed in the next section.

3.3.4. Phase modulation

Digital holography

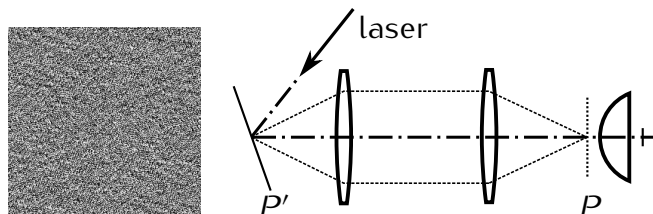


Figure 3.10.: Schematic of spatial illumination by phase holography. A phase-only SLM displays a hologram in the plane P' which is conjugated to the back focal plane P of the objective (inspired by slide from V. Emilian).

Certain types of liquid crystal spatial light modulators can be used to modify the phase of light. When such a device is placed into the back focal plane of a lens, it is possible to control the light distribution in its front focal plane. An iterative algorithm (iterative Fourier transform algorithm, IFTA) can be used to establish a phase image on the liquid crystal display that will result in an intensity distribution in front of the lens.

This approach has been used to excite a two-dimensional pattern in the specimen (Lutz et al. 2008; Zahid et al. 2010) and is advantageous especially for cases where only small parts of the specimen ought to be illuminated. As opposed to conventional intensity spatial light modulators, the light can be redirected from dark areas into the bright areas.

There is also a limited possibility to create three-dimensional patterns, e.g. several points below, in and above the focal plane by displaying Fresnel zone planes. For illumination, usually a laser with non-zero interference length is employed. However, this illumination contains an unwanted “speckle” pattern in the form of noisy non-uniformities. To a certain extent, the contrast of the speckle pattern can be reduced by controlling spatial and temporal coherence of the illumination (sweeping the frequency of the laser or changing illumination direction while the detector is integrating).

Holographic control can be used with 2-photon excitation as well (Nikolenko et al. 2008), but this exacerbates the effect of speckles.

3. Other approaches of light control

Generalized phase contrast (GPC)

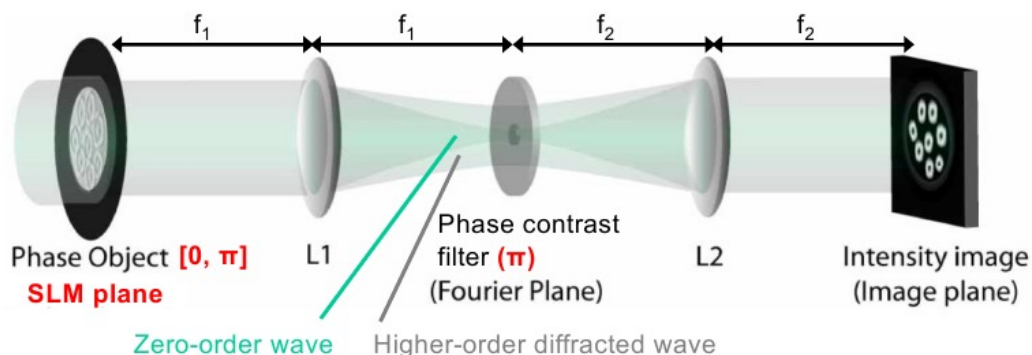


Figure 3.11.: Schematic of generalized phase contrast (from Rodrigo et al. 2008).

A phase contrast microscope objective can be used to convert a phase image from the intermediate image plane into an intensity image in the specimen (Rodrigo et al. 2008). Compared to digital holography, hardly any computation is necessary. Yet, the phase spatial light modulator allows to concentrate a lot of light even on a small region of the specimen as opposed to other techniques, which involve intensity modulation and lose all the light of dark areas by sending it into a beam block or something similar.

The generalized phase contrast method is suitable even with spatially incoherent illumination. However, when the fill-factor – the size of the bright area in the image – changes, the phase contrast filter must be changed.

Generalized phase contrast and temporal focusing (TF-GPC)

The combination of generalized phase contrast and temporal focusing allows spatially controlled illumination of in-focus areas (Papagiakoumou et al. 2010). Usage of a phase spatial light modulator results in high light efficiency compared to intensity modulation. Splitting and recombination of the spectral components of the pulse reduce speckle noise considerably.

3. Other approaches of light control

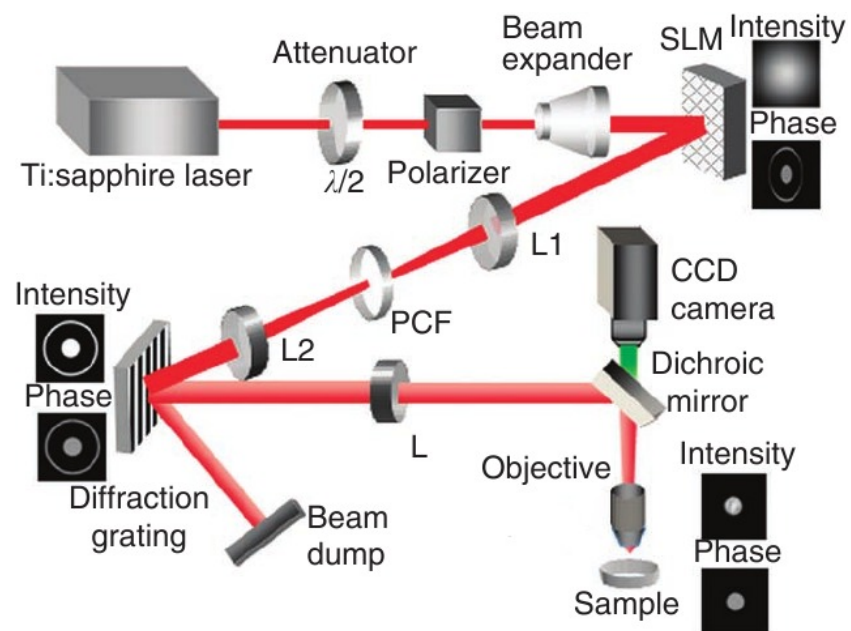


Figure 3.12.: Schematic of phase contrast with temporal focusing (TF-GPC) (from Papagiakoumou et al. 2010), PCF is a phase contrast filter.

4. The concept of spatio-angular microscopy

Here I introduce the spatio-angular microscope. First I explain the concept of its illumination system using exemplary fluorophore distributions, that occur in typical specimen.

Then I describe some decisions we faced during the initial design phase concerning the arrangement of optical components. Furthermore, I position our method among known approaches of light control for microscopy. Of all published techniques for excitation illumination control, the light field microscope (Levoy et al. 2006) comes closest to our approach. I explain differences between both techniques and discuss their respective pros and cons. I address the peculiarities and limitations of the hardware components in chapters 5 (optics) and ?? (micromirror based pupil plane SLM). Initially, the details would be detrimental to clarity.

The effective use of the spatio-angular microscope, requires more knowledge about the specimen than a conventional or a SPIM microscope (Huisken et al. 2004). Ideally, the distribution of refractive index and fluorophores in the specimen should be known. If these parameters were precisely known, there would be no need for an image in the first place. However, while imaging a known specimen, sufficiently good predictions of these parameters can often be made. The higher the accuracy of these prognoses, the greater the reduction in phototoxicity will be.

The computer-based selection of appropriate illumination masks requires the prediction, or at least an approximate estimation, of the three-dimensional distribution of light in the specimen.

In the last part of this chapter, I describe the computational control loop in our spatio-angular microscope and touch topics of image processing.

4.1. Motivation

In order to introduce the basic idea underlying the spatio-angular microscope, I consider the distribution of excitation light in the object of a conventional

4. The concept of spatio-angular microscopy

fluorescence microscope: Figure 4.1 a) schematically illustrates the side view of the excitation beam path through objective lens and object in a confocal microscope. A parallel beam with a circular cross-section (this cross-section is not shown in the illustration) passes through the lens. The lens focuses the light in its focal plane.

Between lens and focal plane the light rays form a convergent circular cone. If refractive index variations in the object are negligible, the light distribution below the plane of focus forms a cone as well, due to symmetry. Assuming a non- or weakly absorbing specimen, the energy of the light in the circular cross-sections of the cone remains constant¹.

The fluorescent bead (1), in the focus, would therefore be excited significantly more than the bead (2) outside the focal plane. Also shown is the light distribution in the intermediate image plane.

The image of the in-focus bead (1) is sharp, i.e. its emanating fluorescence light is concentrated on an area as small as possible and positioned exactly on the detection pinhole. Conversely, the image of the out-of-focus bead (2) is blurred and its fluorescence light is distributed over a large area.

While only a tiny proportion of the light emitted by the out-of-focus bead contributes to the detection signal of the confocal microscope—and therefore hardly affects the image quality, with respect to overall phototoxicity of the full confocal system—it would be better to prevent the excitation of the out-of-focus bead in the first place.

The scheme in Figure 4.1 b) demonstrates how the light cone would have to be manipulated in order to exclude the out-of-focus bead (4). The expected fluorescence image in the intermediate image plane then contains only information from the in-focus bead (3).

Viewed from the in-focus bead (3) the change in illumination corresponds to a restriction of the light angles. Such control can be exerted well through a mask in the other focal plane of the objective lens (also denoted back focal plane or pupil plane).

¹The ray-model is valid in large parts of Figure 4.1 a), but not everywhere. The Law of Malus–Lupin states that rays and wavefronts are equivalent as long as rays do not intersect (caustic), or (FIXME formulas?) a strong intensity gradient occurs. Thus the ray-model is valid almost everywhere in the cone, except for a region with a distance of a few wavelengths to the edge, and the focus itself. While the wave-optical treatment of these areas is possible, it is computationally much more expensive than ray tracing. Wave-optical effects either lead to blurring in a length scale of a few wavelengths or intensity fluctuations due to interference. If necessary, we can use heuristics to find an upper bound for the local intensity from ray tracing results. For this reason we exclusively employ the ray-model in this work.

4. The concept of spatio-angular microscopy

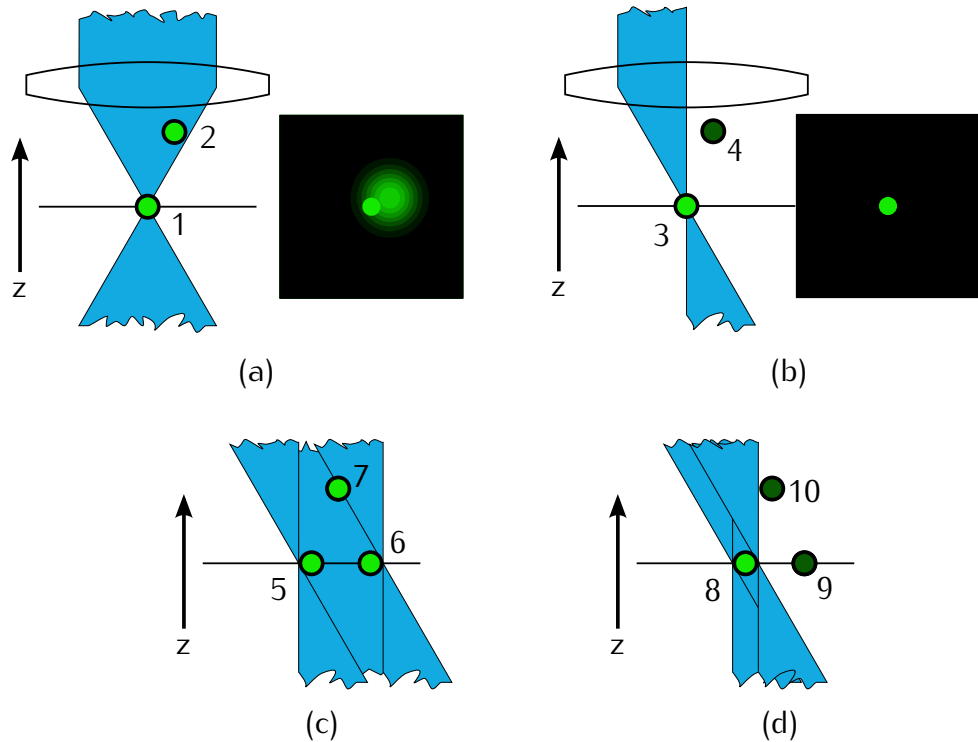


Figure 4.1.: (a) Two fluorescent beads are illuminated by all angles that the objective can deliver. The sharp image of the in-focus bead is deteriorated by blurry fluorescence of the out-of-focus bead (2). (b) Angular control allows selective illumination of the in-focus bead (3), and results in a better image on the camera. (c) Angular control, however, is insufficient, when an extended in-focus area is illuminated. (d) Then, simultaneous spatial and angular control allows sequential excitation of the in-focus beads, while excluding the out-of-focus bead (10).

Thus it is useful and possible to equip a confocal microscope with angular control. However, in our project we set out to build a wide field microscope in order to benefit from the speed and quantum efficiency of modern cameras.

I now turn to the task of bringing angular control to the wide field microscope. Figure 4.1 c) shows a configuration of the specimen with two in-focus beads (5) and (6), and one out-of-focus bead (7). The angular illumination control is ineffective for this arrangement of beads. If both in-focus beads, (5) and (6), are exposed simultaneously, i.e. an extended light source illuminates the entire field, then the out-of-focus bead (7) is always excited.

Only by separate illumination of the in-focus beads (8) and (9), as shown in Figure 4.1 d), angular control regains its function. For this reason a wide field system with angular control, using a mask in the pupil, requires an additional mask conjugate to the field. Therefore, we call our method spatio-angular microscopy.

4. The concept of spatio-angular microscopy

"Spatial" refers to the illumination control in the field and "angular" refers to the control in the pupil plane.

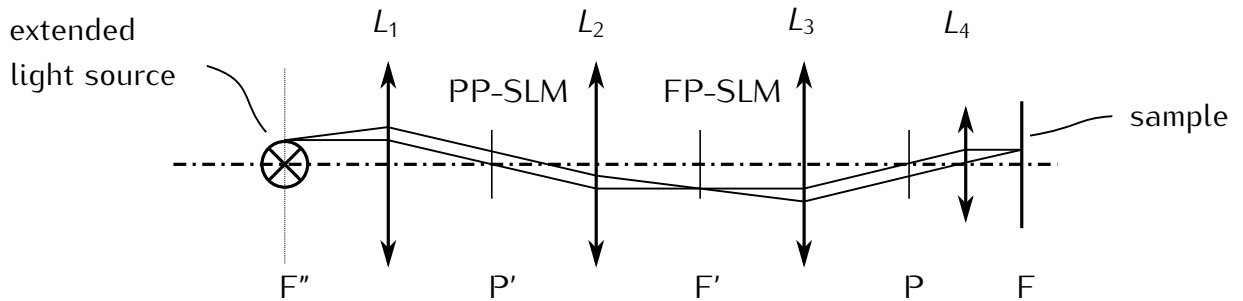


Figure 4.2.: Simplified schematic of the illumination system in our spatio-angular microscope. A homogeneous extended light source delivers light from the left. It is imaged by lenses L_1 and L_2 into the intermediate image F' . Then the tubelens L_3 and the objective L_4 form an image of F' in the sample plane F . We use two spatial light modulators (SLM) to control the spatial and angular light distribution in the specimen—the focal plane SLM in F' , and the pupil plane SLM in P' .

Figure 4.2 shows the optical path through our prototype in a simplified form. From the left side, an extended light source illuminates the system. A sequence of telecentric lenses L_1 , L_2 , L_3 and the objective lens L_4 image the light source from F'' into the front focal plane (indicated by F , for field). The etendue (see page 27 for its definition) of the light source must be large enough to simultaneously fill both, the pupil P as well as the field F .

In each of the two planes P' and F' we place a spatial light modulator (SLM) that allows to control the intensity of the transmitted light.

Looking at the scheme in Figure 4.2, one might argue that we could save a lens, if we placed the pupil plane SLM into P instead of P' . There are three reasons why this is neither possible, nor beneficial: First, the pupil of modern high-performance objective lenses is typically not accessible. Second, the detection path for fluorescent light should contain as few optical components as possible and we can definitely not afford it to be blocked by a SLM. Third, the two masks induce non-linear, and therefore difficult to predict, filtering of spatial frequencies. An analysis requires consideration of partial spatial coherence, but it should be clear (FIXME) that only the downstream² SLM will always deliver a good image, mostly independent of the state of the SLM upstream.

Considering the fact that the image of the focal plane SLM is most important to us, we decided to place it downstream of the pupil plane SLM. The focal plane

²Downstream regarding the propagation direction of the excitation light.

4. The concept of spatio-angular microscopy

SLM may disturb the image of the pupil plane SLM in P, but we can always produce very fine, high-contrast structures in the sample F.

The ability to achieve high resolution in the field is the main difference between our approach and Levoys light field microscope. In the light field microscope, the density of the microlenses noticeably limits the resolution. As opposed to our system, the light field microscope allows to control the angle of incidence in all field positions independently. But, additionally to the reduced focal plane resolution, this requires a single high-resolution SLM with a comparatively low refresh rate. We use two small SLMs, which can each achieve 1 kHz frame rate and enable interesting experiments, e.g. optogenetic control of neuron activities.

Furthermore, structured illumination with high resolution patterns allows us to circumvent the missing cone problem of the widefield microscope. Later I will show that depth discrimination improves with higher resolution patterns (FIXME ref).

4.2. An imaging protocol with spatio-angular illumination control

4.2.1. Description of an exemplary biological specimen

I now refer to the *C. elegans* test sample for phototoxicity that I introduced in section 1.1. So far I did not reach the point of being able to image the development of a real embryo. Key problems are the low light throughput of the illumination system and the length of time necessary to update images on the focal plane display. Nevertheless, I always kept this example in mind while I was developing the control software for our microscope.

During the first few hours, the embryo develops confined within the constant volume of its egg, which has an ellipsoidal shape, extends 40 to 60 microns and can be readily observed using a 63 \times objective lens. Cell divisions occur every few minutes. During development the nuclei get smaller and more dense. In order to track the fate of all individual cells it is sufficient, to capture one stack per minute with 41 layers and a z-step of 1 micron.

4.2.2. Preparation of living embryo samples

For an experiment a hermaphrodite worm is cut and the embryos are placed on an agarose pad, so that they stay immobile during imaging. This procedure is

4. The concept of spatio-angular microscopy

explained³ in Hope (1999). Of these embryos, the experimenter chooses a young specimen, that has not yet divided. We avoid to use fluorescence excitation for this step. The undivided embryos can be distinguished using the less phototoxic differential interference contrast (DIC) imaging mode.

4.2.3. Sectioning through structured illumination

To get an estimate of the initial distribution of the fluorophores in the embryo I obtain the very first stack with structured illumination and no angular control. I use this method to avoid the missing cone problem of the widefield microscope. Perhaps for our particular task of finding the position of one nucleus within the egg, widefield images would be just sufficient. However, for our spatio-angular method, knowledge about the fluorophore distribution is very important and therefore we built our microscope such that we can obtain optical sections.

We compared conventional structured illumination using max–min (FIXME) reconstruction with laser and LED illumination. Although LED illumination resulted in excellent optical sections, the reconstruction of laser illuminated images contained artifacts.

Therefore, we decided to implement HiLo (see Appendix FIXME). With this algorithm, we obtain artifact-free optical sections, regardless of the illumination source. As another advantage the HiLo method increases acquisition speed, because only two raw images per slice are necessary.

4.2.4. Computer model for the integration of a priori knowledge about the biological events

Given an initial measurement of the fluorophore distribution of the embryo, I employ a computational algorithm to find good illumination conditions for subsequent stack acquisitions. An important requirement is that the computer can estimate, which areas of the sample should be protected from illumination.

For our test system, the *C. elegans* embryo, it is a promising approach to represent its three-dimensional fluorophore distribution by a simple model: Spheres encompassing the nuclei, indicate regions with fluorophores. When in focus, the spheres are the source of useful, informative fluorescence signal, but should be protected against exposure when out of focus.

³Note that Murray et al. (2006) describes an improvement of this protocol that prevents squeezing the embryos too much.

4. The concept of spatio-angular microscopy

As I mentioned earlier, there are also unused histones with fluorophores outside of the nuclei. The images reveal that they occur in the cytoplasm at a much lower concentration than in the nuclei. Fluorophores in the cytoplasm have a smaller phototoxic effect, because any radicals they produce are much less likely to reach the DNA and therefore inflict substantially less damage. In the following my goal is to protect only out-of-focus nuclei from exposure. The regions in between are used to bring the light in.

During observation, the nuclei, i.e. the centers of the spheres, move slowly within the embryo. For small periods of time we can describe this movement using a vector field of growth velocities.

A cell division announces itself by a change of the fluorophore distribution of the nucleus due to chromatin condensation and spindle formation. Therefore, whenever the computer detects such changes in the images, in one of the following time steps an additional sphere should be introduced to account for the new daughter cell.

So far I have implemented a simple algorithm, to convert a time series of image volumes from a confocal microscope into a sphere model (Santella et al. 2010). One of our project partners (Jean-Yves Tinevez, <http://fiji.sc/wiki/index.php/TrackMate>) developed a more sophisticated plug-in for ImageJ, that provides the lineage tree and snapshots of the developing cells (see Figure 4.3). Before our microscope can

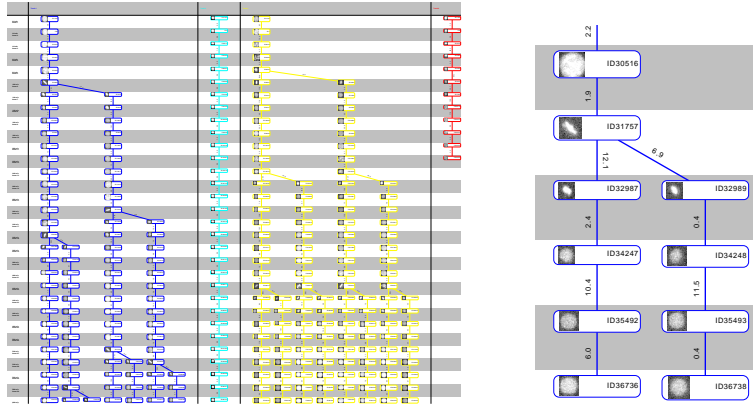


Figure 4.3.: A detail of a lineage tree visualized in TrackScheme. An image of each nucleus is shown in each time step. Note the elongated structure of the nucleus before the cell division event.

be used for our biological problem, the computer model has to be extended so that it reliably tracks the movement of nuclei. Overlooking any nucleus would prevent this nucleus from being imaged in later acquisitions and would be a setback for the experiment. Estimating the vector field of growth velocities helps to track

4. The concept of spatio-angular microscopy

nuclei more robustly and allows to predict their positions for the next exposure.

Currently we have not implemented programs that would fulfill the requirements for imaging a developing embryo. However, in the following text I assume that the described position predictions were available and I discuss how I determine masks for the focal plane and pupil plane SLM.

Murray et al. (2006)

TODO FIXME Bernhard Kauslers work is nice <http://archiv.ub.uni-heidelberg.de/volltexte/2012/12437/>
Live-cell microscopy image analysis for the study of zebrafish embryogenesis
http://hci.iwr.uni-heidelberg.de/publications/mip/techrep/kausler_12_discr.pdf
A Discrete Chain Graph Model for 3d+t Cell Tracking with High Mis detection Robustness

(FIXME read this)

4.2.5. Illumination optimization by means of raytracing

I now discuss a method to find both SLM masks for image acquisitions with minimal phototoxicity. First I define a mask for the focal plane SLM:

From the predicted arrangement of spheres we select in-focus nuclei by intersecting the model with a planar surface. I then define focal plane SLM masks to selectively illuminate each of the in-focus nuclei, by drawing a bright disk in the appropriate position.

Based on such a mask, we can determine which angles can illuminate the in-focus target nucleus, without exposing out-of-focus nuclei.

As I already explained at the beginning of this chapter on page 53, ray-optical theory suffices to describe the light distribution within the sample.

I connect the periphery of an out-of-focus nucleus with a point inside the in-focus target. This defines a circular cone of rays, that are propagated through the objective lens. Their intersection with the pupil plane results in a figure that still very much resembles a circle—I found that already seven rays lead to good representation of its perimeter. An algorithm computes these figures for every out-of-focus nucleus and for a few in-focus targets points within the bright areas of the focal plane pattern. In this manner I construct the desired mask for the pupil plane SLM.

In order to trace the rays into the pupil, I need the design parameters of the objective lens (vertex position, curvature and material for all surfaces). Unfortunately, these rarely are publicly available for high-performance objective lenses. Nevertheless, in chapter (FIXME) I use a simpler model of the objective lens, that

4. The concept of spatio-angular microscopy

requires only three parameters: focal length, refractive index of the immersion medium and numerical aperture. These are always known.

Additionally, I have adapted the model for non-index-matched embedding of the specimen. This problem occurs when the embryo is illuminated with an oil immersion objective, using HILO (FIXME ref). It should be noted, however, that good image quality of the embryo can only be achieved with an objective lens that has the same immersion index as the embryo. Otherwise data from 20 microns within the sample will be severely deteriorated by spherical aberrations.

5. Description of our prototype for spatio-angular illumination

In the preceding chapter I showed the underlying concept of our spatio-angular microscope. Here I discuss additional details that are important for the practical implementation.

I explain the beam path, electronic synchronization of the displays with other components and an algorithm to transform the coordinate system of the camera pixels into the coordinate system of the focal plane SLM.

The pupil plane SLM was specifically developed for our project by our partner Fraunhofer IPMS (Dresden, DE).

5.1. Description of the optical components

So far I have only shown the beam path for transmissive displays (in Figure 4.2). Such SLM only have a very low transmission in practice. Therefore we use reflective displays in our prototype.

In Figure 5.1 I adjusted the beam path accordingly. This schematic also depicts the optics we use to adapt light from the laser to fill the etendue of our system. The light source enters the system from the bottom left. The optic components are color corrected and have anti-reflex coating for wavelengths in the range from 400 nm to 700 nm.

The system successively illuminates the pupil plane SLM — a grayscale micromirror array developed by our project partner Fraunhofer IPMS Dresden — and the focal plane SLM, a commercial binary liquid crystal on silicon display.

I gathered some of the following details from the documents that were created during the development of our prototype and are classified as confidential. I have summarized the key decisions here and the relevant project partners have agreed to the publication.

5. Description of our prototype for spatio-angular illumination

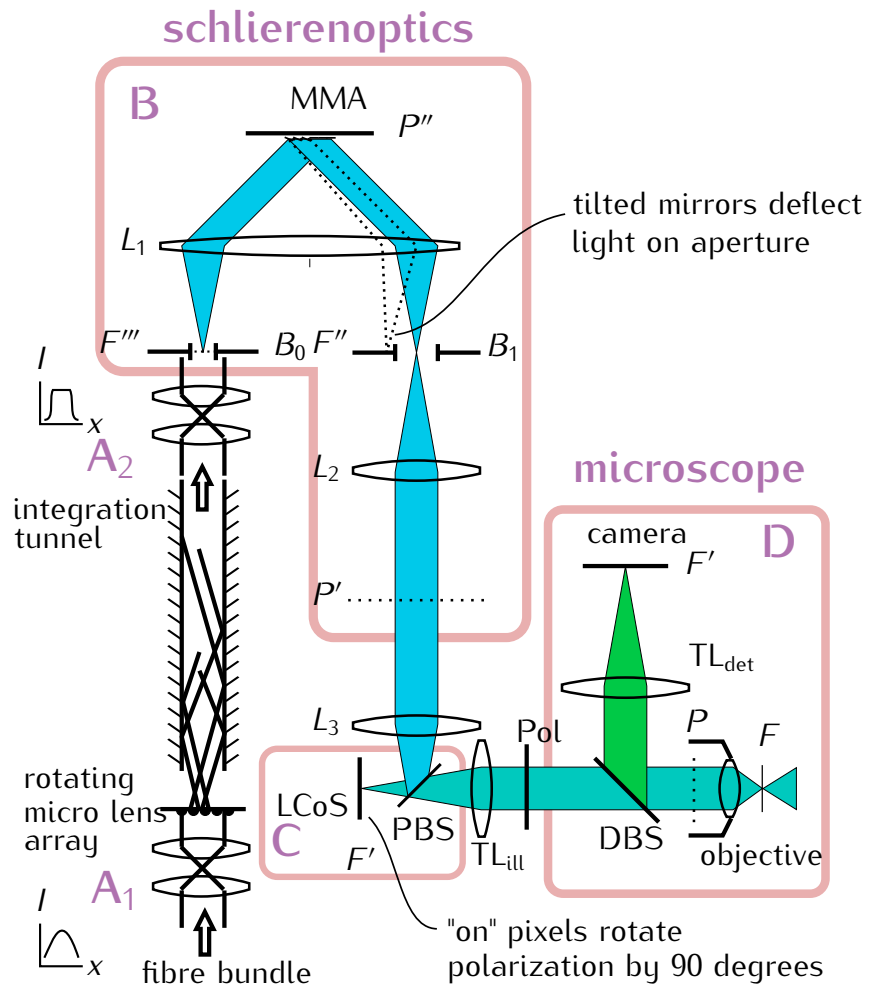


Figure 5.1.: Schematic of the light path through our microscope. Laser light enters from the lower left, is scrambled and homogenized to illuminate the pupil plane SLM in P'' and the focal plane SLM in F' . F is the field plane in the sample and its primed versions are conjugated planes. P is the pupil of the objective. Field mask B_0 and Fourier stop B_1 are adjustable circular apertures. PBS is a polarizing beam splitter. DBS is a dichroic beam splitter. The red boxes delineate subsystems of the illumination system: **A₁** and **A₂**: light scrambling and homogenization, **B**: Fourier-optical filter to provide intensity modulating pupil plane SLM. **C**: Polarization based intensity modulator as focal plane SLM. **D**: Wide-field fluorescence microscope with detection path.

5. Description of our prototype for spatio-angular illumination

5.1.1. Ensuring homogeneous illumination

A quantitative evaluation of our experiments (FIXME ref sec:results) with different illumination patterns is simplified when both pupil plane SLM and focal plane SLM are uniformly illuminated.

We use either a laser¹ or a light emitting diode (LED) as the light source in our experiments. Below we discuss optical measures that attain homogeneity of the illumination of both displays.

The LED² we use has a large active area. Due to etendue mismatch a relatively large amount of its produced light will never reach the sample. But it is easy to achieve a homogeneous illumination. Moreover, the LED can be quickly switched on and off electronically.

Unlike an LED, a laser delivers light of considerably higher spectral radiance ($\text{W}/(\text{sr m}^2\text{m})$). Thus it is in principle possible to use the laser as a highly efficient light source for our system. Unfortunately, the high spectral and spatial coherence of a laser often lead to high-contrast fluctuations of the irradiance and we have to compensate for this by time averaging.

When using the Laser, we send its parallel Gaussian beam into a bundle³ of randomly distributed fibers. This randomizes the light distribution at the bundle output and also broadens the illumination angles.

A relay system (A_1) images the circular output of the fiber bundle onto the entrance of a light pipe. This relay system contains a rotating microlens array⁴. It is driven by a motor with the axis of rotation being displaced from the optical axis. This time-varying element allows to reduce speckle.

Both, the fiber bundle and microlens array, increase the etendue of the laser illumination to the optimum value, which is given by one of our SLM as discussed on page 68.

The light pipe is a hollow mirror-integrator tunnel with quadratic cross-section and depicted in Figure 5.2. The mixing effect of the tunnel can be understood by considering the irradiance in the plane of the tunnel output as it would occur without tunnel.

Drawing the outline of the square cross-section into this irradiance map selects the light that directly reaches this plane. Surrounding this outline with four

¹Lasever LSR473H, diode-pumped solid state laser, output power 600mW, $\lambda = 473 \text{ nm}$

²Huey Jann HPB8-48KBD, wavelength $(463 \pm 1) \text{ nm}$, brightness 35lm, view angle 120°

³Fiber bundle with circular cross-section (Loptek, Berlin, DE), 1.1 mm diameter and 2 m length.

The beam broadening is 3° and increases, when the bundle is bent (Ipp et al. 2009a).

⁴Array of cross-oriented cylindrical lenses on both sides with a pitch of 0.5 mm resulting in an effective focal length of 6.9 mm (LIMO, Dortmund, DE).

5. Description of our prototype for spatio-angular illumination

identical copies that touch its edges selects the light that will reach the output plane after one reflection. The irradiance maps from neighbouring squares are mirrored and added to the direct illumination. Depending on the numerical aperture of the input light, more reflections may occur — resulting in the addition of irradiance from next-nearest-neighbours and so forth.

This improves the uniformity of the light distribution in the output plane without altering the numerical aperture of the light. The more subregions are superimposed, the better will be the uniformity. Assuming N subregions were overlaid and their contributions were statistically independent, then according to the central limit theorem the standard deviation of the irradiance is proportional to $1/\sqrt{N}$ (Koshel 2012).

However, we also align the source distribution to be rotationally symmetric about the optical axis and obtain an even more uniform output than what would follow from this prediction because positive and negative slopes from different subregions compensate in the superposition (also Koshel (2012)).

In our system the side length of the cross-section of the tunnel is 2.5 mm and its length of 250 mm ensures enough reflections for homogeneous illumination. A relay system magnifies the tunnel output to $4\text{ mm} \times 4\text{ mm}$ in the plane F'' .

We thought about using the output of the tunnel directly, without the additional relais system, but then the length of the tunnel would have been prohibitively long.

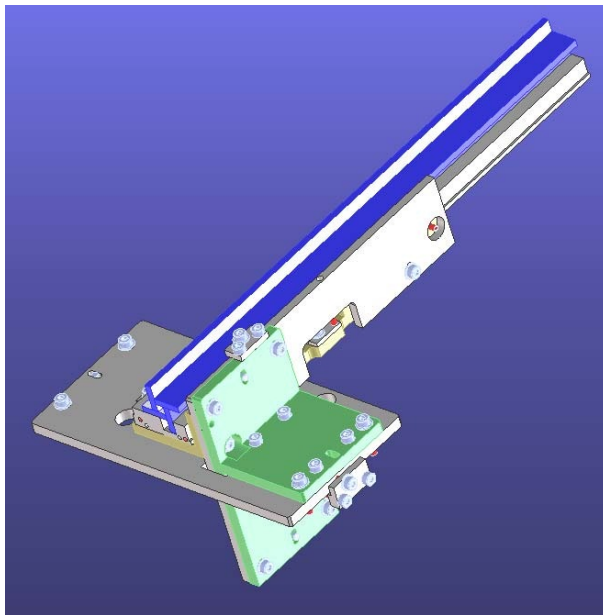


Figure 5.2.: Hollow mirror-integrator tunnel with a quadratic cross section of 2.5 mm side length and 250 mm length.

5. Description of our prototype for spatio-angular illumination

Regarding the two relay systems the optical designer at In-Vision commented (Ipp et al. 2009b) that these have not been optimized for perfect imaging but for the transport of the homogeneous light distribution. The system A_1 at the tunnel entrance has to transfer the illumination from the round fiber end to the square tunnel entrance. The engineer designed a good quality system with only two lenses (and the microlens array). At the other end (A_2 in Figure 5.1) five elements carry the light from the tunnel exit into the field mask B_0 in F'' .

During the planning phase we also considered a homogenization design based on a fly's eye condensor (two consecutive microlens arrays). According to simulations performed by In-Vision, this, however, would have been more difficult to adjust than the tunnel. In particular the system would have been more dependent on illumination wavelength.

In summary the following points are important in order to achieve homogeneous illumination of focal and pupil plane with the tunnel:

- The image of the end of the bundle should properly cover the tunnel entrance. Especially the corners of the tunnel should not be darker than the center. Inhomogeneous illumination at the tunnel entrance leads to inhomogeneous illumination of the pupil plane SLM.
- The end of the fibre bundle must be adjusted in four axes (centering and angle).
- The focal length of the microlenses should be chosen shorter than predicted by pure etendue calculation. In order to compensate inevitably occurring microchipping on the edges of the cemented glass mirrors.

5.1.2. Fourier optical filter for contrast generation on pupil plane SLM

The micromirror array, which we use as a pupil plane SLM consists of torsion mirrors that modulate the phase of the light (see Figure 5.3 for images of the device). In order to modulate the intensity we use the Fourier optical filter denoted as 'schlierenoptics' in Figure 5.1 B.

The device itself is documented in more detail the following references: design of the actuators (Schmidt et al. 2010), gray value images and contrast measurement (Berndt et al. 2010) and per-pixel calibration of the deflection angle using a white light interferometer (Berndt et al. 2011; Berndt 2007).

The lens L1 has two purposes: First, it images the field mask B_0 into the Fourier stop B_1 . Second, the plane P'' with the phase SLM is imaged to infinity.

5. Description of our prototype for spatio-angular illumination

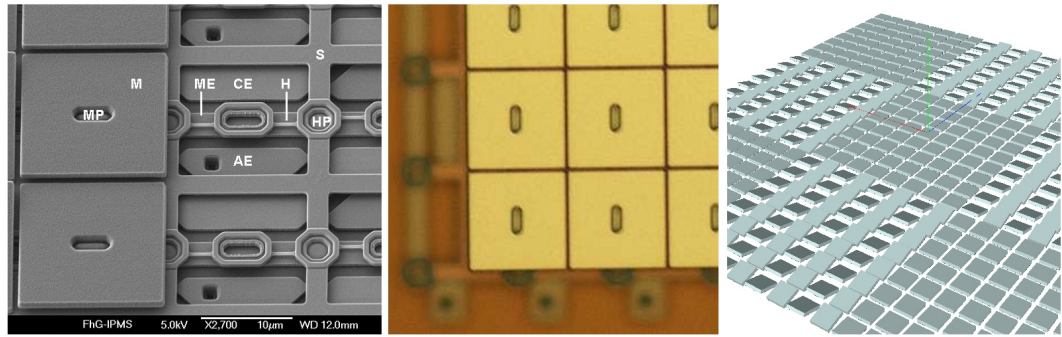


Figure 5.3.: **left:** Scanning electron microscope image of the micro-mirror array (MMA). The pixel pitch of the device is 0.016 mm. The hinges for the tilt movement and the electrodes are clearly visible. **middle:** Optical reflective microscope image of the MMA. **right:** exaggerated rendering of how a 8x8 checker board pattern would be displayed on the device. Electron and optical micrograph by Fraunhofer IPMS Dresden (Germany)

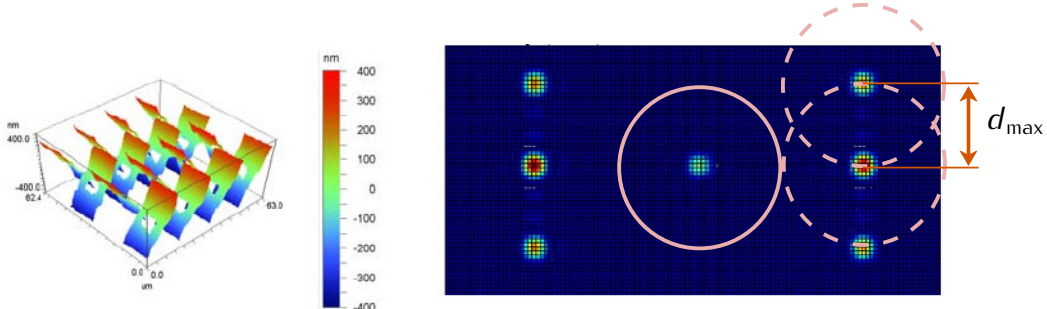


Figure 5.4.: **left:** Measurement of the deflection of micro-mirrors using a white-light interferometer (provided by Fraunhofer IPMS Dresden (Germany)). **right:** Simulation of the Fraunhofer diffraction pattern of the micro-mirror array for coherent, monochromatic light (kindly provided by Joel Seligson). The circles with radius d_{\max} indicate the maximum size of the field mask B0 where the diffraction orders do not overlap. This limits the etendue of our illumination system.

With undeflected micromirrors, the SLM has no significant effect and works like a plane mirror. Both planes F'' and P' are then homogeneously illuminated.

If the left half of the micromirrors are tilted, then they direct the light along the dashed line in Figure 5.1. This light is absorbed by the field stop B1 and therefore missing in P' , i.e. the right side in P' is dark. The total radiant flux (W) through the beam stop in F'' decreases while the transmitted irradiance (W/m^2) remains homogeneous. In the real system, the lens L1 consists of four glass elements.

The phase distribution $\Phi(x)$ in MMA plane corresponds to the profile in Fig-

5. Description of our prototype for spatio-angular illumination

ure 5.4 left:

$$\Phi(\mathbf{x}) = \sum_{\mathbf{p}} \left[\underbrace{\left(\exp(i\mathbf{k}(p_x, p_y)\mathbf{x}) \cdot \text{rect}(x, y) \right)}_{\Phi_p} \otimes \delta(x - p_x \Delta x, y - p_y \Delta y) \right] \quad (5.1) \text{?eq:mmma-con}$$

where $\mathbf{x} = (x, y)$ is a position in the MMA plane, the rectangular function rect delimits an individual micro-mirror with its deflection encoded in $\mathbf{k} = (k_x, k_y)^T$. The index vector $\mathbf{p} = (p_x, p_y)^T$ indicates the mirror position.

The diffraction pattern of an individual mirror is a sinc–function which is shifted according to the mirror deflection and a phase gradient which depends on the mirror position \mathbf{p} :

$$\tilde{\Phi}_p(\mathbf{k}) = \mathcal{F}(\Phi_p(\mathbf{x})) = \text{sinc}(k_x - k(p_x, p_y)) \cdot \exp(i\mathbf{k}(p_x \Delta x, p_y \Delta y)) \quad (5.2)$$

Adjacent rows of mirrors tilt in opposite directions ($\pm x$). Therefore, we can specify the term $\Phi_p(\mathbf{x})$ in equation 5.1 more precisely and obtain two expressions:

$$\Phi_p^{(1)}(x, y) = e^{+ik_0x} \text{rect}(x) \otimes \sum_p \delta(x - p \Delta x) \quad (5.3)$$

$$\Phi_p^{(2)}(x, y) = e^{-ik_0x} \text{rect}(x) \otimes \sum_p \delta(x - p \Delta x) \quad (5.4)$$

A good analytical description of the surface of the MMA is:

$$\begin{aligned} \Phi(\mathbf{x}) &= \Phi_p^{(1)}(x, y) \left(\text{rect}(y) \otimes \sum (\text{every second row}) \right) \\ &\quad + \Phi_p^{(2)}(x, y) \left(\text{rect}(y) \otimes \sum (\text{every second row, shifted by one}) \right) \end{aligned} \quad (5.5)$$

Figure 5.4 right shows a numerically calculated diffraction pattern of this structure for a monochromatic plane wave. Suppose the Fourier stop B1 blocks light outside of the circle with the solid line. Then the transmitted zero-order irradiance is proportional to the sinc^2 of the deflection angle. This applies more or less even if not all mirrors of the array are deflected. Therefore, we can modulate the irradiance in the plane P' using this optical system albeit the transfer function is non-linear.

An accurate prediction of the irradiance in P' is even more difficult to describe when the field mask B0 is opened and the extended source produces illumination that is spatially partially coherent (Mehta 2010).

But one thing is clear: The contrast can only achieve good results as long

5. Description of our prototype for spatio-angular illumination

as higher diffraction (dashed circles in Figure 5.4 right) orders can not pass the Fourier stop B1. This limits the size of the field mask B0 to the diameter d_{\max} , assuming that no high frequency pattern is displayed on the MMA.

The smallest distance between the orders in Figure 5.4 right corresponds to a structure size Λ of two mirror pitches: $\Lambda = 32 \mu\text{m}$. Therefore the diffraction angle θ is:

$$\sin \theta = \lambda / \Lambda \quad (5.6)$$

Utilizing this, we can express the maximum radius:

$$d_{\max} = f_{L1} \tan \theta \approx \frac{f \lambda}{\Lambda} \quad (5.7)$$

Here, f_{L1} is the focal length of lens L1. With the F-number $\# = f_{L1}/(2d_{\max})$ we can find the maximum etendue of the Fourier optical system:

$$\mathcal{E} = \frac{\pi A}{4\#^2} = \frac{\pi A \lambda^2}{\Lambda^2}, \quad (5.8)$$

with the area $A = (4 \text{ mm})^2$ of the micro-mirror array.

For our system the maximal etendue is between $0.0079 \text{ mm}^2/\text{sr}$ and $0.024 \text{ mm}^2/\text{sr}$, depending on the wavelength. This is much smaller than the etendue of a typical microscope objective ($0.27 \text{ mm}^2/\text{sr}$, see section 1.3.3) and corresponds to a field diameter D_{field} in the specimen between $70 \mu\text{m}$ for a wavelength λ of 400 nm and $125 \mu\text{m}$ for 700 nm , with

$$D_{\text{field}} = \frac{2}{\text{NA}} \sqrt{\frac{\mathcal{E}}{\pi}}, \quad (5.9)$$

where NA is the numerical aperture.

5.1.3. Relay optics between pupil plane and focal plane SLM

The lenses L2 and L3 form a double-telecentric relay system with magnification 2 and image F'' onto the focal plane SLM in F' . At the same time these lenses make sure that the pupil plane SLM is imaged to infinity.

The relay system ensures that the pixels of the focal plane SLM are at the resolution limit, while the pupil plane SLM fills the pupil.

In addition, the relay system enables a simpler mechanical realization and good contrast. It would already be difficult to accommodate the focal plane SLM

5. Description of our prototype for spatio-angular illumination

and polarization beam splitter in F'' — including an adjustable aperture would probably not be feasible at all.

5.1.4. Contrast generation on focal plane SLM using polarization

Why fLCoS and not DMD?

The SLM we use to control the focal plane illumination is a ferroelectric liquid crystal on silicon device (fLCoS, ForthDD WXGA R3, UK). Depending on if a pixel is off or on, the returning light either retains the polarization of the input light or rotates it by 90 degrees (Martínez-García et al. 2009). From this, a polarization beam splitter generates a binary intensity contrast (see Figure 5.1 C).

We have not opted for a digital micro-mirror device (DMD), because those mirrors have sharp edges and loose significant amounts of light into higher orders that can not contribute to the image in the specimen. The pixels borders of a fLCoS device are defined by electric fields and are therefore more blurred. At least in this sense, an fLCoS based device should be more efficient than a DMD.

We use a wire-grid polarization beam splitter (Moxtek PBF02C, Orem, UT, US) because they ensure a high enough optical quality, good contrast and the plate causes less back reflections than a beam splitter cube.

The s-polarized component of the incoming light is reflected towards the SLM. Active pixels of the SLM rotate the polarization of light by 90 degrees and then passes through the beam splitter as p-polarization in the direction of the microscope. There is a supplementary cleanup analyzer in the beam path.

It would also be conceivable to arrange SLM and beam splitter differently, so that the light coming from the SLM is *reflected* towards microscope. In this case, however, unwanted bending of the beam splitter's surface will deteriorate the image quality of the focal plane SLM. Therefore, we use the beam splitter in transmission.

The beam splitter plate makes the overall optics slightly asymmetric and thus induces mainly astigmatism and lateral color (Ipp et al. 2009b). The plate is thin enough (thickness 0.7 mm), so that the design remains diffraction limited.

5.1.5. Variable telescope as tube lens

Microscope objectives come with various pupil diameters. The last lens TL_{ill} in our illumination system has been designed as a variable zoom objective (by In-Vision, Guntramsdorf, Austria), that maps the pupil plane SLM from P'' with variable magnification to P .

5. Description of our prototype for spatio-angular illumination

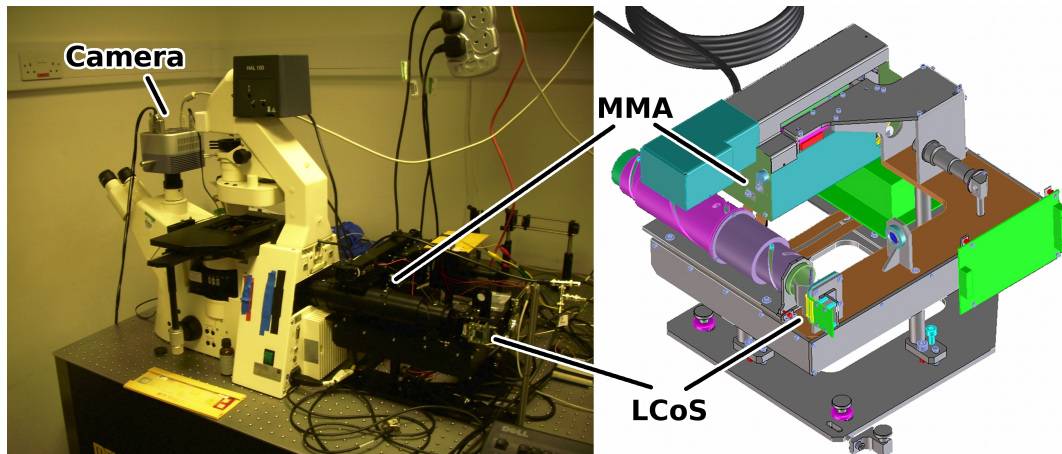


Figure 5.5.: The wide field epi-fluorescence microscope with attached illumination head. The positions of the two spatial light modulators (pupil plane SLM: micromirror array (MMA) and focal plane SLM: liquid crystal on silicon display (LCoS)) are indicated. Drawing by Josef Wenisch (In-Vision, Austria).

Unlike conventional zoom telescopes we use three movable lens groups to guarantee that the image of the pupil plane SLM remains stationary while the focal plane SLM is always imaged into infinity during magnification changes.

5.2. Electronic control of the component

local pattern storage

Both spatial light modulators can run at most with 50% duty cycle. Therefore it is necessary to synchronize the displays. Their controllers allow to upload several hundred frames of image data at the beginning of an experiment and keep them in local storage. Images can then be selected by relatively fast function calls over USB (focal plane SLM, fLCoS) or Ethernet (pupil plane SLM, MMA), see Figure 5.6 for a plan of the interconnections.

camera is master

The camera (Clara, Andor PLC, Belfast, Northern Ireland) as the slowest device is chosen as the master. It provides two TTL outputs. The output "fire" is high while the camera is integrating. The output "shutter" is programmed to go high 1 ms before "fire".

FIXME translate

This allows an Arduino microcontroller to initiate a time-delayed trigger for both SLM, so that they show their patterns exactly while the camera is integrating. I determined the necessary delays using a photodiode and an oscilloscope in order to measure when a dark image is established on each device. The delay is

5. Description of our prototype for spatio-angular illumination

$840\mu\text{s}$ for pupil plane and $396\mu\text{s}$ for focal plane SLM. The Arduino microcontroller activates a laser by an acousto-optic modulator (AOM) so that the system is only illuminated when the camera is integrating and both SLM are showing a defined pattern.

The USB LCoS controller for the focal plane SLM can display its images only for certain discrete times (20 ms , 10 ms , 5 ms , $200\mu\text{s}$). This is because it needs to be programmed with sequences which are supplied by the manufacturer and it is not straight forward to change them via USB interface. Therefore we always work with a fixed LCoS display time of 20 ms .

This disadvantage of the LCoS controller is quite inconvenient as the only way to acquire images from dim specimen is to accumulate several camera readouts. The pupil plane SLM and camera would allow a variable integration time. In particular a Texas Instruments DMD would support variable integration times (?).

The camera acquisitions are stopped by the control software, whenever the XYZ-stage is moved.

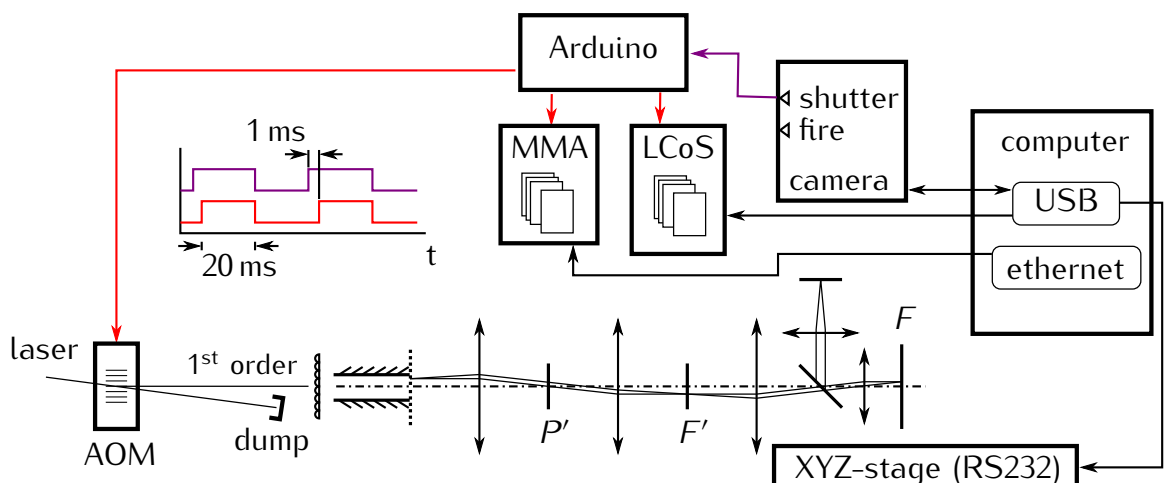


Figure 5.6.: The camera signals the Arduino microcontroller 1 ms before its integration starts. The microcontroller then starts the two SLM so that they have enough time for initialization and later enables the laser.

5.3. Mapping between pixels of the focal plane SLM and camera pixels

FIXME translate

Eine Grundvoraussetzung dafuer, dass die mit dem Raytracer ermittelten SLM

5. Description of our prototype for spatio-angular illumination

Muster das Sample wie geplant bestrahlen ist, dass die Abbildung (mapping) zwischen Pixeln des focal plane SLM und der Kamera bekannt ist. Um diese zu messen, verwende ich als Sample eine fluoreszente Ebene, schalte einzelne Pixel des focal plane SLM ein und nehme Kamerabilder auf.

Die fluoreszente Ebene befindet sich direkt auf der Unterseite des Coverslips. Die Abbildung ist daher nahezu ideal mit keiner (oder vernachlaessigbar geringer) Distortion.

5.3.1. The rigid coordinate transform

- da eine ebene abgebildet wird kann kann minimal vier freiheitsgrade
- prinzipbedingt
- rotation veraendert sich am meisten
- skalierung bleibt gleich, und optische achse bleibt gleich
- das vereinfacht es ungemein verglichen mit einer affinen transformation mit 4 unabhaengigen eintraegen in der matrix (zusaetlich scherung und anisotrope skalierung) also insgesamt 6 freien parametern

Whenever the camera is moved or the variable tubelens is changed, we have to recalibrate the system with a fluorescent plane sample on which we project single spots with known positions on the focal plane SLM. Here I describe a robust approach to find a rigid transform between focal plane SLM and camera coordinates.

In order to relate coordinates on the LCoS display with pixel positions on the camera, I found it suffices to use a rigid transform. The rigid transform between display and camera is defined as:

$$\mathbf{r}^d = s\mathbf{R}_\phi \mathbf{r}^c + \mathbf{t} \quad (5.10)$$

$$\mathbf{R}_\phi = \begin{pmatrix} \cos \phi & q \sin \phi \\ -\sin \phi & q \cos \phi \end{pmatrix} \quad (5.11)$$

where $\mathbf{r}^d = (r_x^d, r_y^d)^T$ is a point on the display, $\mathbf{r}^c = (r_x^c, r_y^c)^T$ is a point on the camera, $\mathbf{t} = (t_x, t_y)^T$ is a translation vector and R_ϕ is a rotation matrix (or a rotation matrix with a reflection if $q = -1$). The value of q can be either $+1$ or -1 . The value of q is -1 , if there is a single axis reflection. It is $+1$ if there is no reflection.

One can find the transform parameters scaling s , rotation angle ϕ , translation

5. Description of our prototype for spatio-angular illumination

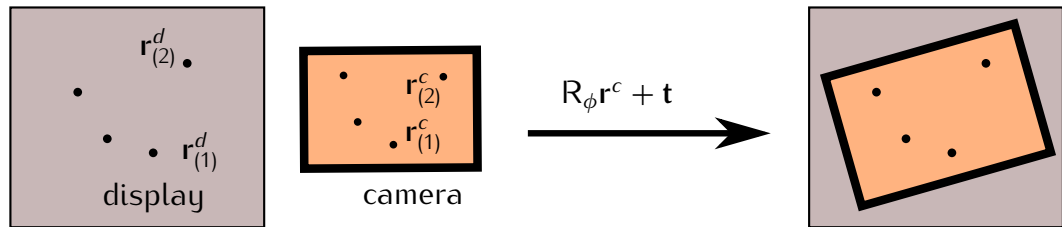


Figure 5.7.: Given $n \geq 4$ camera images of a display showing one point. It is possible to calculate the parameters of the rigid transform parameters scaling s , rotation angle ϕ , translation vector \mathbf{t} .

vector \mathbf{t} , i.e. four degrees of freedom, by minimizing

$$\mathcal{Q} = \sum_i^n |sR_\phi \mathbf{r}_i^c + \mathbf{t} - \mathbf{r}_i^d|^2 \quad (5.12) \text{ ?eq:rigid-}$$

for all n points on the display \mathbf{r}_i^d and there corresponding camera positions \mathbf{r}_i^c .

5.3.2. Experimental example and image processing

For the calibration a fluorescent plane (see Figure 5.8 left for a uniform wide field image) is imaged with the LCoS display showing spots in the illuminated area. Ideally for this measurement all mirrors on the MMA are undeflected and the apertures B_0 and B_1 completely open (see Figure 5.1). Then the square exit of the integrating tunnel illuminates the biggest possible area on the LCoS.

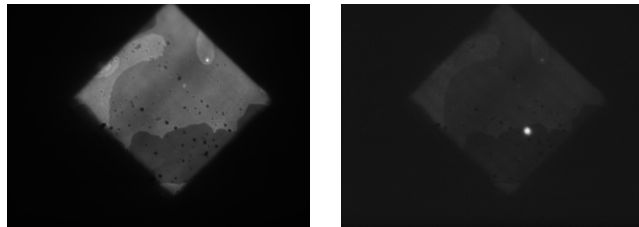


Figure 5.8.: **left:** Uniformly illuminated fluorescent plane (mono and double layer of yellow beads with 110 nm diameter, excited with 473 nm laser in a 63x/1.47 objective). **right:** Image with the the LCoS displaying a disk with 24 pixels diameter (corresponding to $2.4 \mu\text{m}$ in the sample) centred at LCoS position (550, 750).

For the calibration 10×10 images (100 images, each containing one bright spot at a different position) were captured with a disk of 24 pixels diameter at the positions $(400 + 50i, 500 + 50j) \forall i, j \in [0, 99]$. Furthermore, one uniformly illuminated image is used to correct for intensity fluctuations in the fluorescent

5. Description of our prototype for spatio-angular illumination

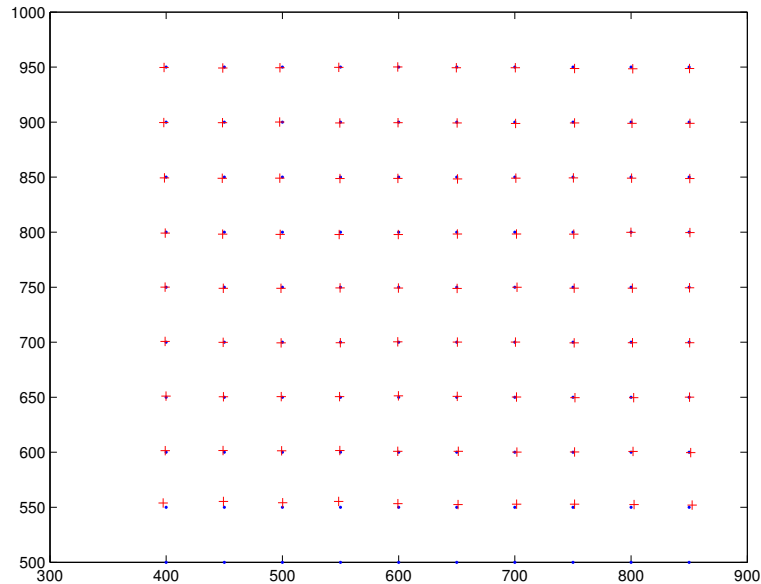


Figure 5.9.: Red “+” signs indicate where the spots that were localized in the camera images end up after a rigid transform. There is sufficient agreement with the original display positions.

plane. The following Matlab/DIPimage code is used to normalize the images and localize the spots. The coordinates are then assembled into the Maxima command that finds the parameters of the rigid transform. Finally the transformed spot positions from the camera images are compared with the original LCoS pixel positions.

5.3.3. Conclusion

The rigid transform and our method to estimate its parameters is a sufficient and robust method, to map the coordinates of our camera into those of the spatial display.

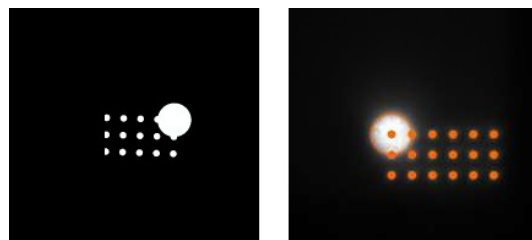


Figure 5.10.: Example of a perfectly fitting rigid transform between LCoS and camera. **left:** Mask that is displayed on the LCoS. **right:** Camera image of fluorescent plane illuminated by mask. The orange lines indicate the borders of the original pattern.

5. Description of our prototype for spatio-angular illumination

The rigid transform can be done directly in OpenGL. Hence, it is trivial to render a properly transformed texture of the camera image which is then shown on the display.

An advantage over other methods, e.g. finding a homology matrix via RANSAC, is that the result is not a transformation matrix but separated parameters for scaling, rotation and translation.

6. Raytracing for spatio-angular microscopy

Imaging with our microscope requires that during the observation of the sample new light patterns are created continuously and as fast as possible. We can not solve this problem by using a commercial software and I therefore decided to implement a simple raytracer.

This chapter documents the basic concepts. Note that some approximations, which are usually used in optical design (paraxial, only non-skew rays) are not applicable here, because rays are to be pursued through diverse fluorophore distributions in samples.

The design parameters of our microscope objectives are not usually known to us. I therefore represent the high-aperture lens using a simplified model (Hwang and Lee 2008). Together with a model of the fluorophore distribution in the sample I can determine which regions of the objectives back focal plane are safe to illuminate and which will excite out-of-focus fluorescence.

Further, I consider the refraction at the coverslip–medium interface for non-index matched media. This enables the calculation of illumination patterns for highly inclined and laminated optical sheet microscopy, as introduced in section 3.1.2.

Note: The formulas in frames are implemented in the computer code that is published on <https://github.com/plops/mma/tree/master/lens>.

6.1. Refraction at planar surface

I begin by describing refraction at a planar surface¹. The wavelength of the light in vacuum defines the length of the wave vector \mathbf{k}_0 . The lengths of the incident and transmitted wave vectors \mathbf{k}_1 and \mathbf{k}_2 are given by the refractive index in their

¹I use the same notation as McClain et al. (1993).

6. Raytracing for spatio-angular microscopy

respective half space:

$$k_0 = 2\pi/\lambda \quad (6.1)$$

$$k_1 = n_1 k_0 \quad (6.2)$$

$$k_2 = n_2 k_0. \quad (6.3)$$

I choose the normal \hat{n} to be directed into the half-space of the incident wave (see Figure 6.1) and define the transversal and normal component of the wave vectors:

$$\mathbf{k}_{1n} = (\mathbf{k}_1 \hat{n}) \hat{n} \quad (6.4)$$

$$\mathbf{k}_{1t} = \mathbf{k}_1 - \mathbf{k}_{1n}. \quad (6.5)$$

The two component vectors are orthogonal and during refraction the transversal component of the wave vector is invariant:

$$k_2^2 = k_{2n}^2 + k_{2t}^2 \quad (6.6)$$

$$\mathbf{k}_{2t} = \mathbf{k}_{1t}. \quad (6.7)$$

Using the two equations from above one can calculate the length of the normal component of the transmitted wave vector \mathbf{k}_2 :

$$k_2^2 = k_{2n}^2 + (\mathbf{k}_1 - \mathbf{k}_{1n})^2 \quad (6.8)$$

$$k_{2n}^2 = k_2^2 - (\mathbf{k}_1 - (\mathbf{k}_1 \hat{n}) \hat{n})^2 \quad (6.9)$$

$$= k_2^2 - (k_1^2 - 2(\mathbf{k}_1 \hat{n})^2 + (\mathbf{k}_1 \hat{n})^2) \quad (6.10)$$

$$= k_2^2 - k_1^2 + (\mathbf{k}_1 \hat{n})^2. \quad (6.11)$$

Finally one can express the full transmitted wave vector \mathbf{k}_2 using only known quantities:

$$\mathbf{k}_2 = \mathbf{k}_{1t} - \sqrt{k_2^2 - k_1^2 + (\mathbf{k}_1 \hat{n})^2} \hat{n} \quad (6.12)$$

$$= \mathbf{k}_1 - (\mathbf{k}_1 \hat{n}) \hat{n} - \sqrt{k_2^2 - k_1^2 + (\mathbf{k}_1 \hat{n})^2} \hat{n}. \quad (6.13)$$

I divide by k_2 with $\mathbf{k}_2/k_2 = \hat{t}$ and $\mathbf{k}_1/k_2 = \eta \hat{i}$ in order to introduce unit direction vectors \hat{i} and \hat{t} for incident and outgoing light. The relative index change across the interface is $\eta = n_1/n_2$.

6. Raytracing for spatio-angular microscopy

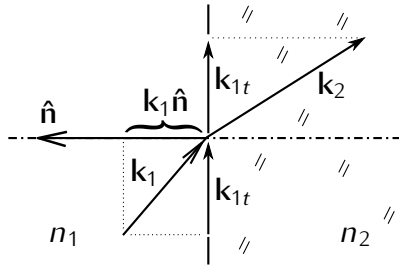


Figure 6.1.: Refraction at an interface transforms the incident wave vector \mathbf{k}_1 into the outgoing wave vector \mathbf{k}_2 .

$$\hat{\mathbf{t}} = \eta \hat{\mathbf{i}} - \eta (\hat{\mathbf{i}} \hat{\mathbf{n}}) \hat{\mathbf{n}} - \sqrt{1 - \eta^2 + \eta^2 (\hat{\mathbf{i}} \hat{\mathbf{n}})^2} \hat{\mathbf{n}} \quad (6.14)$$

$$= \boxed{\eta \hat{\mathbf{i}} - \left(\eta \hat{\mathbf{i}} \hat{\mathbf{n}} + \sqrt{1 - \eta^2 (1 - (\hat{\mathbf{i}} \hat{\mathbf{n}})^2)} \right) \hat{\mathbf{n}}} \quad (6.15)$$

When the radical in the square root is negative a reflection occurs instead (TIRF). Then the tangential component is invariant and normal component inverts the sign:

$$\mathbf{k}_2 = \mathbf{k}_{1t} - \mathbf{k}_{1n} \quad (6.16)$$

$$= \mathbf{k}_1 - 2\mathbf{k}_{1n} \quad (6.17)$$

$$= \mathbf{k}_1 - 2(\mathbf{k}_1 \hat{\mathbf{n}}) \hat{\mathbf{n}} \quad (6.18)$$

$$\hat{\mathbf{t}}_{\text{TIR}} = \boxed{\hat{\mathbf{i}} - 2(\hat{\mathbf{i}} \hat{\mathbf{n}}) \hat{\mathbf{n}}} \quad (6.19)$$

6.2. Intersection of a ray and a plane

Let a ray start at a point \mathbf{s} with direction $\hat{\mathbf{d}}$. A plane (defined by a point \mathbf{c} and the normal $\hat{\mathbf{n}}$) intersects this ray if normal and ray direction are not perpendicular: $\hat{\mathbf{n}} \hat{\mathbf{d}} \neq 0$. The distance between the plane and the origin is $h = \mathbf{c} \hat{\mathbf{n}}$. I define the plane equation in Hesse normal form:

$$\mathbf{r} \hat{\mathbf{n}} = h \quad (6.20)$$

6. Raytracing for spatio-angular microscopy

I replace the coordinate \mathbf{r} with the ray equation and solve for the parameter τ :

$$(\mathbf{s} + \tau\hat{\mathbf{d}})\hat{\mathbf{n}} = \mathbf{h} \quad (6.21)$$

$$\mathbf{s}\hat{\mathbf{n}} + \tau\hat{\mathbf{d}}\hat{\mathbf{n}} = \mathbf{h} \quad (6.22)$$

$$\tau = \boxed{\frac{\mathbf{h} - \mathbf{s}\hat{\mathbf{n}}}{\hat{\mathbf{d}}\hat{\mathbf{n}}}} \quad (6.23)$$

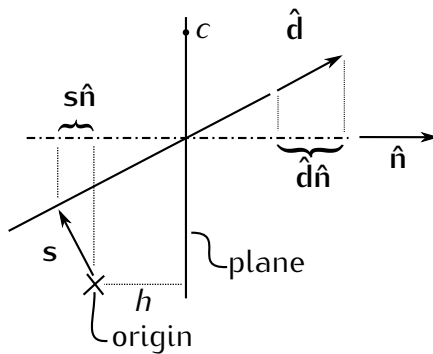


Figure 6.2.: Schematic of plane-ray intersection.

6.3. Intersection of a ray and a sphere

Let a ray start at a point \mathbf{s} with direction $\hat{\mathbf{d}}$. Let a sphere be centred in \mathbf{c} with radius R . Their two equations

$$(\mathbf{r} - \mathbf{c})^2 = R^2 \quad (6.24)$$

$$\mathbf{r} = \mathbf{s} + \tau\hat{\mathbf{d}} \quad (6.25)$$

define the intersection points. Substitution of \mathbf{r} results in a quadratic equation for τ :

$$(\mathbf{s} + \tau\hat{\mathbf{d}} - \mathbf{c})^2 = R^2 \quad (6.26)$$

$$\mathbf{l} := \boxed{\mathbf{s} - \mathbf{c}} \quad (6.27)$$

$$\mathbf{l}^2 + 2\tau\mathbf{l}\hat{\mathbf{d}} + \tau^2 - R^2 = 0 \quad (6.28)$$

$$\underbrace{1}_a \tau^2 + \underbrace{2\mathbf{l}\hat{\mathbf{d}}}_b \tau + \underbrace{\mathbf{l}^2 - R^2}_c = 0 \quad (6.29)$$

6. Raytracing for spatio-angular microscopy

6.3.1. Solving the quadratic equation

In order to prevent numerical errors the following solution should be used (Press et al. 1997):

$$\Delta := b^2 - 4ac \quad (6.30)$$

$$q := \frac{b + \sqrt{\Delta} \operatorname{sign} b}{2} \quad (6.31)$$

$$\tau = \begin{cases} q/a & \text{when } |q| \approx 0 \\ c/q & \text{when } |a| \approx 0 \\ (q/a, c/q) & \text{else} \end{cases} \quad (6.32)$$

If the discriminant Δ is negative the ray misses the sphere and there is no solution. If the discriminant is zero the ray touches the periphery and there is only one solution. A positive discriminant corresponds to two solutions.

6.4. Refraction on paraxial thin lens

The incident beam with direction \hat{i} hits the lens at the point ρ . A line parallel to \hat{i} through the centre of the lens defines the point on the focal plane, which will be intersected by the transmitted ray r as well.

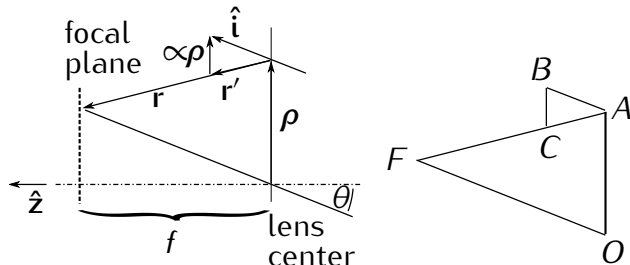


Figure 6.3.: Construction of a ray on a thin lens. The incident beam with direction \hat{i} (from right) hits the lens at the point ρ .

The triangle ABC is similar to triangle FOA . All three angles are identical because each of the lines are parallel: $\overline{CB} \parallel \overline{OA} \parallel \rho$, $\overline{FA} \parallel \overline{CA}$ and $\overline{AB} \parallel \overline{OF} \parallel \hat{i}$. The side \overline{OF} is hypotenuse of a right angled triangle. Its adjacent with respect to the angle θ has length f . Therefore one can deduce the length $|\overline{OF}| = f / \cos \theta$. Between the two similar triangles, the following relation holds and can be used

6. Raytracing for spatio-angular microscopy

to calculate the length $|\overline{BC}|$:

$$\frac{|\overline{BC}|}{|\overline{BA}|} = \frac{|\overline{OA}|}{|\overline{OF}|} \quad (6.33)$$

$$\frac{|\overline{CB}|}{1} = \frac{\rho}{f/\cos(\theta)}. \quad (6.34)$$

Given its length, the vector \overline{CB} can now be calculated, because its direction is known to be along ρ . With this vector and \hat{i} one can now obtain the (arbitrarily scaled) transmitted vector r' . I could normalize it but it turns out to be useful for the high NA immersion lens to find the vector r , that ends in the focal plane. The procedure from above is condensed in the following equations:

$$\rho = (x_0, y_0, 0)^T = \rho(\cos \phi, \sin \phi, 0)^T \quad (6.35)$$

$$\phi = \arctan(y_0/x_0) \quad (6.36)$$

$$\cos \theta = \boxed{\hat{i}\hat{z}} \quad (6.37)$$

$$r' = \hat{i} - \frac{\cos \theta}{f} \rho \quad (6.38)$$

$$r = \boxed{\frac{f}{\cos \theta} \hat{i} - \rho} \quad (6.39)$$

6.5. Refraction through high NA objective (illumination)

It is possible to augment the results of the calculation from the previous chapter to treat an aplanatic immersion objective (Hwang and Lee 2008).

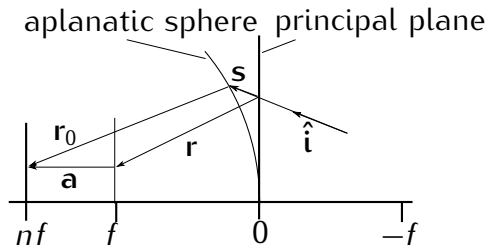


Figure 6.4.: Construction of a ray on an high numerical aperture oil immersion objective. As opposed to a thin air lens the objective's focal length needs to be corrected by the focus difference vector a to accommodate for the immersion and one must take into account spherical principal surface (aplanatic surface) .

I account for the immersion medium by shifting the focal plane in sample space

6. Raytracing for spatio-angular microscopy

to nf using the focus difference vector \mathbf{a} .

$$\mathbf{a} = \boxed{f(n - 1)\hat{\mathbf{z}}} \quad (6.40)$$

$$R = \boxed{nf} \quad (6.41)$$

The principal surface² is a sphere of radius $R = nf$ around the image point (Smith 2000, p. 22 and Botcherby et al. 2008). In the paper Hwang and Lee (2008) they express the deviation between the real principal surface and the principal plane with an approximation for small angles θ and ϕ :

$$\mathbf{s} = \left(R - \sqrt{R^2 - \rho^2} \right) \hat{\mathbf{i}} \quad (6.42)$$

This is an approximation because it only takes into account the perpendicular (along \mathbf{z}) distance between plane and sphere. They demonstrate the viability of this approximation by comparing its results with a full raytrace through a 100×1.41 objective. Focus displacement errors are less than 130 nm for a field of $86.4 \mu\text{m}$ radius. This would be sufficient for our problem. However, in my implementation I reuse the code for ray–sphere intersection to determine the exact vector \mathbf{s} .

The final ray exiting the objective has the direction \mathbf{r}_0 :

$$\mathbf{r}_0 = \boxed{\mathbf{r} + \mathbf{a} - \mathbf{s}}. \quad (6.43)$$

6.6. Reverse path through oil objective (detection)

Now I consider the oil objective in the reverse direction (see Figure 6.6). Given a ray that starts within the sample I will determine the ray in the pupil.

6.6.1. Easy case: back focal plane positions only

If the intersections of rays in the back focal plane are sufficient, a full raytrace is not necessary. This is the case when imaging beads in index matched embedding medium and we want to calculate a pattern for the pupil plane SLM (MMA). Instead it is sufficient to ignore ray origins and just consider their directions in the sample.

²Microscope objectives generally fulfil the Abbe sine condition and form stigmatic images from the sample plane in the image image plane. In this case the principal surface on the object side is a sphere.

6. Raytracing for spatio-angular microscopy

A unit ray direction $\hat{\mathbf{i}} = (x, y, z)^T$ in sample space is transformed into a position $\mathbf{r}_b = (x', y')^T$ in the back focal plane of the objective. The azimuthal angle ϕ isn't changed when going through the objective. The polar angle θ defines how far off axis the back focal plane is hit.

$$\phi' = \phi = \arctan(y/x) \quad (6.44)$$

$$\theta = \arcsin(\sqrt{x'^2 + y'^2}) \quad (6.45)$$

$$r_b = nf \sin \theta \quad (6.46)$$

$$\mathbf{r}_b = r_b (\cos \phi', \sin \phi')^T \quad (6.47)$$

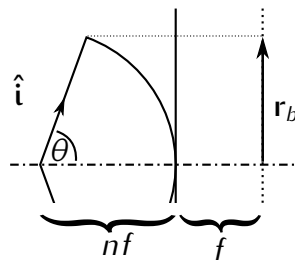


Figure 6.5.: Schematic for tracing a ray direction $\hat{\mathbf{i}}$ from sample space into the back focal plane. The bigger the angle between $\hat{\mathbf{i}}$ and the optical axis, the further outside the ray will pass through the back focal plane.

6.6.2. Full raytrace through oil objective in detection direction

Now I discuss the general case and calculate both, the origins and the directions of rays emerging from the back focal plane. This is necessary in order to trace light bundles from the specimen into the plane of the camera (or focal plane SLM). In the next section I will further modify these formulas to incorporate aberrations due to non-index matched embedding medium.

The position of the objective is defined by its principal point \mathbf{c} and the normal $\hat{\mathbf{n}}$ (directed along optical axis towards sample space). The incident ray is defined by its starting point \mathbf{p} and the direction $\hat{\mathbf{i}}$. First I calculate the centre of the aplanatic sphere \mathbf{g} :

$$\mathbf{g} = \mathbf{c} + nf\hat{\mathbf{n}}. \quad (6.48)$$

Then I obtain the position \mathbf{p}' by intersecting the incident ray and the plane perpendicular to the optical axis through \mathbf{g} . The focus difference vector is defined

6. Raytracing for spatio-angular microscopy

by its length and the optical axis. It can be used to calculate an intermediate point \mathbf{p}'' .

$$\mathbf{a} = -f(n-1)\hat{\mathbf{n}} \quad (6.49)$$

$$\mathbf{p}'' = \mathbf{p}' + \mathbf{a}. \quad (6.50)$$

The point \mathbf{p}'' has now been shifted, so that a thin air lens would image it exactly as the oil objective would image \mathbf{p}' . One can use \mathbf{p}'' to find the direction $\hat{\mathbf{t}}$ of the transmitted ray. It is just the normalized difference vector \mathbf{m} to the principal point.

$$\mathbf{m} = \mathbf{c} - \mathbf{p}'' \quad (6.51)$$

$$\hat{\mathbf{t}} = \mathbf{m}/|\mathbf{m}|. \quad (6.52)$$

As a last step I calculate the starting point \mathbf{e} of the transmitted ray by intersecting the incident ray with the aplanatic sphere.

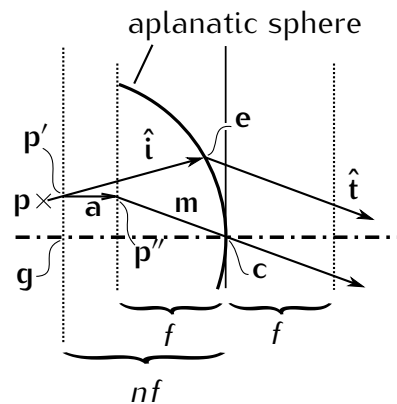


Figure 6.6.: Construction to find the transmitted ray through an oil immersion objective from a point within the sample.

6.6.3. Treatment of aberration (detection)

Now I will extend the formulas of the previous section to include aberrations due to a non-matched embedding medium $n_e \neq n$.

I consider a ray originating in point \mathbf{p} with direction $\hat{\mathbf{i}}$ within an immersion of index n_e . I determine the intersection \mathbf{f} of the ray with the coverslip–embedding interface and refract to obtain $\hat{\mathbf{i}}'$. Then I calculate the time t a photon takes, to

6. Raytracing for spatio-angular microscopy

travel from \mathbf{p} to the interface \mathbf{f} :

$$t = |\mathbf{f} - \mathbf{p}| \frac{n_e}{c} \quad (6.53)$$

and extend the path of the photon backward along the direction $\hat{\mathbf{i}}'$ (corrected for the refraction at the coverslip–embedding surface) by the distance tc/n . This results in the corrected position \mathbf{p}' that indicates where the photon would have originated if the embedding would have been index matched. Now I can apply the equations from the previous sections on the ray defined by \mathbf{p}' and $\hat{\mathbf{i}}'$ to obtain the transmitted ray in the pupil.

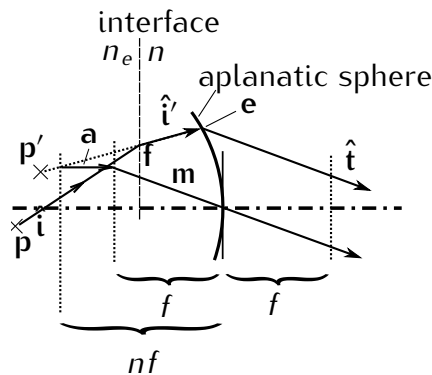


Figure 6.7.: Construction that treats the interface between embedding and immersion medium

6.7. Sphere projection

When I model our sample as a collection of spheres, it is useful to trace rays from the periphery of these spheres through an in focus target \mathbf{c} into the back focal plane.

While the previous sections have described a fairly general raytracer, this section is very technical and relates to our specific problem to represent the sphere model of a fluorophore distribution with as few rays as possible.

The tangents of an out-of-focus sphere S_r^s centred at \mathbf{s} with radius r that pass through the target \mathbf{c} form a double cone (assuming \mathbf{c} is outside of S_r^s). The tangents touch the surface of the sphere S_r^s at the circular intersection C with the sphere S_R^c centred at \mathbf{c} with radius $R = |\mathbf{c} - \mathbf{s}|$. Radius R is the distance from the target to the centre of the out-of-focus sphere. In order to find a point \mathbf{e} where a tangent touches the out-of-focus sphere, it is sufficient to solve the following equation in

6. Raytracing for spatio-angular microscopy

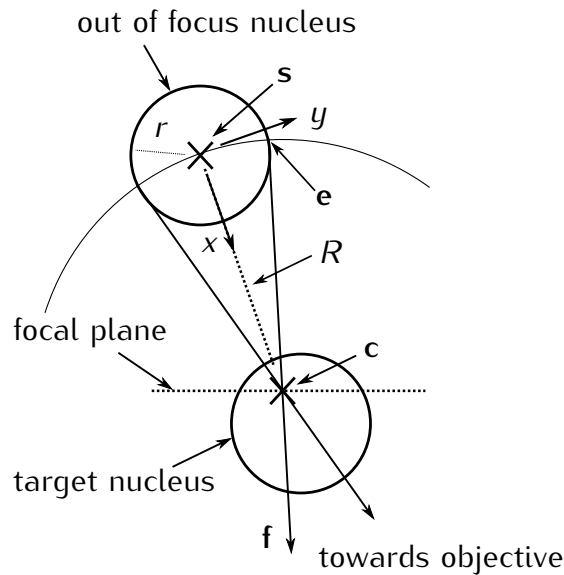


Figure 6.8.: Schematic of how an out-of-focus nucleus and a target point c (not necessarily in the centre of a target nucleus) define a cone of tangential rays.

a 2D coordinate system with the origin in the centre s of the out-of-focus sphere:

$$(x - R)^2 + y^2 = R^2 \quad (6.54)$$

$$x^2 + y^2 = r^2 \quad (6.55)$$

There are two solutions:

$$x_1 = \frac{r^2}{2R} \quad (6.56) \text{ ?eqn:x1?}$$

$$y_{1/2} = \pm \frac{r}{2R} \sqrt{4R^2 - r^2} \quad (6.57) \text{ ?eqn:y1?}$$

In the case $R < r$ the out-of-focus nucleus is intersecting the target, obviating the reason to do the projection in the first place.

I construct two vectors \hat{x} and \hat{y} that span the coordinate system, in order to transform the solution from 2D into 3D. The (unnormalized) direction x of the x-axis of this coordinate system is given by the difference vector of the target c and the nucleus centre s . The direction y must be perpendicular to x and is obtained by calculating the cross product with another vector q . I ensure that q and x are not colinear. The vectors q and x are colinear, when the absolute value

6. Raytracing for spatio-angular microscopy

of their scalar product equals the square of the length $|\mathbf{q}\mathbf{x}| = \mathbf{x}^2$.

$$\mathbf{x} = \mathbf{c} - \mathbf{s} \quad (6.58)$$

$$\mathbf{q} = \begin{cases} (0, 0, 1)^T & \text{when } |x_z| < \frac{2}{3}|\mathbf{x}| \\ (0, 1, 0)^T & \text{else} \end{cases} \quad (6.59)$$

$$\mathbf{y} = \mathbf{x} \times \mathbf{q} \quad (6.60)$$

$$\hat{\mathbf{x}} = \mathbf{x}/|\mathbf{x}| \quad (6.61)$$

$$\hat{\mathbf{y}} = \mathbf{y}/|\mathbf{y}| \quad (6.62)$$

Now I can sample the intersection circle C in order to create viable starting points \mathbf{e} for tangential rays. Let $R_{\phi}^{\hat{\mathbf{c}}}$ be a rotation matrix that rotates a vector by angle ϕ around an axis $\hat{\mathbf{c}}$. A point \mathbf{e} on the circle is then defined using one solution from equations 6.56 and 6.57. The ray direction \mathbf{f} is then easily obtained:

$$\mathbf{e} = \mathbf{s} + x_1 \hat{\mathbf{x}} + y_1 R_{\phi}^{\hat{\mathbf{x}}} \hat{\mathbf{y}} \quad (6.63)$$

$$\mathbf{f} = \mathbf{c} - \mathbf{e}. \quad (6.64)$$

Tracing a sufficient number of rays (e.g. 16) with direction \mathbf{f} for different angles ϕ to the back focal plane gives the projection of the intersection circle C . Note that this projection in general is not a circle anymore.

For practical reasons its useful to project vector \mathbf{x} as well. It can be used as the centre of the (distorted) shape on the back focal plane to rasterize it as a fan of triangles.

6.8. Conclusion

I documented how to trace rays through a perfect thin lens and a high numerical aperture objective. These equations are the starting point to find good illumination strategies.

The treatment of aberrations due to a non-matching embedding medium needs more parameters (target depth, refractive index n_e) and a raytrace from sample space, through the back focal plane, tubelens and focal plane SLM (fLCoS). However, it enriches the type of control, that can be implemented. Illumination with high angles into a low index embedding medium will create thin slices of light (highly inclined and laminated optical sheet, see section 3.1.2).

Note that ray optics are not an sufficient approximation, when intensity features

6. Raytracing for spatio-angular microscopy

in the scale of the wavelength are to be investigated. Small features would mean that only a few pixels of the LCoS would be enabled. This would mean that most of the information of the MMA pattern is filtered out at the LCoS and no simultaneous tight angular control would be possible.

7. Experimental results with spatio-angular microscope

Here I describe some of our experiments that demonstrate the functioning of our spatio-angular microscope prototype.

In the first experiment I use total internal reflection which prevents high angles from reaching the sample when the refractive index of the embedding medium is lower than that of the immersion. This allows to show in a simple way that the angular illumination control works.

In the second experiment, we measure the three-dimensional light distribution in the sample by bleaching a fluorescent gel layer.

Then I describe another experiment, that replicates the problem of imaging life specimen. The task is to localize three-dimensionally distributed beads and then image them individually using an optimized excitation light distribution.

7.1. Measuring acceptance angle for three different embedding media

As one of the first attempts to use the spatio-angular illumination system, I devised an experiment to determine the acceptance angle of a microscope objective as a function of the embedding medium.

For the measurement a thin layer of fluorophores was applied with a marker pen on three microscope slides. As a spacer, a surrounding circle was painted with nail polish. After drying, a drop of a liquid embedding medium was added to two of the samples (immersion oil ($n = 1.52$) and water ($n = 1.33$)). Then coverslips were added to all three samples and sealed with nail polish.

During the measurement the focal plane SLM projected a disk with $30\ \mu\text{m}$ diameter on the fluorescent plane. The illumination angle was varied by stepping a window of 15×15 pixels (equivalent to 1/17th of the pupil diameter) over the pupil plane SLM.

scan pupil plane SLM

7. Experimental results with spatio-angular microscope

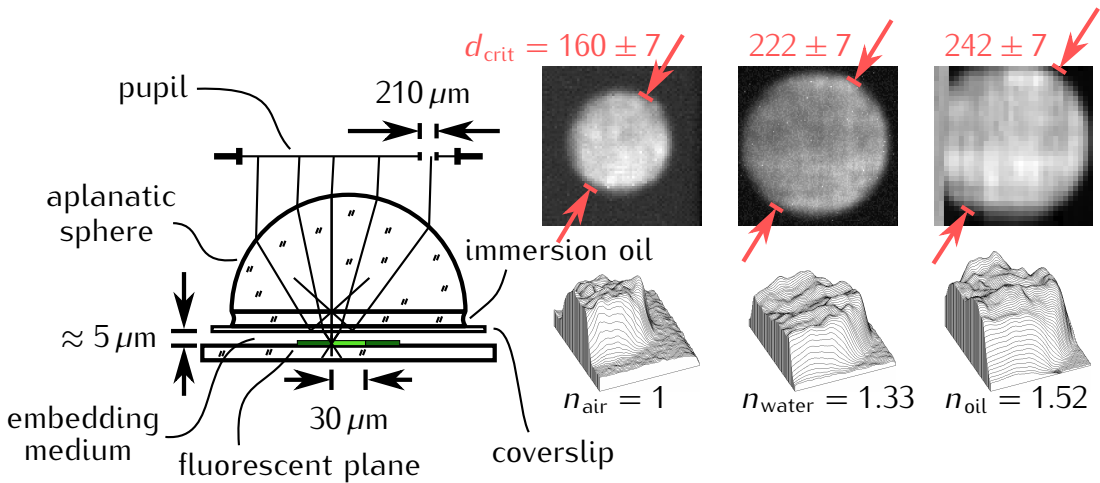


Figure 7.1.: A fluorescent plane on a slide is embedded in oil, water or air. The thickness of the embedding medium is approximately $5 \mu\text{m}$. The focal plane SLM illuminates a disk with $30 \mu\text{m}$ diameter while a window of 15×15 pixels is scanned over the MMA. The window corresponds to a square with $210 \mu\text{m}$ on the side as opposed to 3.6 mm pupil diameter. The red numbers indicate the diameter of the bright circle in pixels of the pupil plane SLM.

For each angle, the sum of all fluorescence light reaching the camera is recorded. The data is depicted in the three images in Figure 7.1. These images contain a bright disk whose diameter d_{crit} is growing with the index of the embedding medium. The center of the disk corresponds to the optical axis of the objective. Points in the interior of the circle have an almost constant intensity (residual fluctuations can be attributed to non-uniformity of the illumination of the pupil plane SLM). For oil immersion the measured diameter of the disk corresponds to the diameter of the pupil. I compare the measurement with the pupil diameter for the objective with magnification $63\times$ and numerical aperture 1.47 that was used in the experiment.

$$d_{\text{pupil}}^{(\text{measure})} = d_{\text{crit}}^{(\text{oil})} \Lambda = (242 \pm 7) \cdot 16 \mu\text{m} = (3.88 \pm 0.08) \text{ mm} \quad (7.1)$$

$$d_{\text{pupil}}^{(\text{theory})} = \text{NA} \cdot f_{\text{TL}}/63 = 1.47 \cdot \underbrace{164.5 \text{ mm}/63}_{f_{\text{obj}}} = 3.84 \text{ mm} \quad (7.2)$$

Here Λ is the pixel pitch of the pupil plane SLM and f_{TL} is the standard tube length for Zeiss microscopes and is used to calculate the focal length f_{obj} of the objective.

If the index of the embedding medium is less than the index of the immersion medium, then total internal reflection occurs on the interface between coverslip

7. Experimental results with spatio-angular microscope

and embedding medium for high incidence angles. The excitation light can then no longer reach the sample. Therefore, the disks in the plots for water and air are smaller.

The relationship between the diameter d_{crit} of the bright circle and the critical angle of total reflection at the interface between coverslip ($n_{\text{cs}} = n_{\text{oil}} = 1.52$) and embedding medium (n_{emb}) is as follows:

$$\theta_{\text{crit}} = \arcsin \left(\frac{n_{\text{emb}}}{n_{\text{oil}}} \right) \quad (7.3)$$

$$d_{\text{crit}} = 2n_{\text{oil}} f_{\text{obj}} \sin \theta_{\text{crit}} = 2n_{\text{oil}} f_{\text{obj}} \frac{n_{\text{emb}}}{n_{\text{oil}}} \quad (7.4)$$

A comparison between the ratios of the measured diameters and the ratios of the refractive indeces in Table ?? shows that the measurement is in good agreement with the theory.

	$n_{\text{emb}}/n_{\text{oil}}$	$d_{\text{crit}}^{\text{emb}}/d_{\text{crit}}^{\text{oil}}$
water	0.875	0.88 ± 0.05
air	0.658	0.64 ± 0.04

Table 7.1.: Comparison showing that the measurement of the angle of acceptance for two different embedding media corresponds to the theory.

7.2. Measuring light distribution by bleaching a fluorescent gel

The above-described experiment allows only an indirect measurement of the effects of angular control in our microscope. Now I describe an experiment where fluorophores in a slab of several microns thickness are bleached. This allows a more direct measurement of the light distribution in the sample by imaging the bleached region in a confocal microscope.

As a sample we use a 4% agarose gel containing fluorescently labeled DNS plasmids. The exact sequence of the plasmids is irrelevant. They only serve as carriers for the fluorophore (SYBR Save DNA gel stain, Invitrogen). Exposed samples are stable for several weeks and no unbleached fluorophores diffuse to bleached regions. The gel was chosen and prepared by Florian Rückerl with whom I conducted this experiment. We reported on this in Rückerl et al. (2013).

During the experiment the focal plane SLM displays three different patterns (all dark, all bright, bright vertical bar) and the pupil plane SLM displays eight different patterns (all dark, all bright, and 6 circular windows). The focal plane

7. Experimental results with spatio-angular microscope

SLM was projected as far into the gel layer as the working distance of the objective would allow and an exposure series was produced overnight. Utilizing a XY-stage, the sample was moved by 0.4 mm between exposures.

overall light efficiency

The laser delivers a continuous beam of 473 nm wavelength with 400 mW power. It is modulated using an acousto-optic modulator (AOM) so that only during the camera integration time (20 ms), and when the two SLM are in a defined state, light can excite the sample. The modulated beam (duty cycle < 50%) has an average power of 15 mW. For this experiment I illuminate the rotating micro-lens array and integrator rod directly (without fibre bundle). I made this decision in the hope to reduce the necessary bleaching time. In hindsight it would have been better to use the fibre bundle. Behind the integrator tunnel there were still 7 mW average power and in front of the dichroic mirror of the microscope a mere 17 μ W (with both SLM showing a white pattern, giving an illuminated field diameter of 40 μ m in the sample).

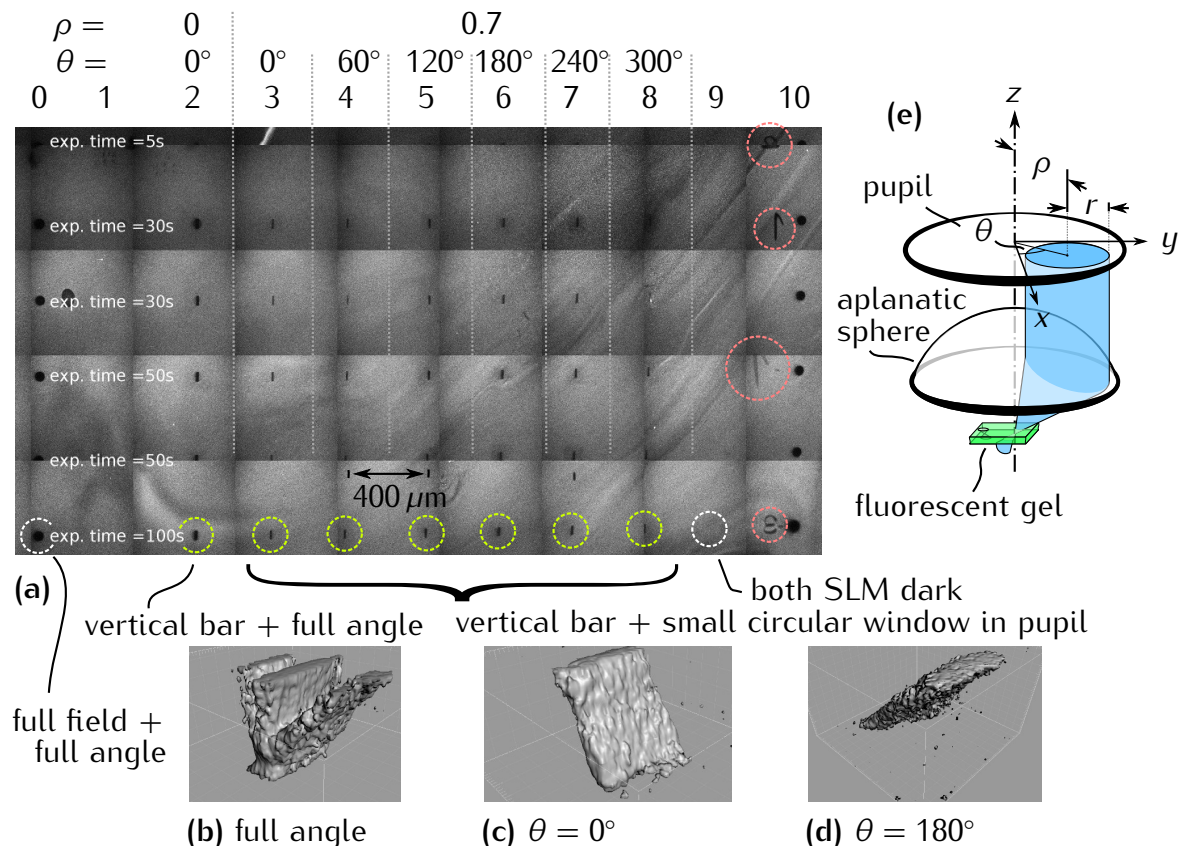


Figure 7.2.: The confocal measurements and images were kindly provided by Florian Rückerl (Institut Pasteur).

Figure 7.2 a) is a mosaic of confocal images in the vicinity of the plane in the bleached gel where the focal plane SLM was focused. The bleached areas

7. Experimental results with spatio-angular microscope

form a pattern of 11×6 exposures. The bleaching dose varies with the vertical direction as indicated by the accumulated exposure times (consisting of numerous individual 20 ms camera integrations). Strong in-focus bleaching becomes evident for bleach durations from 30 s and higher, corresponding to a light dose above 40 J/cm^2 in the focal plane.

Along the horizontal direction, different SLM patterns were displayed. The two areas at both outer borders (column 0 and 10) were bleached with full angular and spatial exposure. The next columns 1 and 9 give an indication of how well both SLM can produce black as no bleaching pattern is evident in these places.

The central areas (columns 2–9, indicated with green circles) were all displaying a vertical bar on the focal plane SLM while the pupil plane SLM displayed a circular window, varying the incidence angle. The first bar from the left (column 2) was illuminated with all angles. Figure 7.2 b) shows a three-dimensional representation of a confocal recording of the bleached area. Unfortunately, three separate bundles are visible, indicating insufficient uniformity of the illumination. As the non-uniformities are not rotationally symmetric with respect to the optical axis, the bundles propagate at slightly different angles.

The images in Figure 7.2 c) and d) show confocal measurements of illumination with restricted angles (columns 3 and 6). For this, a circular window with radius $r = 0.3$ was displayed on the pupil plane SLM. Where the coordinates ρ and r are given relative to the pupil radius — for $\rho = 1$ the window would be centered on the periphery of the pupil, as indicated in the drawing of Figure 7.2 e).

Dark digits in the mosaic (framed by red circles) are landmarks that were retrospectively bleached into the specimen for orientation during the acquisition with the confocal microscope.

7.3. Spatio-angular illumination of three-dimensionally distributed beads

The next experiment models the imaging conditions of a biological sample. For this, beads of three microns diameter were distributed in agarose gel. The goal is to first localize the beads and subsequently utilize the knowledge of their three-dimensional distribution to find patterns for the pupil plane SLM to excite and image the beads individually while avoiding exposure of out-of-focus beads.

First of all I show a focal series of wide field images with z -steps of one micron and illumination of the full field using all angles in the left mosaic of

observed bleaching patterns

wide field baseline

7. Experimental results with spatio-angular microscope

Figure 7.3. These recordings show how several beads sequentially come into focus. In order to facilitate the discussion I manually labeled each bead with its number. Unfortunately, the gel contributes a relatively high background fluorescence from which the blurred images of beads are no longer distinguishable after only three microns of defocus. For this sample of sparse beads, their three-dimensional distribution could easily be determined from these wide field images. In a more dense sample, e.g. a higher bead concentration or nuclei in an embryo, this is no longer possible.

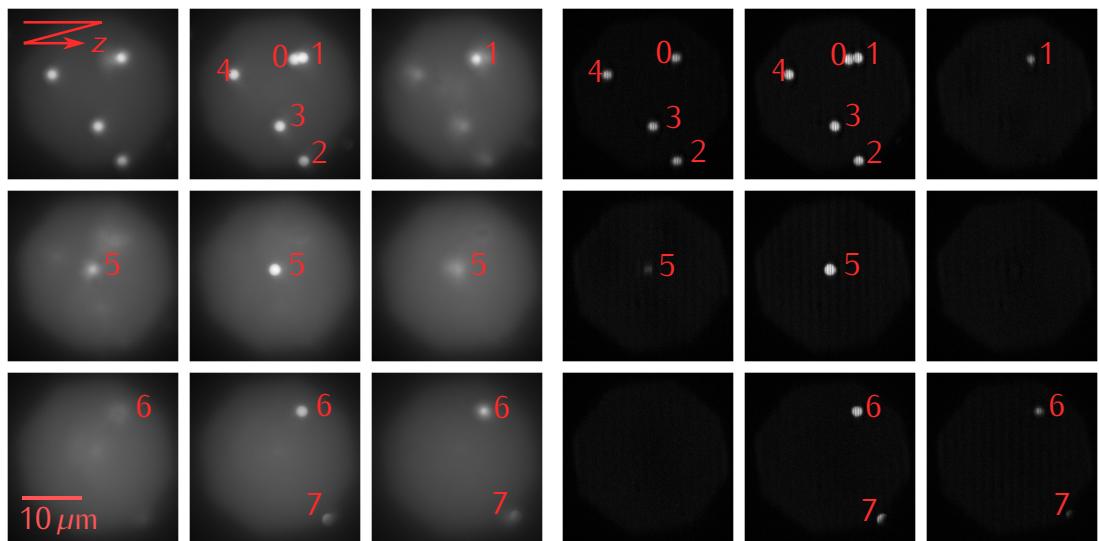


Figure 7.3.: **left:** Wide field focus series of a three-dimensional distribution of yellow-green beads in agarose gel. Sampling in z is $1 \mu\text{m}$. **left:** Computationally sectioned images of the same sample. The corresponding raw images are shown in Figure B.1 on page 109.

optical sectioning

In those cases it is useful to utilize structured illumination to separate out-of-focus and in-focus fluorescence. The mosaic on the right of Figure 7.3 shows the computed optical sections from four raw images per slice. The raw images are displayed in Figure B.1 in the appendix on page 109. The sections contain relatively distinct vertical reconstruction artifacts. These can be avoided using the HiLo reconstruction method which has the additional advantage of only needing two raw images per slice.

bead localization

However, the HiLo method needs considerably more code and I have not implemented it in my real-time imaging software. Also, the artifacts have no effect on the localization precision of the algorithm. For localization I determine the center of each bead by finding local maxima after applying a three-dimensional difference of Gaussian filter (matched to the bead diameter). The resulting

7. Experimental results with spatio-angular microscope

coordinates are depicted in the inlay in Figure 7.4.

In the next step, each bead is illuminated individually by displaying a bright disk at the corresponding position on the focal plane SLM while the pupil plane SLM respectively displays a mask which prevents exposure of out-of-focus beads. This mask is calculated automatically with a raytracer and utilizing the three-dimensional model of the bead distribution.

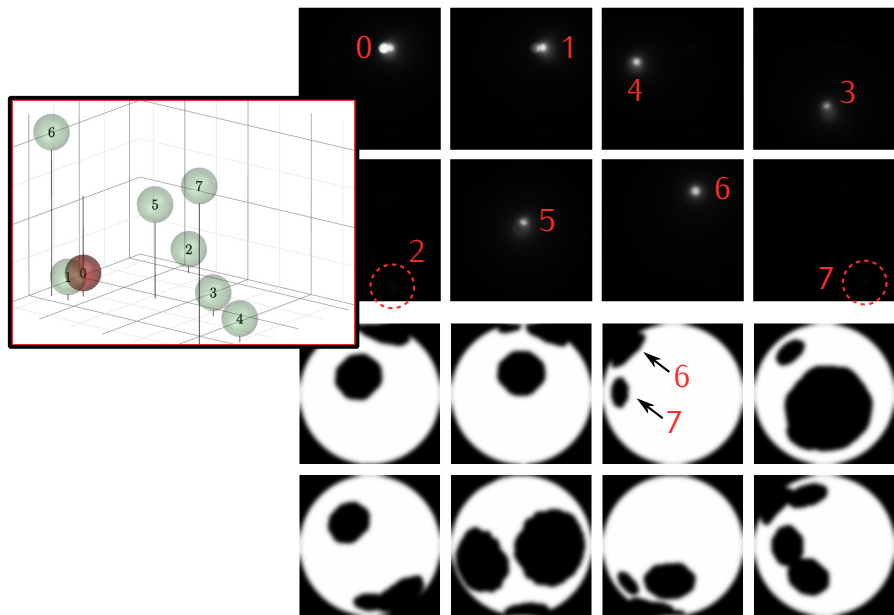


Figure 7.4.: left inlay: Coordinates of the beads from Figure 7.3. **top mosaic:** Camera images with spatio-angular illumination of the beads. This is not a focus series but an image of each individual bead. **bottom mosaic:** Corresponding patterns of the pupil plane SLM.

The eight camera images of the individual beads are shown in the two top rows in Figure 7.4. Unlike Figure 7.3, no focal series is shown. Each image is focused on a single bead. The corresponding pupil plane SLM masks are shown in the two rows below. I will briefly describe the construction of the masks using bead 4 as an example. According to the three-dimensional diagram in the inlay in Figure 7.4 bead 4 is on the edge of the bead distribution. The smallest angle relative to the optical axis is between the connecting line of bead 4 and 7. Therefore the single "shadow" (indicated with an arrow) in the pupil plane mask corresponds to bead 7. All other beads would only be illuminated by light that strikes bead 4 under a larger angle. Bead 6 and maybe bead 5 combine to the second shadow on the periphery of the pupil.

The camera images of bead 2 and 7 in Figure 7.4 stand out because they are completely dark. The reason is that the registration between the focal plane SLM

description of pupil
plane masks

stability

7. Experimental results with spatio-angular microscope

and camera has shifted by a few microns between localizing the beads and their spatio-angular exposure. This type of error was corrected by removing rubber feet from the microscope and screwing it directly to the metal table.

artifacts

A more interesting effect is visible in the camera image of bead 5. Only the bottom half of the bead is illuminated but due to fluorescence in the agarose gel the circular area that is illuminated by the focal plane SLM is still visible. This effect would predominantly occur in samples where fluorescent areas are not sharply defined. As exposures with light from different angles will contain different contributions of background fluorescence it is not clear whether individual sub-images of the spatio-angular microscope can be joined into a seamless image. The image quality of confocal microscopes hardly seems achievable. Cells in an embryo can probably be counted and tracked, but a quantitative measurement of the fluorescence seems difficult.

comparison spatial control and only angular control

I imaged the beads in Figure 7.4 with both full angles and optimized angles. Already the selective illumination of individual beads using only the focal plane SLM and full angles reduced the background fluorescence from other beads and the gel significantly. Unfortunately, it is not possible to discern any further improvement with additional angular control. I think the fluorescence from out-of-focus beads can not be detected in the photon shot noise of the fluorescence from the gel. Angular control will still have a positive effect because out-of-focus beads are not uselessly exposed — it is just not possible to measure this in this particular sample.

7.4. Angular illumination and a higher concentration of beads

In order to measure the influence of angular illumination control directly, I made another sample with higher concentration of beads in an agarose gel with significantly less fluorescence.

The images are shown in Figure 7.5. In the wide field image I indicate one bead with a white circle. In the other images this bead is selectively illuminated using the focal plane SLM white circle with dashed outline.

For simplicity, I have omitted the raytrace illumination optimization and just vary a circular window on the pupil plane SLM ($\rho = 0.7, r = 0.3$, with the same geometry as in Figure 7.2 e)).

In the mosaic on the right side of Figure 7.5 the intensity is displayed with a factor of 100× compared to the previous two images. The same scaling is applied to the images of the mosaic. The intensity of the central bead is clipped. The

7. Experimental results with spatio-angular microscope

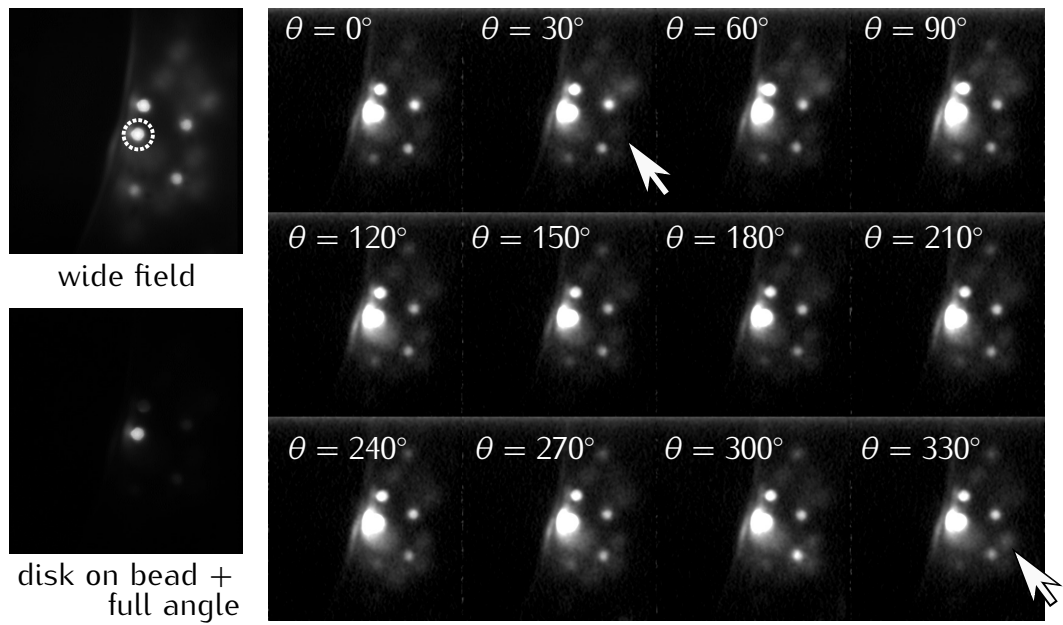


Figure 7.5.: Dense beads in agarose gel **top left:** Wide field image of the beads. The target bead is highlighted with a white circle. **bottom left:** Target bead is selectively illuminated by the focal plane SLM (using all angles). **right mosaic:** Variation of illumination angle. The contrast of out-of-focus beads is increased by scaling the values with a factor of 100 compared to the two images on the left.

illumination cone, that moves with the window manifests itself as a change in the relative intensities of the out-of-focus beads. A difference can be seen, for example, in the point marked by an arrow in the pictures for $\theta = 30^\circ$ and $\theta = 330^\circ$.

7.5. Conclusion

The described experiments demonstrate that the hardware of the microscope is functioning as intended. Although the performance is impaired by low transmission and long pattern loading times.

Especially for the experiment in section 7.3 a lot of software had to work in conjunction. The mapping between focal plane SLM and camera has to be established, the beads must be located and optimal illumination patterns must be found. These algorithms should work in close combination with the hardware control, so that the entire experiment can run with as little user interaction as possible and finish within reasonable time.

8. Discussion

This thesis deals with the practical development of a wide-field fluorescence microscope system that can control the irradiance in the specimen as well as the illumination angles with the aim of decreasing phototoxicity.

origin of the idea

The original idea was to combine a programmable array microscope with a control of the illumination directions. Initially this seems to be an elegant approach: The programmable array microscope produces two images on a camera, one of which contains only out-of-focus light. By variation of the illumination angle of the excitation light, it should be possible to find the direction with minimal out-of-focus contributions.

Fairly quickly it became clear that this approach, if at all, would work only inefficiently. After all, for the programmable array microscope to work, fine structures must be imaged into the specimen. This, however, has the consequence that several diffraction orders instead of one bundle of rays with similar directions must traverse the sample. For most specimens this will bring no advantage compared to a wide-field microscope.

We opted instead for a modification of the excitation path in a wide-field microscope. My assumption was that given an estimate of the 'to-be-imaged' three-dimensional fluorophore distribution, and perhaps additional information on the expected movement of cells, pathogens or organs; a sufficiently accurate prediction of the expected out-of-focus light can be made.

description of the hardware

Using two spatial light modulators (SLM), we can project appropriate distributions of excitation light into the sample. One SLM controls the angle and the other the in-focus pattern of light. Our goal for the instrument was that it can capture one stack per minute, consisting of twenty slices. For this, partial recordings of slices should be acquired in sequence and later composed into one image. Therefore We selected the SLM devices with an emphasis on high speed.

The fastest commercially available SLM are ferroelectric liquid crystal on silicon devices (fLCoS) and digital micro-mirror devices (DMD), which both can only do binary modulation. However, in our case binary intensity modulation is disadvantageous. Sharp edges lead to high diffraction losses and strong

8. Discussion

oscillations of the field in the Fraunhofer diffraction pattern.

The pupil plane SLM, that controls the illumination angles does not necessarily need a high resolution but a binary SLM device should be avoided here because otherwise oscillations of excitation intensity would occur in the specimen and appear on the camera image. For this reason, we use a specifically developed SLM, which resembles a DMD in terms of mode of operation and speed but can display gray scale values.

The focal plane SLM, on the other hand, should have a high resolution and it should be possible to update its patterns very fast, depending on recent camera acquisitions. Initially I opted for a SLM that is connected to the graphics card of a computer. We chose a fLCoS SLM because its pixel borders are less sharp than the DMD and we expected a better efficiency for our application. Unfortunately there were difficulties with the synchronization of the graphics card and the other devices. Therefore, relatively late into the project I had to replace the SLM controller with another one that contains internal memory and is linked to a computer via USB. Unfortunately, the USB connection is very slow and fast update of image patterns is no longer possible. In retrospect, it would have been easier to use two identical gray value SLM from Fraunhofer. Note that Institut Pasteur and Fraunhofer IPMS continue this work and do just that under the Joint-Programme Inter Carnot Fraunhofer PICF 2011, "Micromirror Enhanced Microscopic Imaging for high-speed angular and spatial light control in spectral Optogenetics and Photomanipulation applications in biological applications" (MEMI-OP).

A serious disadvantage of the Fraunhofer SLM in combination with the Fourier optical filter approach employed in our prototype is the small acceptance angle. This limits the exposed field to $80\text{ }\mu\text{m}$ diameter for a wavelength of 473 nm using a $63\times$ objective with a numerical aperture of 1.4, while the objective does support $400\text{ }\mu\text{m}$ field diameter. One solution could be contrast generation in a common path interferometer as described in the patent application (Heintzmann and Wicker 2010). The approach is derived from reflective Nomarski differential interference contrast microscopy. A birefringent prism separates the illumination bundle into bundles that have a small offset (shear). If the shear distance corresponds to the pixel pitch $\Lambda = 16\text{ }\mu\text{m}$ of the micro-mirrors then this device converts height differences between adjacent mirrors into intensity contrast. My experiments with a set of Nomarski prisms that were available in our lab gave an indication, that this method can work. However the prisms had too small a shear angle and returning diffraction orders were cut off. At this point in time, the planning for the original prototype was already so far advanced that a change was not possible.

Why Fraunhofer
micro-mirror array?

choice for focal
plane SLM

remedy against low
acceptance angle

8. Discussion

However, this is still a very promising method and will probably produce good results when prisms with larger shear angles are used. Additionally it should be noted that this method will work better for piston-type micro-mirrors than for torsion micro-mirrors.

priority of the control algorithm

Given the *low transmission* of our prototype, which could be just barely enough to investigate the biological test system of *C. elegans* embryos, the disproportionately high effort that went into synchronizing the two fast SLM which can only run at a *reduced duty cycle*, and the *limited etendue* which excludes some interesting experiments, it would have been better in hindsight, to build a demonstrator with two slow, conventional, gray-value SLM and to spend more effort on the development of the illumination control algorithm.

holographic system

In this context, with the aim of simplifying the hardware, I built a holographic illumination system consisting of a single phase-only SLM in the intermediate image plane. This enables simultaneous control of both, the in-focus light distribution as well as the illumination angles in the specimen. The SLM displays diffraction gratings and its arrangement is such, that the first diffraction order illuminates the pupil. The illumination angle in the specimen can be adjusted by the grating period and direction while the local irradiance is controlled with the grating contrast.

Unfortunately the phase-only SLM that I used for the experiments suffers from cross-talk between pixels, a non-linear transfer function and temporal fluctuations of the displayed phase pattern. It was uncertain whether these problems could be circumvented. Especially higher orders which are generated by the device's non-linearity and that can reach the sample are a problem, and it seems particularly difficult to project a finely structured grid into the sample. Projecting such patterns is necessary, because for my illumination algorithm I need a reasonably good measurement of the three-dimensional fluorophore distribution. For many specimen structured illumination is necessary to remove out-of-focus light from the raw images and obtain optical sections. Phase SLM which became available more recently have a much better performance and could probably be used to construct a holographic spatio-angular illumination device.

sectioning by structured illumination

Our prototype with two SLM is more suitable for structured illumination. The period on the focal plane SLM and the illumination aperture defined by the pupil plane SLM can be selected for best possible contrast of the in-focus light pattern. Optically sectioned images can be calculated with the usual methods. The HiLo method proposed by Jerome Mertz and best documented in Mertz and Kim (2010) is preferable to others as only two exposures per slice are necessary. Since

8. Discussion

images in our system are taken in rapid succession and movement artifacts are unlikely, we developed a variant of the HiLo method and in contrast to the original, which uses one uniformly illuminated image and one with structured illumination, we use two structured illumination images which gives better signal-to-noise.

sCMOS -- new camera technology

During my work on the project a much improved camera technology came to market. No such camera was used for measurements in this work, however, such a camera could be added to our system without substantial changes.

This change is made possible mostly due to the flexibility that the Arduino gives. This cheap and easy to use electronics platform has been used for several years in our lab and is particularly useful for synchronization of multiple devices. The source code for the Arduino microcontroller is often short and relatively easy to read. This controller is thus well suited to document the logic in our synchronization circuits and can be easily understood and extended by new members of our group.

During this work, I used many different electronic devices (SLM: Hamamatsu, Holoeye, ForthDD, Texas Instruments, Fraunhofer, cameras: Andor (Clara, IXon2, IXon3, IXon Ultra, Neo sCMOS), Photometrics Cascade II, Hamamatsu (Orca Flash 2.8 and 4.0), Logitech Pro 9000, and more). I noticed that construction and debugging effort depend very much on the quality of the documentation. If documentation is insufficient, which unfortunately is often the case, then it helps if communication is done with open standards (USB video device class, Ethernet).

Particularly positive I was surprised by the Texas Instruments DMD. The SLM development kit is very mature (?), contains open source software and high quality documentation explaining even the control registers of individual chips. While working with the kit I was able to implement features within three days, for which I spent several months of reverse engineering and trial and error on devices of other manufacturers — most notably, the fastest possible image update with 1440 frames per second via HDMI. If I had known that before, I would have designed the prototype differently and I would have accepted some drawback regarding optical performance.

I am particular unhappy with the state of scientific cameras as all of them gave me problems with incompatible or unstable drivers. Therefore, I hope that there will be more projects that open their resources to the public, such as Marc Levoy's Franken Camera (Adams et al. 2010); or that the manufacturers of the ever-improving consumer cameras document and disclose the protocols for disabling automatic image processing and accessing raw sensor data for their devices (as with the Logitech Pro 9000).

Arduino for control electronics

Open hardware is a good thing

8. Discussion

results of existing control software

Our prototype and the software for illumination optimization has been designed for the observation of cells in a developing *C. elegans* embryo. So far I was able to demonstrate spatio-angular illumination on static, non-living samples. So far I have not applied the method for living organisms. Here, the main problem is that image upload, especially to the focal plane SLM takes disproportionately long.

8.1. Outlook

proposal of an optogenetics experiment

If the sample does not change very fast, and plenty of time is available to upload images into the SLM controllers, then the current prototype allows experiments with rapidly changing illumination patterns (about 1000 fps should be possible). One interesting biological experiment would be similar to Branco et al. (2010). There, synapses were excited by moving a focal spot along one linear dendrite and its response was recorded as a function of the speed of the focal spot. With our system, two branches of a dendrite could be stimulated simultaneously and the response of the junction could be investigated.

next steps for control software

The algorithm for the optimization of the illumination patterns can still be improved. So far, I assume that the sample can be represented well by spheres. The nuclei in each slice are illuminated individually and the algorithm finds illumination angles so that exposure of out-of-focus nuclei is avoided. An obvious improvement would be to find nuclei that can be illuminated with similar angles and group them for simultaneous exposure. Even better would be an algorithm that does not need to represent the specimen as solid bodies but works directly on stacks of optical sections. In a first simple experiment, using the graphics processing unit, I could show that the extensive calculations can be carried out in reasonable time frames.

partial coherent simulation

Our work also leaves an unanswered question regarding the optics. It would be interesting to simulate the wave-optical image formation of the prototype with partial coherence. This would answer the question how important the gray levels of the micro-mirror array in the pupil-plane really are, and whether or not we can replace it with a binary DMD.

A similar simulation should be used to investigate the influence of field mask B0 and Fourier stop B1 on the contrast and the transfer function of the schlierenoptics system.

A. EM-CCD camera calibration

A.1. Andor Basic code listing for automatic image acquisition

```
' This is code for the Basic interpreter in Andor Solis
function ~GetSaturatingExposure()
    SetKineticNumber(1)
    exp=.01
    SetExposureTime(exp)
    run()
    m=maximum(#0,1,512)
    GetSaturatingExposure=exp*10000/(m-100)
    CloseWindow(#0)
return
name$ = "C:\Users\work\Desktop\martin\20111111\scan-em3\xion_"
print("start")

SetOutputAmp(1)
print("conv_start")
exp= ~GetSaturatingExposure()
print(exp)
SetExposureTime(exp)
SetKineticNumber(20)
SetShutter(0,1)
run()
save(#0,name$ + "conv1_dark.sif")
ExportTiff(#0, name$ + "conv1_dark.tif", 1, 1, 0, 0)
CloseWindow(#0)
CloseWindow(#1)

SetShutter(1,1)
run()
save(#0,name$ + "conv1_bright.sif")
ExportTiff(#0, name$ + "conv1_bright.tif", 1, 1, 0, 0)
CloseWindow(#0)
CloseWindow(#1)

SetOutputAmp(0)
SetShutter(1,1)
for i = 40 to 300 step 10
    SetGain(i)
    exp=~GetSaturatingExposure()
    print(exp)
    SetExposureTime(exp)
    SetKineticNumber(20)
    SetShutter(0,1)
    run()
```

A. EM-CCD camera calibration

```
    save(#0, name$ + str$(i) + "_dark.sif")
    ExportTiff(#0, name$ + str$(i) + "_dark.tif", 1, 1, 0, 0)
    CloseWindow(#0)
    CloseWindow(#1)
    SetShutter(1,1)
    run()
    save(#0, name$ + str$(i) + "_bright.sif")
    ExportTiff(#0, name$ + str$(i) + "_bright.tif", 1, 1, 0, 0)
    CloseWindow(#0)
    CloseWindow(#1)
next

SetOutputAmp(1)
print("conv_end")
exp= ~GetSaturatingExposure()
print(exp)
SetExposureTime(exp)
SetKineticNumber(20)
SetShutter(0,1)
run()
save(#0, name$ + "conv2_dark.sif")
ExportTiff(#0, name$ + "conv2_dark.tif", 1, 1, 0, 0)
CloseWindow(#0)
CloseWindow(#1)

SetShutter(1,1)
run()
save(#0, name$ + "conv2_bright.sif")
ExportTiff(#0, name$ + "conv2_bright.tif", 1, 1, 0, 0)
CloseWindow(#0)
CloseWindow(#1)
```

A. EM-CCD camera calibration

$g_{\text{ain}}_{\text{software}}$	$1/(M \cdot M_{\text{pre}})$ [e/ADU]	N_r [e/px]	$N_{(M)}/(W \times H)$ [e/px]	exposure [ADU]	$N'_{(M)}/(W \times H)$ [s]	$1/F_n$ [e/(px s)]
conv1	1.3165	7.189	3008.66	0.2016	14923	0.981
50	0.1160	0.486	260.05	0.0289	8995	0.591
60	0.0984	0.406	225.46	0.0249	9054	0.595
70	0.0841	0.349	190.52	0.0212	8983	0.591
80	0.0729	0.305	165.24	0.0186	8907	0.586
90	0.0680	0.288	150.54	0.0161	9368	0.616
100	0.0611	0.262	128.47	0.0136	9427	0.620
110	0.0550	0.241	121.11	0.0129	9409	0.619
120	0.0510	0.228	113.71	0.0120	9498	0.624
130	0.0465	0.211	106.66	0.0112	9541	0.627
140	0.0433	0.201	96.95	0.0101	9564	0.629
150	0.0405	0.192	89.68	0.0093	9671	0.636
160	0.0380	0.183	87.24	0.0090	9656	0.635
170	0.0359	0.175	81.56	0.0084	9739	0.640
180	0.0339	0.169	79.80	0.0081	9863	0.648
190	0.0321	0.163	74.00	0.0075	9806	0.645
200	0.0305	0.158	72.57	0.0073	9878	0.649
210	0.0292	0.155	69.44	0.0070	9944	0.654
220	0.0280	0.150	67.69	0.0068	9971	0.656
230	0.0268	0.147	65.63	0.0065	10057	0.661
240	0.0257	0.188	63.90	0.0063	10131	0.666
250	0.0244	0.140	62.52	0.0062	10026	0.659
260	0.0237	0.137	62.86	0.0062	10078	0.663
270	0.0229	0.135	63.17	0.0062	10130	0.666
280	0.0221	0.133	63.64	0.0062	10204	0.671
290	0.0214	0.130	63.38	0.0062	10162	0.668
300	0.0205	0.128	63.20	0.0062	10133	0.666
conv2	1.5953	8.768	8198.86	0.5291	15496	1.019

Table A.1.: Comparison of read noise for different EM-gain settings (first column) of the Andor Ixon3. W and H are the size of the sensor (in pixels). The value $N'_{(M)}$ estimates the number of photoelectrons the detector would have seen with 1 s integration time and is used to calculate the excess noise factor in the last column. In EM-mode the fastest readout speed was used 10 MHz with vertical shift speed of 1.7 μ s.

A. EM-CCD camera calibration

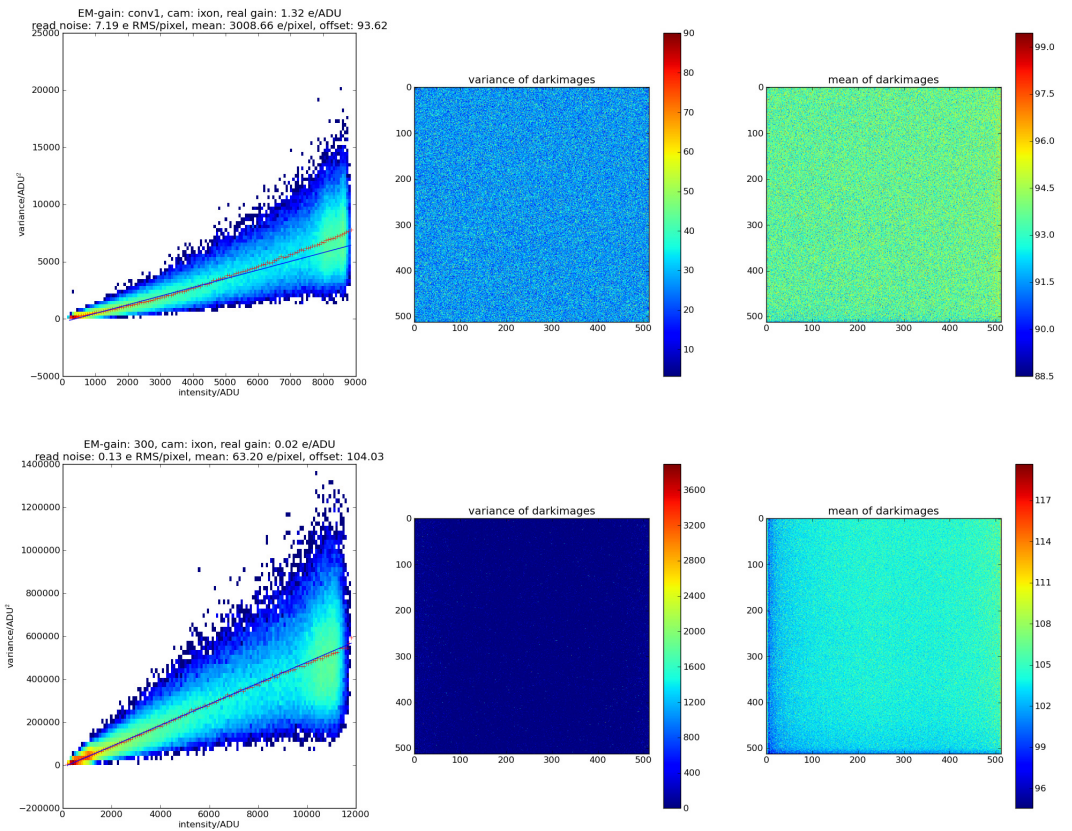


Figure A.1.: Readnoise evaluation using the Python code in section A.2
top: Conventional readout of an Andor Ixon3 camera.
bottom: readout with an EM-gain setting of 300 on the same camera with identical sample.
left: 2D histogram of per pixel variances against binned intensities.
middle: variance of 20 dark images. **right:** mean of 20 dark images.

A.2. Python code listing for the read noise evaluation

```

#!/usr/bin/env python
# ./ti.py /media/backup/andor-ultra-ixon/martin/20111111/scan-em3/ ultra 2700
import sys
import os

import matplotlib
matplotlib.use('Agg')

from pylab import *
from libtiff import TIFFfile, TIFFimage
from scipy import stats

seterr(divide='ignore')

folder = sys.argv[1]
cam = sys.argv[2]
gain = sys.argv[3]

```

A. EM-CCD camera calibration

```

def readpics(gain, cam='ixon_', isdark=False):
    print 'loading ', os.path.join(folder, cam) + '_' + gain + '_bright.tif'
    fg=TIFFfile(os.path.join(folder, cam) + '_' + gain + '_bright.tif')
    bright,bright_names=fg.get_samples()
    bg=TIFFfile(os.path.join(folder, cam) + '_' + gain + '_dark.tif')
    dark,dark_names=bg.get_samples()
    return (bright[0],dark[0])

(f,b) = readpics(gain=gain, cam=cam)

bg=mean(b, axis=0)
v=var(f, axis=0)
i=mean(f, axis=0)

ny,nx=64,128
H,y,x=histogram2d(v.flatten(),i.flatten(),bins=[ny,nx],
                    range=[[0,v.max()], [0,i.max()]])
extent = [x[0], x[-1], y[0], y[-1]]
acc=zeros(x.shape, dtype=float64)
accn=zeros(x.shape, dtype=int64)
s=nx/i.max()
for ii, vv in nditer([i,v]):
    p=round(ii*s)
    acc[p]+=vv
    accn[p]+=1

fig=figure(figsize=(24, 8), dpi=300)
hold(False)
title('bal')
subplot(1,3,1)
imshow(log(H), extent=extent,
       aspect='auto', interpolation='none', origin='lower')
hold(True)
ax=x[nonzero(accn)]
ay=acc/accn
ay=ay[nonzero(accn)]
l=round(.6*len(ax))
bx=ax[0:l]
by=ay[0:l]
plot(ax,ay,'r+')
slope,intercept,rval,pval,stderr=stats.linregress(bx,by)
plot(ax,polyval([slope,intercept],ax))
xlabel('intensity/ADU')
ylabel(r'variance/ADU$^2$')
real_gain=1/slope # unit electrons/ADU
read_noise=sqrt(var(b))*real_gain # electrons RMS per pixel
mean_elecs=(mean(f)-mean(b))*real_gain # photoelectrons electrons per pixel
print gain, cam, real_gain, read_noise, mean_elecs, mean(b), rval, pval, stderr
tit='EM-gain: %s, cam: %s, real gain: %.2f e/ADU\n'
read noise: %.2f e RMS/pixel, mean: %.2f e/pixel, offset: %.2f'
% (gain, cam, real_gain, read_noise, mean_elecs, mean(b))
title(tit)
subplot(1,3,2)
imshow(var(b, axis=0))
title('variance of darkimages')
colorbar()
subplot(1,3,3)

```

A. EM-CCD camera calibration

```
imshow(mean(b, axis=0))
title('mean of darkimages')
colorbar()
show()
fig.savefig(cam+'_'+gain+'.png')
```

B. Optical sectioning by structured illumination

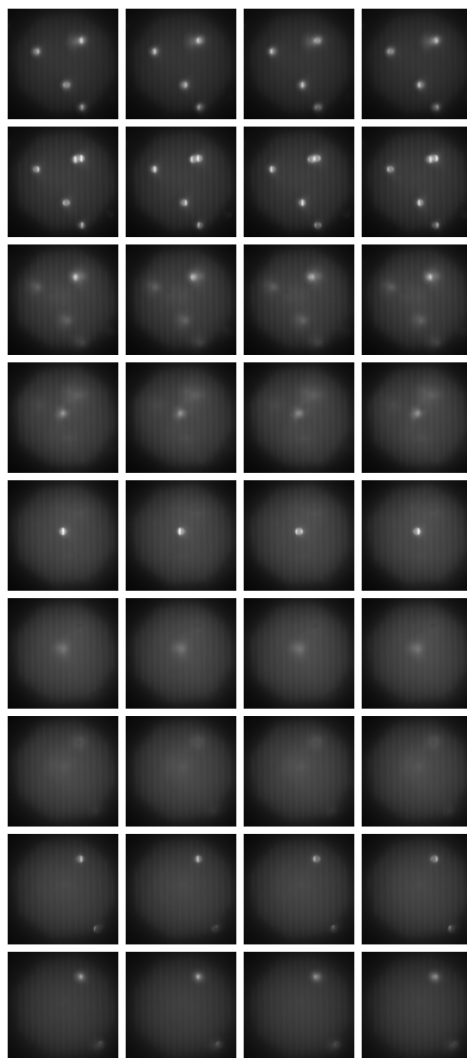


Figure B.1.: Structured illumination images of the same of the beads from Figure 7.3. Of each z -slice (rows) four exposures with different grating phase (columns) were captured.

C. Mapping between focal plane SLM and camera

C.1. Rigid coordinate transformation

Each term of the sum in equation ?? on page 73 can be expressed as two scalar terms:

$$\mathcal{Q} = \sum_i^n |s(\cos \phi r_{ix}^c + q \sin \phi r_{iy}^c) + t_x - r_{ix}^d|^2 + |s(-\sin \phi r_{ix}^c + q \cos \phi r_{iy}^c) + t_y - r_{iy}^d|^2 \quad (\text{C.1})$$

The following Maxima code will find the solution to the least squares problem:

```
load(minpack)$
q:-1;
g(s,p,tx,ty):=[s*( cos(p)*<cx>+q*sin(p)*<cy>)+tx-<dx>,
                 s*(-sin(p)*<cx>+q*cos(p)*<cy>)+ty-<dy>, ... ]$ 
minpack_lsquares(g(s,p,tx,ty), [s,p,tx,ty], [0.88,-3.1,1200,-20]);
```

I define the function `g` to contain all the terms of the sum. This can easily written by a program that constructs the lines according to the given pattern, replacing `<cx>`, `<cy>` with camera coordinates and `<dx>`, `<dy>` with display coordinates. The function `minpack_lsquares` calls the subroutine `lmder` which was originally developed for the Fortran¹ package `minpack`.

```
c  subroutine lmder (http://www.netlib.org/minpack/lmder.f)
c  the purpose of lmder is to minimize the sum of the squares of
c  m nonlinear functions in n variables by a modification of
c  the levenberg-marquardt algorithm. the user must provide a
c  subroutine which calculates the functions and the jacobian.
c  the subroutine statement is
c      subroutine lmder(fcn,m,n,x,fvec,fjac,ldfjac,ftol,xtol,gtol,
c                      maxfev,diag,mode,factor,nprint,info,nfev,
c                      njev,ipvt,qltf,wa1,wa2,wa3,wa4)
```

¹Rather than calling a Fortran library Maxima calls a version of this function that was automatically translated into Common Lisp via f2cl.

C. Mapping between focal plane SLM and camera

The reason for using Maxima is, that it calculates the symbolic Jacobian for the problem. This makes it straight forward to change the simple rigid transform to a model with more parameters.

The following Common Lisp code shows how the result of the optimization can be used to initialize the OpenGL modelview matrix to transform objects in its buffer, so that they will appear at the given positions on the camera.

```
(defun load-cam-to-lcos-matrix (&optional (x 0s0) (y 0s0))
  (let* ((s 0.828333873909549) (sx s) (sy (- s))
         (phi -3.102) (sp (sin phi)) (cp (cos phi))
         (tx 608.433) (ty 168.918)
         (a (make-array (list 4 4) :element-type 'single-float
                        :initial-contents
                        (list (list (* sx cp) (* sy sp) .0 (+ x tx))
                              (list (* -1 sx sp) (* sy cp) .0 (+ y ty))
                              (list .0 .0 1.0 .0)
                              (list .0 .0 .0 1.0))))))
  (gl:load-transpose-matrix (sb-ext:array-storage-vector a))))
```

Alternatively, here is the equivalent code in C (with different parameters):

```
float m[4*4]; // OpenGL Modelview Matrix
float s=-.8749328910202312,
      sx=s, sy=-s, phi=-.8052030670943575,
      cp=cos(phi), sp=sin(phi),
      tx=1456.71806436377,
      ty=910.4787738693659;
m[0]= sx*cp;   m[4]=sy*sp;   m[8] =0;   m[12]=tx;
m[1]=-1*sx*sp; m[5]=sy*cp;   m[9] =0;   m[13]=ty;
m[2]=0;        m[6]=0.;     m[10]=1;    m[14]=0;
m[3]=0;        m[7]=0.;     m[11]=0;   m[15]=1;
glMatrixMode(GL_MODELVIEW);
glLoadMatrixf(m);
```

C.2. Image processing: Localizing bright spots on the camera

The following Matlab listing shows how to open the image files:

```
%% load the files
% 0 .. 99 spot images
% only 10..99 usable because the first are on border and not illuminated
a = newim(1392,1040,103); for i=0:102
% Andor's FITS format isn't read correctly
% correct this by adding 2^15
a(:,:,i) = 2^15 + readim(sprintf('0%03d.fits',i));
end
```

Of the 103 images, that are loaded into `a`, the first 100 contain spots and the image at the zero-based index 102 is the uniformly illuminated image shown in Figure 5.8 left. The other two images at indices 100 and 101 are two centered disks with different diameters and are not used here.

C. Mapping between focal plane SLM and camera

```

bright = squeeze(a(:,:,102)); % histogram of uniformly illuminated
% image has minimum at 800 ADU
mask = gaussf(bright,8) > 800; % create mask with illuminated area
bg = 510; % the background is be 510 ADU

posmax = newim(100,2); for i = 10:99
% correct for sample non-uniformity
corr = (squeeze(a(:,:,i)) - bg) / bright * mask;
% find coordinates of maximum
[coords,vals]=findmaxima(gaussf(corr,32)); [valss,valsind] =
sort(vals); % sort coordinates by intensity
tmp = coords(valsind,:); % collect the maximum with highest
posmax(i,:) = tmp(end,:); % intensity into result
end

```

The DIPimage toolbox provides the function `findmaxima`, that locates all local maxima in an image with subpixel accuracy. I sort the result by gray value and only use the biggest. The measured 100 camera coordinate pairs in `posmax` correspond to r_i^c in equation 5.12.

From Matlab I create the file `fit.max` with batch commands for Maxima. Then I run Maxima. When it is finished after a few seconds, the file `max.out` will contain the four fitted parameters.

```

c = double(posmax)'; cmd =
''; % collect equations in maxima format
for i=10:99 dx = num2str(400+50*mod(i,10)); dy =
num2str(500+50*floor(i./10)); cx = num2str(c(i+1,1)); cy =
num2str(c(i+1,2)); cmd=[cmd ' s*( cos(p)*' cx '+q*sin(p)*' cy
') +tx-' dx ', ... s*(-sin(p)*' cx '+q*cos(p)*' cy ') +ty-' dy ','];
end cmd(:,end) = []; % delete last comma

% load the fitting package and start defining the merit function g
pre = 'load(minpack)$ q:-1; g(s,p,tx,ty):=[';
% now put cmd between
% call the fitting function and store the parameters into max.out
cod = [']$'
fit:minpack_lsquares(g(s,p,x,y),[s,p,x,y],[.88,-1.3,1200,-20]);'
... 'write_data(fit[1],"max.out");'

fid = fopen('fit.max','w'); % write maxima commands into file
fwrite(fid,[pre cmd cod]); fclose(fid);
[max_status,max_result]=system('maxima -b
fit.max'); % execute maxima

```

We load the transformation parameters back into Matlab and create the diagram Figure 5.9 to visualize, how well the transform matches camera and display coordinates.

```

% load rigid transformation parameters from the file into matlab
params = load('max.out'); scale = params(1); phi = params(2); tx =
params(3); ty = params(4);

mirr = -1; R = [cos(phi),mirr*sin(phi); -sin(phi),mirr*cos(phi)]; T

```

C. Mapping between focal plane SLM and camera

```
= [tx ty]';

%% plot the two grids on top of each other
mapped = zeros(100,2); for
i=11:100 % camera coordinates into display coordinates
mapped(i,:) = (scale*R*q(i,:)'+T)'; end

dpos = zeros(100,2); for i=0:99 % calculate display points
dpos(i+1,1) = 400+50*mod(i,10); dpos(i+1,2) = 500+50*floor(i./10);
end

hold off; plot(dpos(:,1),dpos(:,2),'.'); hold on;
plot(mapped(11:end,1),mapped(11:end,2),'r+');

%
```

Bibliography

- Abramoff** [1] M. D. Abràmoff, I. Hospitals, P. J. Magalhães, and M. Abràmoff. Image Processing with ImageJ. *Biophotonics International*, 2004. 5
- Adams2010** [2] A. Adams, M. Horowitz, S. H. Park, N. Gelfand, J. Baek, W. Matusik, M. Levoy, D. E. Jacobs, J. Dolson, M. Tico, K. Pulli, E.-V. Talvala, B. Ajdin, D. Vaquero, and H. P. a. Lensch. The Frankencamera. *ACM Transactions on Graphics*, 29(4):1, July 2010. ISSN 07300301. doi: 10.1145/1778765.1778766. URL <http://portal.acm.org/citation.cfm?doid=1778765.1778766>. 101
- Bernas2004** [3] T. Bernas, M. Zarebski, R. R. Cook, and J. W. Dobrucki. Minimizing photobleaching during confocal microscopy of fluorescent probes bound to chromatin: role of anoxia and photon flux. *Journal of microscopy*, 215(September):281–296, 2004. 18
- Berndt2007** [4] D. Berndt. *Software fuer die zeitoptimierte Kalibrierung von Mikrokippsspiegeln*. PhD thesis, Dresden, 2007. 65
- Berndt2010** [5] D. Berndt, J. Heber, S. Sining, D. Kunze, J. Knobbe, J.-U. Schmidt, M. Bring, D. Rudloff, M. Friedrichs, J. Roessler, M. Eckert, W. Kluge, H. Neumann, M. Wagner, and H. Lakner. Multispectral characterization of diffractive micromirror arrays. In *Proc. SPIE*, volume 7718, 2010. 65
- Berndt2011** [6] D. Berndt, J. Heber, S. Sining, and D. Rudloff. Calibration of diffractive micromirror arrays for microscopy applications. In *Proc. SPIE*, volume 81910O, 2011. doi: <http://dx.doi.org/10.1117/12.899881>. 65
- Botcherby2008** [7] E. J. Botcherby, R. Juškaitis, M. J. Booth, and T. Wilson. An optical technique for remote focusing in microscopy. *Opt. Commun.*, 281, 2008. 82
- Boyden2005** [8] E. S. Boyden, F. Zhang, E. Bamberger, G. Nagel, and K. Deisseroth. Millisecond-timescale, genetically targeted optical control of neural activity. *Nature neuroscience*, 8(9):1263–8, Sept. 2005. ISSN 1097-6256. doi: 10.1038/nn1525. URL <http://www.ncbi.nlm.nih.gov/pubmed/16116447>. 12

Bibliography

- Branco2010** [9] T. Branco, B. A. Clark, and M. Häusser. Dendritic discrimination of temporal input sequences in cortical neurons. *Science (New York, N.Y.)*, 329(5999):1671–5, Sept. 2010. ISSN 1095-9203. doi: 10.1126/science.1189664. URL <http://www.ncbi.nlm.nih.gov/pubmed/20705816>. 102
- Caarls2011** [10] W. Caarls, B. Rieger, A. H. B. De Vries, D. J. Arndt-Jovin, and T. M. Jovin. Minimizing light exposure with the programmable array microscope. *Journal of microscopy*, 241(1):101–110, Jan. 2011. ISSN 1365-2818. doi: 10.1111/j.1365-2818.2010.03413.x. URL <http://www.ncbi.nlm.nih.gov/pubmed/21118211>. 38, 45
- Chu2007** [11] K. K. Chu, D. Lim, and J. Mertz. Enhanced weak-signal sensitivity in two-photon microscopy by adaptive illumination. *Opt. Lett.*, 32(19):2846–2848, Oct. 2007. doi: 10.1364/OL.32.002846. URL <http://ol.osa.org/abstract.cfm?URI=ol-32-19-2846>. 43
- Denk1990** [12] W. Denk, J. H. Strickler, and W. W. Webb. Two-photon laser scanning fluorescence microscopy. *Science*, 245, 1990. 38
- Deschenes2002** [13] L. Deschenes and D. V. Bout. Single molecule photobleaching: increasing photon yield and survival time through suppression of two-step photolysis. *Chemical physics letters*, 365:387–395, 2002. URL <http://www.sciencedirect.com/science/article/pii/S0009261402014902>. 17
- Dixit2003** [14] R. Dixit and R. Cyr. Cell damage and reactive oxygen species production induced by fluorescence microscopy: effect on mitosis and guidelines for non-invasive fluorescence microscopy. *The Plant Journal*, 36(2):280–290, Oct. 2003. ISSN 09607412. doi: 10.1046/j.1365-313X.2003.01868.x. URL <http://doi.wiley.com/10.1046/j.1365-313X.2003.01868.x>. 16
- Dunsby2008** [15] C. Dunsby. Optically sectioned imaging by oblique plane microscopy. *Optics Express*, 16, 2008. 41
- Durbin1987** [16] R. M. Durbin. *Studies on the development and organisation of the nervous system of caenorhabditis elegans*. PhD thesis, Cambridge, 1987. 13
- Edelstein2010** [17] A. Edelstein, N. Amodaj, K. Hoover, R. Vale, and N. Stuurman. Computer Control of Microscopes Using μ Manager. In *Current Protocols in Molecular Biology*, number October, pages 14.20.1–14.20.17. John Wiley & Sons, Inc., 2010. ISBN 9780471142720. doi: 10.1002/0471142727.mb1420s92. 5
- Gamal2005** [18] A. E. Gamal and H. Eltoukhy. CMOS image sensors. *Circuits and Devices Magazine, IEEE*, (June), 2005. URL http://ieeexplore.ieee.org/xpls/abs_all.jsp?arnumber=1438751. 34

Bibliography

- [goodman1968][19] J. W. Goodman. *Introduction to Fourier optics*, volume 2. McGraw-Hill, New York, 1968. 24
- [Gross2005][20] H. Gross, W. Singer, M. Totzeck, F. Blechinger, and B. Achtner. *Handbook of optical systems*. Wiley-VCH, physical i edition, 2005. ISBN 9783527606689. URL <http://onlinelibrary.wiley.com/doi/10.1002/3527606688.fmatter/summary>. 20
- [grossman2010][21] N. Grossman, V. Poher, M. S. Grubb, G. T. Kennedy, K. Nikolic, B. McGovern, R. B. Palmini, Z. Gong, E. M. Drakakis, M. A. A. Neil, M. D. Dawson, J. Burrone, and P. Degenaar. Multi-site optical excitation using ChR2 and micro-LED array. *Journal of Neural Engineering*, 7(1):16004, 2010. URL <http://stacks.iop.org/1741-2552/7/i=1/a=016004>. 44
- [Gustafsson1995][22] M. G. L. Gustafsson, D. A. Agard, and J. W. Sedat. Sevenfold improvement of axial resolution in 3D wide-field microscopy using two objective lenses. *Proceedings of SPIE*, 2412:147–156, 1995. URL <http://scholar.google.com/scholar?hl=en&btnG=Search&q=intitle:Sevenfold+improvement+of+axial+resolution+in+3D+widefield+microscopy+using+two+objective+lenses#0>. 25, 26
- [Gustafsson1999][23] M. G. L. Gustafsson, D. A. Agard, and J. W. Sedat. I5M: 3D widefield light microscopy with better than 100 nm axial resolution. *Journal of Microscopy*, 195(July):10–16, 1999. 10, 26
- [Haferkorn1984][24] H. Haferkorn and W. Richter. *Synthese optischer Systeme*. Dt. Verl. der Wiss., Berlin, 1984. 20
- [Haken2006][25] H. Haken and H. C. Wolf. *Molekulphysik und Quantenchemie*. Springer, fifth edition, 2006. doi: 10.1007/3-540-30315-4. 17, 18
- [Cameras2012][26] Hamamatsu. Scientific images are more than just pictures. A camera should be more than just a sensor. Technical report, Hamamatsu, 2012a. 32, 34
- [Hamamatsu2012][27] Hamamatsu. Digital Camera C11440-22CU Instruction manual. Technical Report September, 2012b. 35
- [Heintzmann2010a][28] R. Heintzmann and K. Wicker. Optical devices and Methods, Patent application WO 2010/089548 A1, 2010. 99
- [Hoebe2007][29] R. A. Hoebe, C. H. Van Oven, T. W. J. Gadella Jr., P. B. Dhonukshe, C. J. F. Van Noorden, and E. M. M. Manders. Controlled light-exposure microscopy reduces photobleaching and phototoxicity in fluorescence live-cell imaging. *Nature*

Bibliography

Biotechnology, 25(2):249–253, Feb. 2007. ISSN 1087-0156. doi: 10.1038/nbt1278. 43

Hoebe2010[30] R. A. Hoebe, C. J. F. Van Noorden, and E. M. M. Manders. Noise effects and filtering in controlled light exposure microscopy. *Journal of Microscopy*, 240(3):197–206, 2010. ISSN 1365-2818. doi: 10.1111/j.1365-2818.2010.03400.x. URL <http://dx.doi.org/10.1111/j.1365-2818.2010.03400.x>. 43

Hope1999[31] I. Hope. *C. elegans: a practical approach*. Oxford University Press, Oxford, 1999. URL http://books.google.com/books?hl=en&lr=&id=B5JJaHa3JlgC&oi=fnd&pg=PR17&dq=C.+elegans:+A+Practical+Approach&ots=_FyXstupGY&sig=QlIY3tSNFRugKG002T91Fp6ZsOY. 57

Huisken2004[32] J. Huisken, J. Swoger, F. Del Bene, J. Wittbrodt, and E. H. K. Stelzer. Optical Sectioning Deep Inside Live Embryos by Selective Plane Illumination Microscopy. *Science*, 305(5686):1007–1009, Aug. 2004. ISSN 0036-8075. doi: 10.1126/science.1100035. URL <http://www.lmg.embl.de/pdf/huisken04.pdf>. 39, 40, 52

Hwang2008[33] S.-u. Hwang and Y.-g. Lee. Simulation of an oil immersion objective lens : A simplified ray-optics model considering Abbe's sine condition. *Optics Express*, 16(26):363–370, 2008. 76, 81, 82

Ipp2009[34] E. Ipp, J. Wenisch, and A. Jacobsen. Deliverable 8.04 Initial MMA/Optics evaluation system (refractive) v1.2. Technical report, In-Vision, 2009a. 63

Ipp2009a[35] E. Ipp, J. Wenisch, A. Jacobsen, and G. Zöchling. Deliverable 8.09 Final design of refractive optical systems. Technical report, In-Vision, 2009b. 65, 69

Konopka2008[36] C. A. Konopka and S. Y. Bednarek. Variable-angle epifluorescence microscopy: a new way to look at protein dynamics in the plant cell cortex. *The Plant Journal*, 53:186–196, 2008. URL <http://www.biochem.wisc.edu/faculty/bednarek/lab/publications/Konopka2007PlantJ.pdf>. 42

Koshel2012[37] R. Koshel. *Illumination Engineering: Design with Nonimaging Optics*. Wiley, 2012. ISBN 9781118462492. URL http://books.google.com/books?hl=en&lr=&id=WpL2SQoJCXYC&oi=fnd&pg=PR2&dq=Illumination+Engineering:+Design+with+Nonimaging+Optics&ots=7gJQ4QgdFp&sig=sTUpKAHR-GEA_d5BpVuGoZgNdAc. 64

Bibliography

- [Levoy2006][38] M. Levoy, R. Ng, A. Adams, M. Footer, and M. Horowitz. Light field microscopy. *ACM Trans. Graph.*, 25(3):924–934, July 2006. ISSN 0730-0301. doi: <http://doi.acm.org/10.1145/1141911.1141976>. URL <http://doi.acm.org/10.1145/1141911.1141976>. 46, 52
- [Levoy2009][39] M. Levoy, Z. Zhang, and I. McDowall. Recording and controlling the 4D light field in a microscope using microlens arrays. *Journal of Microscopy*, 235(2):144–162, 2009. ISSN 1365-2818. doi: 10.1111/j.1365-2818.2009.03195.x. URL <http://dx.doi.org/10.1111/j.1365-2818.2009.03195.x>. 46, 48
- [Lidke2005a][40] K. A. Lidke, B. Rieger, D. S. Lidke, and T. M. Jovin. The Role of Photon Statistics in Fluorescence Anisotropy Imaging. *IEEE Transactions on Image Processing*, 14(9):1237–1245, 2005. 31
- [Lippmann1908][41] G. Lippmann. Epreuves reversibles. Photographies intégrales. *Comptes-Rendus Académie des Sciences*, 146:446–451, 1908. URL <http://ci.nii.ac.jp/naid/10019520779/en/>. 45
- [Lutz2008][42] C. Lutz, T. S. Otis, V. DeSars, S. Charpak, D. A. DiGregorio, and V. Emiliani. Holographic photolysis of caged neurotransmitters. *Nat. Methods*, 5:821–827, Sept. 2008. URL <http://www.ncbi.nlm.nih.gov/pmc/articles/PMC2711023/>. 49
- [Mackay][43] C. D. Mackay, R. N. Tubbs, R. Bell, D. Burt, and I. Moody. Sub-Electron Read Noise at MHz Pixel Rates. *SPIE*, 2001. 32
- [Martínez-García2009][44] A. Martínez-García, I. Moreno, M. M. Sánchez-López, and P. García-Martínez. Operational modes of a ferroelectric LCoS modulator for displaying binary polarization, amplitude, and phase diffraction gratings. *Applied optics*, 48(15):2903–14, May 2009. ISSN 1539-4522. URL <http://www.ncbi.nlm.nih.gov/pubmed/19458742>. 69
- [Matthae2003][45] M. Matthae, L. Schreiber, and W. Faulstich, Andreas Kleinschmidt. High Aperture Objective Lens, Patent US 6,504,653 B2, 2003. 5
- [McClain1993][46] S. C. McClain, L. W. Hillman, and R. A. Chipman. Polarization ray tracing in anisotropic optically active media. I. Algorithms. *J. Opt. Soc. Am. A*, 10, 1993. 76
- [McCutchen1964][47] C. McCutchen. Generalized aperture and the three-dimensional diffraction image. *JOSA*, 54(2):240–244, 1964. ISSN 1084-7529. doi: 10.1364/JOSA.54.000240. URL <http://www.opticsinfobase.org/abstract.cfm?URI=JOSAA-19-8-1721><http://www.opticsinfobase.org/abstract.cfm?id=52274>. 23

Bibliography

- [Mehta2010a][48] S. B. Mehta. *Phase-space perspective of partially coherent imaging: Applications to biological phase microscopy*. PhD thesis, National University of Singapore, 2010. 67
- [Mertz2010][49] J. Mertz and J. Kim. Scanning light-sheet microscopy in the whole mouse brain with HiLo background rejection. *Journal of biomedical optics*, 15(1):016027, 2010. ISSN 1560-2281. doi: 10.1117/1.3324890. URL <http://www.ncbi.nlm.nih.gov/pmc/articles/PMC2917465/>&tool=pmcentrez&rendertype=abstract. 100
- [Murray2006][50] J. I. Murray, Z. Bao, T. J. Boyle, and R. H. Waterston. The lineageing of fluorescently-labeled *Caenorhabditis elegans* embryos with StarryNite and AceTree. *Nature protocols*, 1(3):1468–76, Jan. 2006. ISSN 1750-2799. doi: 10.1038/nprot.2006.222. URL <http://www.ncbi.nlm.nih.gov/pubmed/17406437>. 57, 59
- [Neil1997][51] M. A. A. Neil, R. Juškaitis, and T. Wilson. Method of obtaining optical sectioning by using structured light in a conventional microscope. *Optics Letters*, 22:1905–1907, 1997. 26
- [Nikolenko2008][52] V. Nikolenko, B. O. Watson, R. Araya, A. Woodruff, D. S. Peterka, and R. Yuste. SLM Microscopy: Scanless Two-Photon Imaging and Photostimulation with Spatial Light Modulators. *Front Neural Circuits*, 2:5, 2008. URL <http://www.ncbi.nlm.nih.gov/pmc/articles/PMC2614319/>. 49
- [Oron2005][53] D. Oron, E. Tal, and Y. Silberberg. Scanningless depth-resolved microscopy. *Opt Express*, 13:1468–1476, Mar. 2005. URL <http://www.weizmann.ac.il/home/feyaron/microscope/scanningless.pdf>. 48
- [Otsu2008][54] Y. Otsu, V. Bormuth, J. Wong, B. Mathieu, G. P. Dugue, A. Feltz, and S. Dieudonne. Optical monitoring of neuronal activity at high frame rate with a digital random-access multiphoton (RAMP) microscope. *J. Neurosci. Methods*, 173:259–270, Aug. 2008. URL http://cnp.igc.gulbenkian.pt/_media/research/mainen/ghyomm/otsu_2008.pdf. 43
- [Papagiakoumou2010][55] E. Papagiakoumou, F. Anselmi, A. Begue, V. de Sars, J. Gluckstad, E. Y. Isacoff, and V. Emiliani. Scanless two-photon excitation of channelrhodopsin-2. *Nat. Methods*, 7:848–854, Oct. 2010. 50, 51
- [Pawley2006][56] J. B. Pawley. More Than You Ever Really Wanted to Know About Charge-Coupled Devices. In J. B. Pawley, editor, *Handbook of biological confocal microscopy*, chapter Appendix 3, pages 918–931. Springer, third edition, 2006. 29, 31

Bibliography

- [Praitis2001][57] V. Praitis, E. Casey, D. Collar, and J. Austin. Creation of low-copy integrated transgenic lines in *Caenorhabditis elegans*. *Genetics*, 157(3):1217–26, Mar. 2001. ISSN 0016-6731. URL <http://www.ncbi.nlm.nih.gov/pmc/articles/PMC1461581/>. 13
- [Press1997][58] W. H. Press, S. A. Teukolsky, W. T. Vetterling, and B. P. Flannery. *Numerical Recipes in C*. Cambridge University Press, Cambridge, second edition, 1997. ISBN 0521431085. 80
- [Reddy2008][59] D. G. Reddy, K. Kelleher, R. Fink, and P. Saggau. Three-dimensional random access multiphoton microscopy for functional imaging of neuronal activity. *Nat. Neurosci.*, 11:713–720, June 2008. URL <http://www.ncbi.nlm.nih.gov/pmc/articles/PMC2747788/pdf/nihms129126.pdf>. 43, 44
- [Rhodes2008][60] C. Rhodes. SBCL: A Sanely-Bootstrappable Common Lisp. In R. Hirschfeld and K. Rose, editors, *Self-Sustaining Systems*, pages 74–86. Springer Berlin / Heidelberg, 2008. 5
- [Robbins2003][61] M. S. Robbins, S. Member, and B. J. Hadwen. The Noise Performance of Electron Multiplying Charge-Coupled Devices. *IEEE Transactions on Electron Devices*, 50(5):1227–1232, 2003. 32
- [Rodrigo2008][62] P. J. Rodrigo, D. Palima, and J. Glückstad. Accurate quantitative phase imaging using generalized phase contrast. *Optics Express*, 16:2740–2751, 2008. URL <http://www.opticsinfobase.org/abstract.cfm?URI=oe-16-4-2740>. 50
- [Ruckerl][63] F. Rückerl, M. Kielhorn, J.-y. Tinevez, J. Heber, R. Heintzmann, S. Shorte, I. Pasteur, I. Dynamique, A.-e. Str, R. Division, and M. Biophysics. Micro mirror arrays as high-resolution , spatial light modulators for photoactivation and optogenetics. In *SPIE*, volume 8586, 2013. 91
- [Santella2010][64] A. Santella, Z. Du, S. Nowotschin, A.-K. A. Hadjantonakis, and Z. Bao. A hybrid blob-slice model for accurate and efficient detection of fluorescence labeled nuclei in 3D. *BMC bioinformatics*, 11(1):580, 2010. ISSN 1471-2105. doi: 10.1186/1471-2105-11-580. URL <http://www.biomedcentral.com/1471-2105/11/580>. 4, 58
- [Santi2011][65] P. A. Santi. Light Sheet Fluorescence Microscopy. *Journal of Histochemistry and Cytochemistry*, 59:129–138, 2011. doi: doi:10.1369/0022155410394857. 39
- [Sauer2011][66] M. Sauer, J. Hofkens, and Joerg Enderlein. *Handbook of Fluorescence Spectroscopy and Imaging*. Wiley-VCH, Weinheim, 2011. ISBN 978-3-527-31669-4. 16, 18, 19

Bibliography

- [Schindelin2012][67] J. Schindelin, I. Arganda-carreras, E. Frise, V. Kaynig, M. Longair, T. Pietzsch, S. Preibisch, C. Rueden, S. Saalfeld, B. Schmid, J.-y. Tinevez, D. J. White, V. Hartenstein, K. Eliceiri, P. Tomancak, and A. Cardona. Fiji: an open-source platform for biological-image analysis. *Nature Methods*, 9(7), 2012. doi: 10.1038/nmeth.2019. 5
- [Schmidt2010][68] J. U. Schmidt, M. Bring, J. Heber, M. Friedrichs, D. Rudloff, J. Rossler, D. Berndt, H. Neumann, W. Kluge, M. Eckert, M. List, M. Mueller, and M. Wagner. Technology development of diffractive micromirror arrays for the deep ultraviolet to the near-infrared spectral range. In H. Thienpont, P. V. Daele, J. Mohr, and H. Zappe, editors, *MICRO-OPTICS 2010*, volume 7716 of *Proceedings of SPIE-The International Society for Optical Engineering*, 2010. ISBN 978-0-8194-8189-4. doi: 10.1117/12.855750. 65
- [Sheppard2006a][69] C. J. R. Sheppard, X. Gan, M. Gu, and M. Roy. Signal-to-Noise Ratio in Confocal Microscopy. In J. B. Pawley, editor, *Handbook of biological confocal microscopy*, chapter 22, pages 442–452. Springer, third edition, 2006. 32
- [Siedentopf1903][70] H. Siedentopf and R. Zsigmondy. Über Sichtbarmachung und Größenbestimmung ultramikroskopischer Teilchen, mit besonderer Anwendung auf Goldrubingläser. *Annalen der Physik*, 315:1–39, 1903. doi: DOI:10.1002/andp.19023150102. URL <http://onlinelibrary.wiley.com/doi/10.1002/andp.19023150102/abstract>. 39
- [Smith2000][71] W. J. Smith. *Modern optical engineering*. McGraw-Hill, 3 edition, 2000. ISBN 0-07-136360-2. 82
- [Stiernagle2006][72] T. Stiernagle. Maintenance of *C. elegans*. In C. e. R. Community, editor, *WormBook*, number 1999, pages 1–11. Jan. 2006. doi: 10.1895/wormbook.1.101.1. URL <http://www.ncbi.nlm.nih.gov/pubmed/18050451>. 13
- [Streibl1984][73] N. Streibl. Depth transfer by an imaging system. *Journal of Modern Optics*, 31(11): 1233–1241, 1984. URL <http://www.tandfonline.com/doi/abs/10.1080/713821435.26>
- [Sulston1977][74] J. E. Sulston and H. R. Horvitz. Post-embryonic cell lineages of the nematode, *Caenorhabditis elegans*. *Developmental biology*, 56(1):110–56, Mar. 1977. ISSN 0012-1606. URL <http://www.ncbi.nlm.nih.gov/pubmed/838129>. 13
- [Tinevez2012][75] J.-Y. Tinevez, J. Dragavon, L. Baba-Aissa, P. Roux, E. Perret, A. Canivet, V. Galy, and S. Shorte. *A quantitative method for measuring phototoxicity of a live cell imaging microscope.*, volume 506. Elsevier Inc., 1 edition, Jan. 2012. ISBN

Bibliography

9780123918567. doi: 10.1016/B978-0-12-391856-7.00039-1. URL <http://www.ncbi.nlm.nih.gov/pubmed/22341230>. 13, 15

- Tokunaga2008**[76] M. Tokunaga, N. Imamoto, and K. Sakata-Sogawa. Highly inclined thin illumination enables clear single-molecule imaging in cells. *Nature Methods*, 5(2):159–161, Feb. 2008. ISSN 1548-7091. doi: 10.1038/NMETH.1171. URL <http://www.ncbi.nlm.nih.gov/pubmed/18176568>http://www.riken.jp/ExtremePhotonics/realtime/s_no2.pdf. 42
- Linde2011a**[77] S. van de Linde. *Photoswitching of organic dyes and single molecule based super resolution imaging*. PhD thesis, Bielefeld, 2011. URL <http://pub.uni-bielefeld.de/publication/2436869>. 18
- Verveer1998**[78] P. J. Verveer, Q. S. Hanley, P. W. Verbeek, L. J. V. A. N. Vliet, and T. M. Jovin. Theory of confocal fluorescence imaging in the programmable array microscope (PAM). *Journal of Microscopy*, 189(March):192–198, 1998. 45
- Vogelsang2008**[79] J. Vogelsang, R. Kasper, C. Steinhauer, B. Person, M. Heilemann, M. Sauer, and P. Tinnefeld. A Reducing and Oxidizing System Minimizes Photobleaching and Blinking of Fluorescent Dyes. *Angew. Chem. Int. Ed.*, 47, 2008. doi: 10.1002/anie.200801518. 18
- Voie1993**[80] A. H. Voie, D. H. Burns, and F. A. Spelman. Orthogonal-plane fluorescence optical sectioning: three-dimensional imaging of macroscopic biological specimens. *Journal of Microscopy*, 1993. 39
- Vu2011**[81] P. Vu, B. Fowler, S. Mims, C. Liu, J. Balicki, and H. Do. Low Noise High Dynamic Range 2.3 Mpixel CMOS Image Sensor Capable of 100Hz Frame Rate at Full HD Resolution. *imagesensors.org*, pages 3–6, 2011. URL http://www.imagesensors.org/PastWorkshops/2011Workshop/2011Papers/P35_Fowler_HDR.pdf. 34
- Zahid2010**[82] M. Zahid, M. Vélez-Fort, E. Papagiakoumou, C. Ventalon, M. C. Angulo, and V. Emiliani. Holographic Photolysis for Multiple Cell Stimulation in Mouse Hippocampal Slices. *PLoS ONE*, 5(2):e9431, 2010. doi: 10.1371/journal.pone.0009431. URL <http://dx.doi.org/10.1371/journal.pone.0009431>. 49
- Zhang2009**[83] Z. Zhang and M. Levoy. Wigner distributions and how they relate to the light field. In *Computational Photography (ICCP), 2009 IEEE International Conference on*, pages 1–10, Apr. 2009. doi: 10.1109/ICCPHOT.2009.5559007. 46